On computations and their maintenance in the mouse visual system

Joel Bauer

December, 2022

On computations and their maintenance in the mouse visual system

Joel Bauer

Dissertation zum Erwerb des Doktortitels
an der Fakultät für Biologie der
Ludwig-Maximilians-Universität München

14 Dezember, 2022

Supervisors:
Prof. Dr. Mark Hübener
Prof. Dr. Tobias Rose
Prof. Dr. Tobias Bonhoeffer

First Reviewer:	Prof. Dr. Mark Hübener
Second Reviewer:	Prof. Dr. Laura Busse
Date of Submission:	14.12.22
Date of Defense:	22.03.23

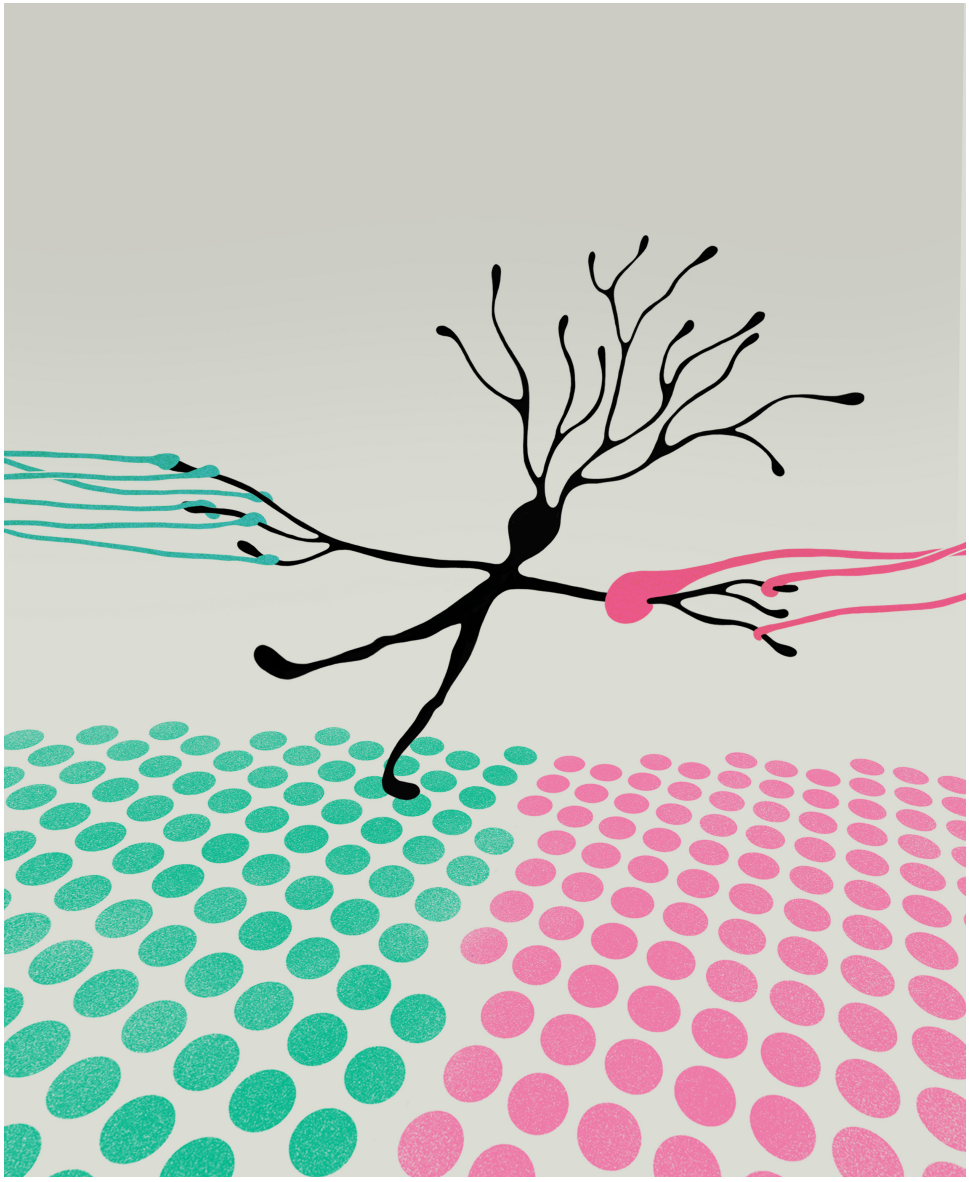

Illustration by Julia Kuhl

Contents

Abstract **vii**

1 Introduction **1**
1.1 Characteristics of the mouse visual pathway . . . 1
1.1.1 The retina and its projections . . . 1
1.1.2 Superior colliculus . . . 2
1.1.3 Dorsal lateral geniculate nucleus . . . 3
1.1.4 Primary visual cortex . . . 4
1.1.5 Higher visual areas . . . 5
1.2 Segregation of RGC afferent streams in the mouse dLGN . . . 6
1.2.1 Projection zones: Development of the spatial segregation of RGC projections 6
1.2.2 Cell types: Segregation through connection specificity . . . 7
1.2.3 Synaptic weights: Segregation through sparse connectivity and heterogeneous synaptic weights . . . 8
1.2.4 The specific case of eye-specific convergence . . . 9
1.2.5 Aims and objectives . . . 11
1.3 Representational stability and adaptability in the visual system . . . 12
1.3.1 Stability of structured projection patterns and macro-organization . . . 12
1.3.2 Single cell representational stability . . . 14
1.3.3 Experience-dependent plasticity in the visual system . . . 15
1.3.4 Aims and objective . . . 18

2 Materials and Methods **19**
2.1 Materials . . . 19
2.1.1 Viruses . . . 19
2.1.2 Antibodies . . . 19
2.1.3 Reagents . . . 20
2.1.4 Surgical reagents and drugs . . . 20
2.1.5 Surgical equipment: Intravitreal injections . . . 21
2.1.6 Eye dissection equipment . . . 21
2.1.7 Surgical equipment: Craniotomy, virus injections and cranial window implantation . . . 22
2.1.8 Two-photon imaging setup . . . 23
2.1.9 Analysis software . . . 23
2.1.10 Solutions . . . 24
2.2 Methods . . . 27
2.2.1 Eye-specific optogenetic input mapping in mouse dLGN . . . 27
2.2.2 Experience-dependent representational drift in mouse V1 . . . 33

3 Results **37**
3.1 Limited eye-specific convergence in the dLGN and its causes . . . 37
3.1.1 Experimental pipeline . . . 37
3.1.2 Limited overall eye-specific convergence on TC neurons in the dLGN . . . 38

3.1.3 Distribution of TC neuron eye preference and monocularity across dLGN and visuotopy . . . 40
3.1.4 The dendritic morphology of TC neurons cannot be classified into distinguishable types . . . 42
3.1.5 Segregation of eye-specific RGC axons cannot account for their low level of convergence on TC neurons . . . 43
3.1.6 TC neuron dendritic bias does not prevent eye-specific RGC input convergence 44
3.1.7 TC neuron eye preference is probabilistically determined by relative availability of RGC axons . . . 45
3.1.8 Non-dominant eye inputs have lower AMPAR to NMDAR mediated response ratios . . . 46
3.2 Experience dependent drift of orientation tuning in mouse V1 . . . 48
3.2.1 Pairwise signal correlation decay of tuning curves . . . 48
3.2.2 Drift of preferred orientation of V1 neurons . . . 49
3.2.3 Changing the statistics of the visual environment using cylinder lens goggles shifts the population distribution of preferred orientations . . . 51
3.2.4 Stripe rearing affects the direction of preferred orientation drift but not its magnitude . . . 53
3.2.5 Cell-specific restoration of preferred orientation after recovery from stripe rearing . . . 56

4 Discussion **59**
4.1 Synaptic input selection limits eye-specific convergence in the mouse dLGN . . . 59
4.1.1 Reconciling disparate levels of dLGN binocularity from different experimental approaches . . . 60
4.1.2 No TC neuron morphology types in dLGN . . . 62
4.1.3 To what degree does eye-specific RGC projection segregation contribute to eye-specific channel segregation? . . . 62
4.1.4 Eye-specific input selection and synaptic strengthening as mechanisms for channel segregation in dLGN . . . 63
4.1.5 Implications for other forms of visual stream segregation and integration . . 65
4.1.6 Summary and outlook . . . 66
4.2 Stability and drift of orientation tuning in mouse V1 . . . 67
4.2.1 PO drift as a novel aspect of representational drift in V1 . . . 67
4.2.2 Effects of behaviour and repeated stimulus exposure on V1 tuning . . . 68
4.2.3 What modulates drift speed? . . . 70
4.2.4 Perceptual learning and its effects on visual tuning properties . . . 72
4.2.5 Cell-specific restoration of PO coding . . . 73
4.2.6 Consequences of drift in V1 . . . 74
4.2.7 Summary and outlook . . . 76

Bibliography **79**

Acronyms **93**

Acknowledgements **95**

Affidavit **99**

Erklärung **101**

Abstract

The mammalian visual system is composed of several stages of stimulus feature extraction, distributed across multiple visual areas. Brain areas of the visual system are hierarchically organized from retina, to thalamus and superior colliculus, to primary visual cortex and higher visual areas. Each of these areas is uniquely adapted to perform specific computations on the visual information it receives. These computations arise through the anatomical arrangement of axons and dendrites, as well as experience dependent plasticity mechanisms, which form specific circuit motifs over the course of development. However, once these circuits are established, parts of this system remain plastic, allowing for some degree of adaptability. In this thesis, I will pose the following two questions. First, what are the connectivity rules in the visual thalamus, which result in visual channel segregation? I will focus on the convergence of eye-specific inputs to thalamic neurons as my model. Second, what is the stability of visual feature tuning in the primary visual cortex, and what are the factors that modulate their stability? Here, I will use orientation preference of layer 2/3 neurons as my model.

In the first study, I evaluated the convergence of retinal ganglion cell (RGC) inputs from the two eyes onto thalamocortical (TC) neurons in the dorsal lateral geniculate nucleus (dLGN) of the mouse. The canonical view of this brain region in mammals is that it maintains the separation of distinct visual channels. This includes the separation of information from the two eyes. In the past, several conflicting reports have been published on the level of such binocular convergence in the mouse. I employed a dual colour optogenetic input mapping approach and demonstrated that the level of binocularity of TC neurons is relatively low. This is because individual TC neurons receive disproportionately stronger input from one eye compared to the other. I next tested whether limited axodendritic overlap, between RGC axons and TC neuron dendrites, could explain this low level of binocular convergence. Although the segregation of RGC projections from the two eyes into two distinct zones does result in regions where ipsilateral dominant neurons are more numerous, limited axodendritic overlap cannot explain the low level of convergence onto individual neurons. Instead, synaptic selection and refinement prevents the mixing of information from the two eyes at this level of the mouse visual system.

In the second study, I investigated representational drift in the mouse primary visual cortex (V1), using chronic two-photon calcium imaging. Representational drift, the time dependent decrease in the similarity of neuronal responses to sensory stimuli, has been observed across multiple brain regions, including V1. However, so far, a specific tuning feature that undergoes such time dependent drift has not been demonstrated. Furthermore, a recent study showed that the frequency of exposure to an odour correlates with the stability of its representations in the olfactory cortex. My results demonstrate that the preferred orientation of neurons is one visual feature that undergoes time dependent representational drift. I then used cylinder lens goggles to alter the range of orientations a mouse experiences for several weeks, and found that this did not alter the drift rate of preferred orientation. Nevertheless, the distorted visual experience altered the direction of preferred orientation drift in favour of the experienced orientation, resulting in a shift of the overall distribution of preferred orientations. This suggests that ongoing representational drift may allow the visual system to adapt to changes in the statistics of the visual environment.

Taken together, in this thesis I explore how both anatomy and experience shape computations and their maintenance in the mouse visual system.

1. Introduction

1.1 Characteristics of the mouse visual pathway

The visual system of mammals has been explored in a variety of species over the last century and a half. While the classical animal models for mammalian vision have been cats and primates, in recent decades rats, mice, ferrets and tree shrews have become increasingly popular. In particularly the mouse has become widespread as a model of visual processing due to the suite of investigative tools available to mouse research, such as transgenics, viral delivery of genes, chronic calcium imaging and optogenetics. As the studies in this thesis were performed on mice, I will first give an overview of the most important characteristics of the mouse visual system and how it differs from that of other mammals. I will compare mice primarily to primates and cats, not just because they have been the classical models for mammalian vision, but also because mice are more closely related to primates than cats (Prothero, 2016), yet the visual system of primates and cats seem more similar to one another than compared to mice. These differences will be framed in an evolutionary setting in order to put the mouse visual system into the broader context of mammalian vision.

1.1.1 The retina and its projections

The retina is a complex multi-layered tissue that spans the inside of the eye and enables image detection. The structure of the retina is highly conserved across vertebrates and marks the beginning of the brains visual processing system.

The organization of the photoreceptor layer of the mouse, is characteristic of a nocturnal animal. Once light has passed through the eye and reaches the outermost layer of the retina, it hyperpolarizes photoreceptor cells. These photoreceptor cells come in two main types: rods and cones. Rods are more sensitive than cones and are therefore specialized to low light conditions, whereas cones are less sensitive but have a variety of colour sensitivities depending on the opsins (light sensitive proteins) they express. The mouse retina has a relatively high proportion of rod to cone cells. The rods and cones are relatively evenly distributed across the retina, with the overall density decreasing gradually towards the periphery (Jeon et al., 1998). This is in stark contrast to the retinas of diurnal primates and nocturno-diurnal domestic cats, which both have an area highly enriched in cones known as the fovea or area centralis, respectively. This area is roughly at the centre of the eye's optical axis (Steinberg et al., 1973; Packer et al., 1989; Grünert and Martin, 2020). Interestingly though, this local increase in cone density has receded in some nocturnal primates (Finlay et al., 2008). Furthermore, within two species of rodents, those that are diurnal have a more pronounced enrichment of cells in the central retina than their closely related nocturnal counterparts (Vega-Zuniga et al., 2013). It therefore appears that the presence and quality of the area centralis and fovea is a relatively flexible evolutionary trait in the mammalian retina. Overall, this results in mice being specialized to low light conditions but lacking high acuity vision in the central visual field.

Colour vision is limited in mice, compared to most primates, due to the lack of a red sensitive opsin. Mice have a green sensitive (M type) opsin and a UV sensitive (S type) opsin in their cone cells, but lack the red sensitive (L type) opsin that some primates have evolved. However, mice seem to have some degree of dichromatic vision in their ventral retina, or upper field of view, due to the differential arrangement of these opsins across the retina (Szél et al., 1992; Szatko et al., 2020). Interestingly, this reflects the high contrast between UV and green objects in the upper visual field

of natural scenes and may enhance their ability to detect birds of prey (Qiu et al., 2021).

In response to light, rods and cones modulate the amount of the neurotransmitter glutamate they release, to drive a network of neurons comprising of amacrine, bipolar, horizontal and finally retinal ganglion cells (RGCs), which send their axons to the brain. This network performs the first instance of neural computation in the visual pathway of vertebrates, as information is not passed unchanged from photoreceptor cells (input) to RGCs (output), but is combined in various ways to produce several distinct computations. This leads to a variety of RGC functional types (in mice >30; Baden et al., 2016). A key aspect what differentiates these RGC types is their receptive field (RF; the spatial position and arrangement of light stimuli on the sensory epithelium that changes the cell's firing). The typical RF shape of RGCs comprises a central region responsive to light intensity increases and a surround region responsive to light intensity decreases (ON-centre), or the inverse (OFF-centre; Kuffler, 1953). However, other aspects that differentiate RGC types cannot be described by a purely spatial RF. Instead some RGC types show selectivity to derivatives of the spatiotemporal light intensity changes that occur within a defined region, such as the direction of movement of a light spot or contour (direction selectivity, DS; Barlow and Hill, 1963; Barlow et al., 1964) or the orientation of a contour (orientation selectivity, OS; Levick, 1967). This diversity of RGC types represents a set of spatiotemporal filters that are applied to the image projected onto the retina.

Different types of RGCs project to different brain areas, as well as subregions within each brain area, leading to each region receiving a set of distinctly filtered images. ON-OFF direction selective RGCs for instance project exclusively to the superficial layers of the midbrain's superior colliculus (SC) and the dorsal lateral geniculate nucleus in the thalamus (dLGN; Huberman et al., 2009), while a subtype of intrinsically photosensitive RGCs projects primarily to the suprachiasmatic nucleus and enables photoentrainment (Chen et al., 2011).

In all mammals the majority of RGCs project to the contralateral hemisphere by crossing at the optic chiasm, while a species dependent fraction projects ipsilaterally. Due to the lateral placement of the eyes in mice, the part of the visual field that is seen by both eyes, the binocular visual field, is relatively small and largely confined to the upper visual field (Dräger, 1978). A small fraction of the RGCs in the ventrolateral crescent of the retina that receive light from the binocular field of view do not cross at the optic chiasm and instead project to the ipsilateral hemisphere (~3-5% of all RGCs; Dräger and Olsen, 1980; Mason and Slavi, 2020). This results in each hemisphere of the mouse brain receiving visual input form the entirety of the contralateral eye as well as some additional input from the ipsilateral eye's ventrolateral crescent. This organization is different from primates and to a large degree cats, as both have more ipsilaterally projecting RGCs, which decussate based on the naso-temporal division. Each hemisphere therefore receives visual input from the lateral half of the contralateral retina, the medial half of the ipsilateral retina and both foveae (Stone, 1983; Illing and Wässle, 1981). It would seem, therefore, that mice have little potential for binocular integration, but subsequent processing in dLGN and primary visual cortex (V1) enhances the ipsilateral eye's influence (Coleman et al., 2009).

A striking characteristic of mouse RGC projections is the dominance of projections to the SC. Around 88% of RGC axons project to the SC while only 25-50% project to the dLGN (Ellis et al., 2016). In contrast, in cats roughly 50% of RGCs project to SC (Illing and Wässle, 1981) and in primates only 5-10% of RGCs projecting to SC (Perry and Cowey, 1984). This suggests a much stronger involvement of mouse SC in visual processing, particularly compared to primates.

1.1.2 Superior colliculus

The SC is an evolutionarily ancient structure that integrates information from multiple sensory systems and controls movement in response to sensory cues. It is organized in an interconnected laminar structure with the superficial layers receiving visual input, the middle layers inputs from other sensory systems and the deeper layers primarily producing motor output signals (Isa et al., 2021). In primates, SC is involved in saccades, target selection and orientating (Schiller et al., 1987; McPeek and Keller, 2004), and there is evidence for the involvement of visually induced fear responses (Morris et al., 2001; Almeida et al., 2015). The mouse SC controls the identification and reaction to salient stimuli that are indicative of potential predators (looming stimuli; Shang

et al., 2015; Wei et al., 2015) and potential pray (small moving stimuli; Gale and Murphy, 2014; Hoy et al., 2019). This suggests that despite the disproportionate fraction of RGCs that project to SC between primates and mice, the role in visual processing is similar. However, the degree of dependence on the SC differs substantially between mice and primates (see section 1.1.5). Mice, in fact, more closely resemble non-mammalian vertebrates in this regard, and it has been postulated that mammals passed through a nocturnal bottleneck, allowing the rebalancing of inputs between SC and dLGN differentially across the mammalian orders (Kaas et al., 2021).

1.1.3 Dorsal lateral geniculate nucleus

Although in mice most RGCs project to SC, the dLGN projects to V1 and is therefore the primary source of information for visual computations in V1.

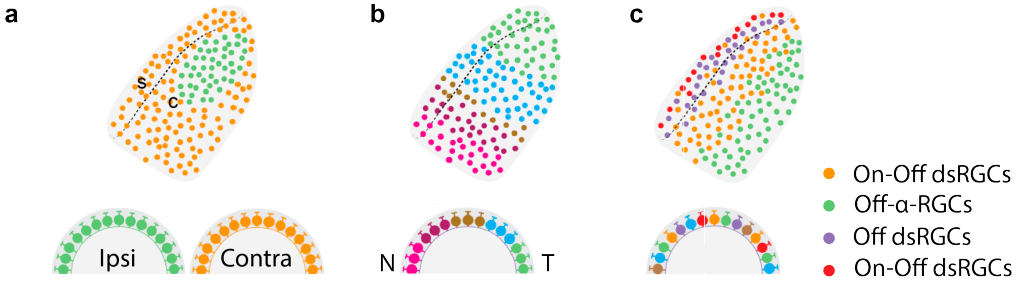

Figure 1.1: RGC input specificity to mouse dLGN. a) RGCs project from ipsi- and contralateral retinae (bottom) to separate projection regions within to dLGN (top). s: shell region, c: core region. b) RGCs project retinotopically, N: nasal T: temporal c) Different RGC types project to different overlapping subregions within the dLGN. Figure panel modified from Monavarfeshani et al., 2017.

The anatomy of the mouse dLGN is substantially different from both cats and primates in multiple ways. The dLGN of cats and primates is segmented into several distinct layers that are defined based on cytoarchitectural features and the RGC types that project to them. Cat dLGN is composed of three distinct layers (A, A1 and C); layer A receives contralateral inputs, layer A1 ipsilateral, and layer C input from both eyes. Three morphologically distinct thalamocortical (TC) projecting cell types (X, Y and W) receive input from different RGC types (X-cell, Y-cell and W-cell, respectively), but are interspersed among the three layers. Primate dLGN is also composed of multiple layers with each layer receiving either contralateral or ipsilateral inputs. Unlike in cats, however, the different layers contain different cell types with the magnocellular (M) and parvocellular (P) layers containing M or P cells, respectively (Stone, 1983; Kremkow and Alonso, 2018). The rodent dLGN on the other hand does not feature distinct cytoarchitectural layers but instead is composed of a shell and a core region. Both regions receive contralateral retinal input, while a subregion in the core exclusively receives ipsilateral input (Reese, 1988; Figure 1.1a). The retinotopic organization of dLGN runs roughly orthogonal to the shell-core border (Piscopo et al., 2013; Figure 1.1b), similar to the layers in cats and primates (Malpeli and Baker, 1975; Bishop et al., 1962). Much of the mouse dLGN core is innervated by non-direction selective OFF-α-RGC axons (Huberman et al., 2008). The shell, on the other hand, is innervated by direction selective OFF and ON-OFF RGCs along with inputs from SC (Kim et al., 2010; Osterhout et al., 2014), suggesting it to be functionally distinct from the core (Huberman et al., 2009; Grubb and Thompson, 2004; Piscopo et al., 2013; Cruz-Martín et al., 2014). However, other direction selective RGCs also innervate the dorsolateral half of the core as well as the shell (Kim et al., 2010) arguing against a clear functional division of shell and core, but rather suggesting overlapping zones of functional specialization (Figure 1.1c). In contrast to other mammals, the mouse dLGN therefore does not show true lamination but still has distinct, though overlapping, subregions.

As part of the so-called thalamic relay nuclei, the dLGN has traditionally been considered to simply “relay” information from retina to visual cortex (Chalupa and Williams., 2008). In cats and primates, the lamination of dLGN, the separation of RGC type and eye-specific projections, and

the specific connectivity between different RGCs and TC neuron types firmly establish one role of dLGN in these species as actively keeping RGC afferent streams segregated. In line with this view, TC neurons (also known as thalamic relay cells) in mice, generally respond best to ON-OFF centre-surround stimuli of roughly the same size as RGCs (Grubb and Thompson, 2003). Studies in recent years, however, have suggested varying degrees of convergence from different functional RGCs and RGC types (Hammer et al., 2015; Rompani et al., 2017; Rosón et al., 2019) and from both eyes (Howarth et al., 2014; Rompani et al., 2017; Sommeijer et al., 2017). This has raised the question whether, in mice, the dLGN performs a second instance of combinatorial computation prior to visual information reaching the cortex. This question will be explored in sections 1.2, 2.1, 3.1 and 4.1.

1.1.4 Primary visual cortex

The primary visual cortex of mammals is a retinotopically organized (Daniel and Whitteridge, 1961), laminated structure with stimulus selectivity indicative of widespread convergence of the small ON-OFF centre-surround receptive fields found in dLGN. This convergence of small receptive fields results in an increase in receptive field size (Siegle et al., 2021), the increased abundance of selectivity for oriented bars and edges, and direction selectivity (Hubel and Wiesel, 1959; Hubel and Wiesel, 1962).

Cat, primate and rodent V1 are all subdivided into 6 layers. Canonically, the cortical circuit of sensory areas is described as follows: layer 4 (L4) neurons receive thalamic input and send their output to L2 and L3 neurons; these are highly interconnected, and send their output to L5 and L6 neurons as well as other cortical regions; L1 is comprised of axons and dendrites; L5 neurons send their output to subcortical areas, while L6 neurons send their output to thalamus (Kandel et al., 2021). The exact connectivity, however, varies greatly between cortical regions and species. Mouse V1 deviates from the canonical circuit in the following ways. dLGN TC neurons project to L1 in addition to L4, where they connect onto L2/3 neurons (Cruz-Martín et al., 2014; Bickford et al., 2015). In primates and cats, L4 can be further subdivided based on TC cell type projections as well as differences in receptive field properties (Gilbert, 1983), whereas in mice no such subdivision of L4 is described. Similarly, L2 and L3 are not considered distinct layers in mice, as they are in primates. However, there is still a depth dependent gradient in visual stimulus preference and mRNA expression profiles of neurons in L2/3 (Niell and Stryker, 2008; O'Herron et al., 2020; Cheng et al., 2022; Weiler et al., 2022). Overall, this hints at a somewhat less laminated architecture of the mouse visual cortex compared to cats and, especially, primates.

A fundamental difference between rodent V1 and that of other mammals is the lack of periodic variation of some visual features on the cortical surface, such as the columnar organization of orientation preference in cats and primates (Hubel and Wiesel, 1962; Hubel and Wiesel, 1974). Mice, do not have orientation columns. Instead, cells with different preferred orientations (PO) are randomly arranged across the cortical sheet, forming a "salt-and-pepper" type organization (Ohki et al., 2005), though some evidence argues for the local clustering of cells with similar POs (Ringach et al., 2016). Mouse V1, despite having a region sub-serving the frontal visual field and responds to visual stimulation of either eye (binocular V1; bV1), does not show the ocular dominance column pattern observed in cat and primate (Hubel and Wiesel, 1962; Hubel and Wiesel, 1972; Dräger, 1974). This leads to the distribution of contralateral, ipsilateral and binocular responsive cells being relatively intermingled within the binocular region (Mrsic-Flogel et al., 2007). Overall, the mouse visual cortex shows a surprising lack of organization beyond its retinotopy when compared to non-rodent mammals (though recent studies have brought this into question: Ringach et al., 2016; Tring et al., 2022; Laing et al., 2015; Goltstein et al., 2022). The evolutionary reason for this characteristic is still not clear, with the two most prominent theories being that it is either due to the relative size of the retina compared to V1, regardless of species (Jang et al., 2020), or that it is a phylogenetic trait of rodents and lagomorphs, regardless of size (Schmidt and Wolf, 2021).

1.1.5 Higher visual areas

The next stage of information processing in the retino-cortical visual pathway is comprised of the higher visual areas (HVAs); cortical areas that receive direct input from V1, have a retinotopic organization and play distinct roles in visual processing.

In primates, the HVAs are divided into a dorsal and a ventral stream, which are involved in different functions for visual perception. The dorsal stream is involved in visual motion processing and visuomotor coordination, while the ventral stream is crucial for object recognition (Schneider, 1969; Mishkin and Ungerleider, 1982; Goodale and Milner, 1992). The dorsal stream of primates receives SC input, in addition to the cortical input, via the thalamic pulvinar nucleus, allowing for a limited degree of "unconscious" vision when V1 is damaged, known as blindsight (Pöppel et al., 1973; Weiskrantz et al., 1974). Similar segregation has also been found in cats (Lomber et al., 1996).

In mice, HVAs show distinct distributions of spatiotemporal tuning properties (Han et al., 2022), and tracing studies have given anatomical evidence for a segregation of HVAs into medial (putatively analogous to dorsal stream) and lateral (putatively analogous to ventral stream) areas (Wang et al., 2011; Wang et al., 2012). However, the assignment of areas to the two streams is still debated. The cortical HVAs include the: lateromedial (LM), laterointermediate (LI), posterior (P), postrhinal (POR), rostrolateral (RL), posteromedial (PM), anterior (A) and anteromedial (AL) areas. Some argue that the group of lateral HVAs, which include LM, LI, P and POR areas, anatomically and functionally belong to the "ventral" processing stream while the rest of the HVAs belong to the "dorsal" processing stream (Wang et al., 2011; Wang et al., 2012; Jin and Glickfeld, 2020; Goltstein et al., 2021). Others (Kaas et al., 2021) argue that in particular POR is part of the dorsal visual stream, due to the dominant drive of POR by SC via the lateral posterior nucleus (LP) of the thalamus (Beltramo and Scanziani, 2019; Bennett et al., 2019). Mouse SC does control aspects of object interaction and localization behaviours, akin to canonical dorsal stream functions seen in primates, via subcortical pathways (Isa et al., 2021). It seems however, that mouse SC additionally contributes to the lateral/"ventral" cortical visual stream involved in object recognition, via POR. This involvement in both object interaction and recognition explain the increased dependence of rodent vision on SC compared to primates (Kaas and Baldwin, 2019) and might be linked to the larger number of RGC projections to SC in mice and other rodents (see section 1.1.2).

It is important to stress that the use of vision by mice is specialized to their natural environment. This is reflected in the many anatomical differences across the visual pathway compared to other mammals, due to different evolutionary pasts and specialization to different biological niches. Despite this, mice are still able to perform well in many complex visual tasks (Morris, 1984; Hoy et al., 2019; Reinert et al., 2021) demonstrating the acute abilities of the mouse visual system.

1.2 Segregation of RGC afferent streams in the mouse dLGN

The mammalian dLGN has multiple anatomical attributes, which indicate it maintains the segregation of RGC afferent streams (or channels) before relaying them to the visual cortex. As mentioned above (section 1.1.1), the diverse RGC types in the mammalian retina represent a set of spatiotemporal filters. In effect, they produce separate spatiotemporally filtered images that are sent to image processing regions in the brain. The concept of RGC afferent stream segregation refers to mechanisms that prevent mixing of the different filtered images, and results in separate populations of neurons receiving and sending them. This type of connectivity is sometimes referred to as a labelled line. RGC afferent stream segregation implies a lower entropy state than the opposite extreme, complete mixing, suggesting that specific processes are necessary to construct and maintain it. Some of the anatomical and physiological features that point to these processes include: segregation of RGC type projections (Godement et al., 1984; Kim et al., 2010; Osterhout et al., 2014), cell type specific connectivity (Stone, 1983; Gilbert, 1983; Hamos et al., 1987) and sparse or heterogeneous synaptic weight distributions (Chen and Regehr, 2000; Litvina and Chen, 2017). Each of these features underlies a different potential mechanism, by which afferent stream segregation can be achieved. The dLGN has become a popular model for how molecular guidance cues and activity dependent refinement direct the development of these three segregation mechanisms. Here, I will summarize the evidence for each of these three mechanisms in the mouse dLGN and how they develop, in order to assess if the mouse dLGN fulfils the canonical role of RGC afferent stream segregation. I will then evaluate whether it also fulfils this role in the specific case of eye-specific segregation, which recent studies have called into question (Howarth et al., 2014; Rompani et al., 2017).

1.2.1 Projection zones: Development of the spatial segregation of RGC projections

The retinogeniculate input onto dLGN neurons is the first stage in the retinocortical pathway where information from different RGC types, and from both eyes, could theoretically converge. In some species, anatomical boundaries prevent this convergence from occurring. In primates, the parvocellular (P) and magnocellular (M) laminae receive eye-specific (either left of right eye) RGC projections. Furthermore, parvocellular RGCs (also called midget cells) project to the dLGN P lamina, while magnocellular RGCs (also called parasol cells) project to the dLGN M lamina (Stone, 1983). Segregation of RGC afferent streams is therefore largely achieved through the laminar structure in primate dLGN. In the dLGN of adult mice, projections from the two eyes are segregated into adjacent termination zones, and there is some separation in RGC afferent types between subregions, despite the lack of clear lamination (Godement et al., 1984; Kim et al., 2010; Osterhout et al., 2014; also see section 1.1.3). This suggests that, also in mice, the streams of information from both eyes and different RGC types are kept separate at this stage of the visual system. Here, I will outline how the functional organization of dLGN develops, relying first on molecular guidance cues followed by activity dependent refinement.

The mouse dLGN is segmented into a dorsolateral shell and a ventrolateral core which receive input from different RGC types (see section 1.1.3; Figure 1.1) that arrive in the dLGN at different stages. At around embryonic day (E)12 the first RGC projections reach the optic chiasm and decussate. Over the course of several days to weeks, different RGC types develop and project to various brain regions. The first axons reach dLGN befpre E16, but some of these early RGCs then retract from the dLGN while the axons of different RGC types arrive (Osterhout et al., 2014). Axons continue to arrive in the dLGN even after birth and, over time, the dLGN is innervated by a multitude of RGC types (Huberman et al., 2008; Kim et al., 2010; Rosón et al., 2019), most of which target specific but overlapping bands along the dorsolateral to ventrolateral axis (Figure 1.1). The development of this semi-laminated structure of RGC inputs is dependent on the arrival time of different RGC types and the expression of axon guidance markers such as Cadherins (Osterhout et al., 2014), but seems to be independent of retinal waves (spontaneously evoked patterns of activity in the developing retina; Huberman et al., 2008). However, a complete timeline of this development by the more than 30 RGC types is yet to be completed.

Compared to the semi-laminated RGC type innervation structure in mouse dLGN, the development of the eye-specific projection zones is somewhat delayed. At ~E14, a portion of RGC axons that reach the chiasm are repelled at the midline, via Ephrin signalling, and are redirected to the ipsilateral dLGN, where they arrive around postnatal day 0 (P0/E20/birth; Godement et al., 1984; Williams et al., 2003; Assali et al., 2014). These axons initially terminate in a large area within the dLGN, resulting in a shared termination zone of contra and ipsilateral projections. Ipsilateral axons then begin to retract from most of the dLGN until they remain only in a region of the mediodorsal dLGN, while contralateral axons retreat from this ipsilateral termination zone, resulting in a segregation of the two projections (Figure 1.1a) at around P8, before the eyes open (Godement et al., 1984). This process of eye-specific segregation is dependent on both Ephrin signalling and spontaneous retinal waves (Penn et al., 1998; Pfeiffenberger et al., 2005). Interestingly, induced retinal activity before eye opening only leads to eye-specific segregation, if the activity is uncorrelated between the two eyes (Zhang et al., 2012). This suggests that, the dependency of eye-specific segregation on retinal waves is due to the uncorrelated nature of such activity waves between the two eyes. The innervation and segregation of eye-specific projection zones in the dLGN is therefore a protracted process, which begins before birth and ends before eye opening, and depends on axon guidance cues as well as spontaneous retinal activity.

The development of the retinotopy of mouse dLGN follows a similar developmental pattern as that of the eye-specific RGC projection segregation. Notably, due to the small size of mouse dLGN and its three-dimensional organization, much of what we know about the development of the retinotopy of dLGN is based on studies from other species or from studies on the development of retinotopy in mouse SC. It was initially thought that retinotopic organization was preserved along the optic nerve in mammals (Polyak, 1957), however, this theory was later rejected (Horton et al., 1979; Guillery, 1995). This means that the highly specific retinotopic arrangement seen in the adult dLGN and SC (Reese and Jeffery, 1983; Piscopo et al., 2013; Dräger, 1975; Molotkov et al., 2022; Sibille et al., 2022) must be restored at some point after the optic chiasm. Soon after arrival in the target regions, and to some degree already in the optic tract, axons regain retiotopic organization (Simon and O'Leary, 1992; Guillery, 1995). However, retinotopically organized innervation in the SC, and probably the dLGN, is only coarse at birth. Over the next days, until eye opening at ~P12, the termination zones of individual RGC axon arbours are refined (Jeffery, 1985; Simon and O'Leary, 1992; Molotkov et al., 2022). As with eye-specific segregation, this process of initial course arrangement is achieved through Ephrin based molecular gradients, before activity dependent processes refine the organization (McLaughlin et al., 2003; Triplett and Feldheim, 2012; Assali et al., 2014). This retinotopic organization of the RGC axons results in the arrangement of TC neuron retinotopy (Reese and Jeffery, 1983; Piscopo et al., 2013; Molotkov et al., 2022).

Though there is anatomical specificity of RGC type and eye-specific projections in the mouse dLGN, this specificity of inputs is not necessarily sufficient for the segregation of RGC afferent streams. This is because the resulting effect of the segregation also depends on the size of the dendritic arbours of target TC neurons. If the arbours of the TC neurons are much larger than the width of specific RGC termination zones, then individual TC neurons could still synapse with multiple input sources. Indeed, in mice, TC neurons within the ipsilateral projection zone often have dendritic arbours that overlap both contra- and ipsilateral projection zones (Krahe et al., 2011). On the other hand, the semi-laminated RGC type innervation does seem to result in TC neurons in the dorsolateral portion of the dLGN showing higher direction and orientation selectivity (Piscopo et al., 2013). However, the effect of the geometric relationship between TC neuron dendrites and RGC projection zones on afferent stream segregation has so far not been investigated systematically. One of the questions I will address in this thesis is whether these geometric relationships can predict the eye specificity of TC neuron responses (section 3.1).

1.2.2 Cell types: Segregation through connection specificity

Beyond the segregation of RGC afferents into separate projection zones, other mechanisms of information stream division are conceivable. If specific RGC types predominantly synapse with specific TC neuron types, RGC afferent streams could be kept separate even without distinct RGC projection zones.

In cats and primates, TC neurons are subdivided into separate classes. In these species, different RGC types synapse with different TC neuron types within the dLGN. In primates, the P and M type TC neurons are separated in different lamina, receive different RGC type inputs, project to different lamina in V1 and can very clearly be separated based on the mRNA expression profiles (Stone, 1983; Gilbert, 1983; Bakken et al., 2021). Though cell type specific connectivity is present, it is unclear if RGC type to TC neuron type connectivity is dependent on cell type specific features beyond the TC neuron type and RGC afferent apposition discussed in the previous section. However, in cats the two electrophysiologically and morphologically distinct X-type and Y-type TC neurons, are interspersed, yet primarily receive input from either X or Y type RGCs, respectively (Stone, 1983; Gilbert, 1983). Hamos et al., (Hamos et al., 1987) found that a single X RGC axon arbour in Lamina A formed synapses with 3 X-type TC neurons and one Y-type TC neuron, out of 43 TC neurons in the volume. However, the single RGC arbour provided 100%, 49% and 33% of the total RGC inputs to the X-type TC neurons and only 2% to the Y-type TC neuron. This demonstrates cell type specificity of connections, but also that the degree of convergence of individual RGCs can vary dramatically, even within X-type TC neurons. This means that, at least in cats, separation of RGC afferent streams is at least partially mediated by cell type specific connectivity. The mechanisms of the cell type specific connectivity are unknown, but it could involve coincident timing of TC neuron type development and RGC type axon arrival, cell type specific molecular cues or activity dependent input selection.

In mice, the division of the dLGN cells into different TC types is not as clear. Though there is non-laminar segmentation of the mouse dLGN into shell and core based on RGC type and SC input, it is unclear if the cells in these two regions are classifiable into two distinct groups. Evaluating morphological traits is a common approach for classifying neuron types. Krahe et al., (Krahe et al., 2011; see also Bickford et al., 2015; Kerschensteiner and Guido, 2017) found three distinct morphological types, which resembled the morphologies of X-, Y- and W-type neurons in cats, that were enriched in different parts of the dLGN. However, they found no difference in electrophysiological characteristics of the three cell types. Furthermore, a second study, using electron microscopy, failed to identify separable groups of TC neuron morphologies despite sampling across an area where all three types should have been present (Morgan et al., 2016). Evaluating the expression of genetic markers is another method for classifying neurons. Calbindin positive TC neurons are more commonly found in the shell region (Grubb and Thompson, 2004). Taking a wider range of markers into account, however, shell and core TC neurons can genetically be classified as a single neuron type (Kalish et al., 2018; Bakken et al., 2021), with gradients of genetic marker expression (e.g. Ncab1 and Pvalb) running perpendicular to the shell-core boarder (Bakken et al., 2021).

Though there is some evidence for the presence of morphologically distinct TC neuron types in mouse dLGN, there is little evidence for genetically distinct types. If TC neurons in the mouse can indeed be classified into separable types, there would be the possibility that information streams from different RGC types are relayed in separate channels via these TC neuron types, similar to cats (Krahe et al., 2011). Given the inconsistency of reporting about the existence of TC neuron types in the mouse, the separability of TC neurons into distinct groups should be reassessed. In this thesis I will present data that further calls into question the separability of TC neurons into morphologically distinct groups (see sections: 3.1.4 and 4.2.3).

1.2.3 Synaptic weights: Segregation through sparse connectivity and heterogeneous synaptic weights

As described above, segregation of RGC afferent streams can be achieved through the anatomical separation of RGC projections and through the specificity of RGC type to TC neuron type connectivity. However, sparse connectivity to individual TC neurons, regardless of TC neuron type, could also achieve the segregation of RGC afferent streams; e.g. if TC neurons are homogenous in their development and genetics but their responsiveness is largely determined by very few RGCs. This could either be achieved through sparse connectivity (each TC neuron only connects to a small number of RGCs), or through sparse synaptic weights (TC neurons connect weakly to many RGCs, but a small number of synapses are disproportionately strong), or a combination of the two.

The most extreme form of this would be if each TC neuron receives input from only a single RGC (perfect relay), but in order to achieve RGC afferent stream segregation convergence of RGCs of the same type is sufficient. Limiting convergence of RGC types could take two forms: either, most of a cell's inputs originate from the same RGC type (structural relay), or a cell receives diverse RGC inputs, but those from a single type have disproportionately stronger synaptic weights (functional relay).

There is strong evidence that, in the mouse, TC neurons are connected to many RGCs. Using both electron microscopy and brainbow AAV (a technique that labels cell in diverse colour combinations, making it possible to distinguish cellular components belonging to different cells; Cai et al., 2013), it has been shown that two forms of retinogeniculate synaptic structures exist. One, in which a large synapse is formed between a single RGC and one TC neuron (simple encapsulated), and one in which multiple RGCs synapse in close proximity on a TC neuron dendrite (complex encapsulated; Hammer et al., 2015; Morgan et al., 2016; Liang et al., 2018). This finding was corroborated using single cell retrograde rabies tracing (Rompani et al., 2017), which showed that TC neurons could be innervated by 1 to 91 RGCs of between 1 and 9 RGC cell types. These data show that perfect relay and structural relay modes do exist in the mouse, but they are not the norm.

Despite the evidence for a high level of RGC number and RGC type convergence in the mouse dLGN, there is also substantial evidence that the synaptic weight distribution becomes increasingly heterogeneous over the course of development. In a series of experiments, Chen et al. (Chen and Regehr, 2000; Hooks and Chen, 2006; Lin et al., 2014; Litvina and Chen, 2017) demonstrated that, initially, TC neurons receive many RGC inputs that are weak and have a low AMPA receptor (AMPAR) to NMDA receptor (NMDAR) ratio. This is interesting because AMPARs and NMDARs are glutamate neurotransmitter receptors with different contributions to synaptic function. AMPAR are fast conducting ion channels that induce synaptic transmission (Watkins and Evans, 1981). NMDARs, on the other hand, are ion channels that require coincident presynaptic glutamate release, D-serine/glycine (Papouin et al., 2012), and postsynaptic depotentiation to induce postsynaptic calcium influx. Calcium influx through NMDARs induces the unsilencing and potentiation of synapses through AMPAR insertion (Collingridge et al., 1984; Bliss and Collingridge, 1993; Isaac et al., 1995; Liao et al., 1995). Chen et al., found that over the course of several weeks after around eye opening, many of these connections are eliminated, while the strength of the remaining synapses, and their AMPAR to NMDAR ratios, are non-uniformly increased (Chen and Regehr, 2000; Jaubert-Miazza et al., 2005). This process is dependent on retinal waves during the early phase and normal visual experience later on (Hooks and Chen, 2006; Hooks and Chen, 2008). At the end of this process of developmental refinement, TC neurons on average receive 10 functional RGC inputs, of which only 1-3 dominate the postsynaptic activity (Litvina and Chen, 2017). This heterogeneity in synaptic weights makes the possibility of functional relay more likely.

Taken together, these findings suggest that although TC neurons may receive some level of input from many RGC afferents, only a small number of synapses could define the response properties of a postsynaptic TC neuron. This is in line with a recent *in vivo* study that demonstrated that visually driven TC neuron activity could be modelled by the summation of just 1 to 5 RGC neuron types, with only two dominating the input (Rosón et al., 2019). It seems, therefore, that mouse dLGN shows an intermediate level of RGC afferent stream segregation through functional relay. However, it remains unclear how the different mechanisms (projection segregation, input selection, and heterogeneous synaptic) contribute to afferent stream segregation and how this differs across species.

1.2.4 The specific case of eye-specific convergence

The ability to combine information from two sensors has multiple advantages: redundancy in the case of failure, an increase in spatial coverage, increase in signal to noise and inference of signal source location when the spatial relation of the sensors is considered. This holds true for the advantages of combining information from two eyes, known as binocular integration. Understanding how binocular integration happens in the brains of various animals, therefore, gives us a window into how biological neural circuits may leverage two complementary sensors. As the mouse has

increasingly become a popular model of mammalian vision, many aspects of binocular integration in the mouse visual system have been explored. By now, it is well established that behaviourally relevant binocular computations occur in the mouse brain (Dräger, 1975; Scholl et al., 2013; Samonds et al., 2019; Boone et al., 2021). At what stage in the visual system these computations occur is not entirely understood. Anatomically, the first instance where information from both eyes could theoretically be combined is at the retinogeniculate and retinocollicular synapses.

According to the canonical view, that dLGN relays RGC afferent streams to visual cortex, there should be little integration of contra- and ipsilateral input by TC neurons. Though it is not entirely clear if the dLGN of mice fulfils this function to the same extent as in other mammals, the segregation of eye-specific RGC projections suggests that at least for binocular convergence this canonical view may hold. However, the evidence for or against binocular convergence at the retinogeniculate synapse is even less consistent than for the convergence of RGC types summarized above. The first *in vivo* recordings of adult mouse dLGN neurons performed while presenting monocular and binocular visual stimuli, found no binocular cells (39 contra- and 12 ipsilateral responsive cells; Grubb and Thompson, 2003). This was corroborated a few years later using *in vitro* stimulation of the optic nerves while patch clamping dLGN neurons in ~P19 mice (Jaubert-Miazza et al., 2005), although with a small sample size of only 8 neurons. In a follow up study from the same lab (Žiburkus and Guido, 2006), it was then shown that the proportion of binocular cells measured using this *in vitro* method, decreased from ~66% at p0-14 to ~17% at P15-21 (althought this was done in rats). However, a lack of experiments in older mice leaves uncertainty if this proportion decreases further beyond P20. Roughly 10 years later, an *in vivo* study was published that found widespread binocularity and no cells that were only responsive to ipsilateral visual stimulation. This extremely high level of binocularity was not reduced after cortical feedback to dLGN was inhibited (Howarth et al., 2014). This was followed by a retrograde rabies input tracing study that also found no dLGN neurons that exclusively received ipsilateral RGC inputs (Rompani et al., 2017). Further *in vivo* studies were published that showed varying fractions of binocularly responsive neurons across a range of recording and visual stimulation methods (Jaepel et al., 2017; Sommeijer et al., 2017; Huh et al., 2020). Despite a wide range of measured binocularity, these findings ultimately resulted in the view that mouse dLGN performs binocular integration through convergence at the retinogeniculate synapse (Zeater et al., 2015; Wallace et al., 2016; Rose and Bonhoeffer, 2018; Kerschensteiner and Guido, 2017; Liang and Chen, 2020).

These divergent studies have prompted me to assess the level of binocularity in the mouse dLGN. In this thesis, I will investigate the extent of binocular retinogeniculate convergence onto TC neurons. I propose that eye-specific retinogeniculate convergence in the mouse dLGN should be reassessed for several reasons. Firstly, there are substantially conflicting estimates on the level of binocularity in mouse dLGN, and accurate estimates are necessary for our understanding of binocular integration in the mouse visual system. Secondly, high binocularity together with the seemingly high level of convergence of RGC types either suggests a markedly different role of mouse dLGN compared to other mammals, or the level of RGC channel segregation in other mammals has been overestimated. Thirdly, RGC convergence, including eye-specific convergence, has been an important model for the development of specialized circuits in the mammalian brain. Understanding the interaction of the different mechanisms that contribute to the adult circuit is a pre-requisite to understanding its development.

1.2.5 Aims and objectives

Canonically, the mammalian dLGN maintains the segregation of RGC afferent streams, relaying information from retina to visual cortex. Recent studies have called into questions, whether the mouse dLGN aligns with this view. In particular, several studies have implicated that information from both eyes are combined at the level of the retinogeniculate synapse, resulting in higher than expected levels of functional and structural binocularity of thalamocortical (TC) neurons (Howarth et al., 2014; Sommeijer et al., 2017; Rompani et al., 2017). However, these reports contradict a number of other studies (Grubb and Thompson, 2003; Jaubert-Miazza et al., 2005; Jaepel et al., 2017; Huh et al., 2020). In part of this thesis (sections 2.1, 3.1 and 4.1) I aim to reconcile these seemingly contradictory findings using data from a dual-colour optogenetic input mapping approach. With this method, the evoked postsynaptic activity of TC neurons is measured in response to independent stimulation of RGC inputs from the two eyes. I also aim to evaluate to what extent eye-specific RGC axon segregation, synaptic input selection and eye-specific synaptic strengthening contribute to the segregation or integration of information from the two eyes.

1.3 Representational stability and adaptability in the visual system

In order to operate, the brain's sensory systems must fulfil two seemingly opposing functions. On the one hand, they must reliably sense, represent, relay and interpret the environment, and on the other, refine representations and adapt interpretations when necessary, in order to enable appropriate actions. I define these two functions of sensory systems as representational stability and representational adaptability. Representational stability relies on the consistent response of networks of neurons in reaction to stimulus exposure, while representational adaptability requires that the same sensory stimuli can evoke different neural activity over time. Due to the lack of chronic single cell activity measurements until recently, the canonical view of stability and adaptability of sensory systems has been seen through the lens of anatomy and the macro-organization of functional maps. Hence, stability has been viewed as a passive process (the lack of connectivity changes), while adaptability as active (targeted connectivity changes). Here, I will review the extent of representational stability and the effect of chronic visual perturbations on the developing and adult visual cortex.

1.3.1 Stability of structured projection patterns and macro-organization

Neurons in the visual cortex are highly interconnected. It has long been known that their interconnectivity is organized in a like-to-like connectivity pattern governed by the general principle that neurons who share selectivity to visual features are more likely to be synaptically connected (Gilbert and Wiesel, 1989). I will refer to groups of neurons that are highly interconnected, due to a shared tuning property, as like-to-like microcircuits (LLM). In this context, the term LLM is necessarily loose as there are many different visual features that may determine connection probability between neurons. Additionally, most features are continuous rather than discrete, suggesting LLMs are often not discrete. The entire connectivity of V1 neurons could therefore only be described by a very high dimensional structure with a multitude of connectivity probability rules. LLMs are simply portions of this structure, composed of highly connected neurons that share similar tuning across one of many visual stimulus features. In order to reliably and continuously represent the visual scene, the tuning of neurons to visual features must be constant, and so also their position within this high dimensional connectivity structure. How the position of neurons in this connectivity structure is maintained is therefore a fundamental question. Some of the rules that govern this connectivity structure are determined by the structure of afferent input to V1. This is because the structure of short- and long-range projections can limit which neurons are able to connect with one another. In other words, physical proximity of axons and dendrites is a pre-requisite for communication among neurons in a biological neural network. To understand the restrictions that physical proximity between neurons in the visual system imposes on the stability of the marco-organisation of V1, I will first outline the concept of information availability with respect to the functional maps of retinotopy, ocular dominance and orientation tuning. I will then evaluate if and when during development axons and dendrites stop growing and the general anatomy of the visual system becomes less plastic, and how this process leads to functional map stabilization in the absence of perturbations.

The retinotopic organization of TC projections to V1 is established by the time of eye opening in mammals (Espinosa and Stryker, 2012). This is largely in parallel to the organization of RGC projections to dLGN, outlined in section 1.2.1 (e.g. retinotopy, semi-laminar innervation by different RGC types and eye-specific projection zones). Similar to retinothalamic projections, the retinotopic organization of TC projections is dependent on molecular guidance cues, e.g. Ephrin signalling, as well as spontaneous activity (Cang, Kaneko, et al., 2005; Cang, Rentería, et al., 2005). This organization results in limited retinotopic scatter of TC neuron boutons at a given cortical location (Roth et al., 2016). Depending on the extent of the dendritic arbours of recipient cortical neurons, this means that most of the thalamocortical information directly available to a recipient neuron is limited to some portion of visual space. Local and long range corticocortical projections from primary and higher visual areas are also retinotopically organized, but to a lesser degree (Marques et al., 2018). As long as the dendritic arbour size of V1 neurons does not increase and the TC

and intracortical axons do not dramatically reorganize, the available input to the neurons remains functionally limited. Even if synaptic modifications occur and a neuron connects to a different set of TC projections in its vicinity, its receptive field cannot shift far.

In mammals that have ocular dominance columns, e.g. cats and primates, the segregation of TC projections to L4 of V1, by eye dominance, also restricts the availability of information from the two eyes. Ocular dominance columns are formed by the segregated projection of TV neurons to V1 (Hubel and Wiesel, 1972; Shatz et al., 1977). Moreover, the dendritic arbours of L4 spiny stellate neurons close to OD column borders are asymmetrically biased, avoiding columns of the opposite eye (Katz et al., 1989; Kossel et al., 1995). This presumably enhances the effectiveness of eye-specific segregation of TC projections, by further restricting a cell's access to axons responsive to the eye of the neighbouring ocular dominance column. Using repeated intrinsic optical imaging, it has been demonstrated that the locations of these OD columns are stable over many months (Shtoyerman et al., 2000), suggesting this restriction in input availability is stable over time.

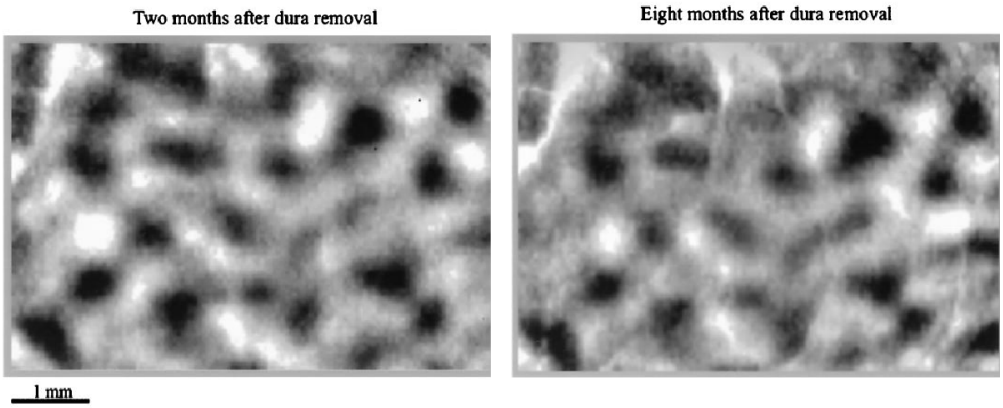

Figure 1.2: Stable orientation preference patches in primate visual cortex. Intrinsic optical signal response map of one orientation, recorded 6 months apart. Dark regions correspond to a decrease in the intrinsic signal (reflection of red light), which corresponds to an increase in neuronal activity when the visual stimulus is presented (here a drifting square grating). The relative positions of the patches that respond to one particular orientation are largely conserved over eight months, demonstrating long-term stability of the orientation map in primate V1. Figure from Shtoyerman et al., 2000.

Orientation preference is thought to be calculated *de novo* in V1 through the spatial alignment of TC receptive fields (Hubel and Wiesel, 1962) and/or ON-OFF subfield segregation (Lee et al., 2016) and is organized in a pinwheel patters in V1 of cats and primates (Bonhoeffer and Grinvald, 1991). How this structure arises, is less clear as with ocular dominance columns. One study (Jin et al., 2011), found that the RF position of ON and OFF responsive TC axons in a local area predicted the local orientation preference of V1 neurons. Unlike for ocular dominance however, there is no bias in the organization of dendrites of V1 neurons with respect to the orientation pinwheel structures (Levy et al., 2014). Nevertheless, the structure of orientation preference maps may be determined by TC projection organization. Additionally, some studies suggest that cortico-cortical axons preferentially target iso-orientation domains (Gilbert and Wiesel, 1989; Schmidt et al., 1997; Buzás et al., 2001; Buzás et al., 2006; though see Martin et al., 2014). The stabilization of these TC and inter-orientation domain projections could explain why the location of orientation columns is largely stable over time, similar to ocular dominance maps (Chapman et al., 1996; Sengpiel et al., 1998; Shtoyerman et al., 2000; Figure 1.2). Eye-dominance and orientation preference in animals possessing feature tuning maps, could therefore be stabilized through the restriction of available input, as long as major dendritic and axonal remodelling does not occur.

It turns out that dendrite and axon structures are generally stable in adult V1 under baseline conditions. Studies that have quantified the dynamics of dendrites and axons in the adult cortex of mice, found that dendritic arbours of excitatory neurons do not undergo remodelling (Lee et al., 2006), and the motility of axon branches of TC neurons is limited to tens of microns (Paola et al., 2006; Stettler et al., 2006). The stability of axons and dendritic branches may therefore

be a sufficient explanation for why functional maps, resulting from the organization of long-range projections (both TC and cortico-cortical), are stable over time. Under which circumstances axon and dendrite arbours may remodel, and lead to changes in these macro-organizations, will be outlined in section 1.3.3.

1.3.2 Single cell representational stability

The dependence of V1 cortical maps on the organization of TC projections may explain the stability of retinotopy, ocular dominance and orientation maps in mammals that have such maps. Even if cortical neurons experience large or even complete synaptic turnover, the restriction in the availability of inputs in their vicinity would result in similar tuning, assuming that the long-range projection organization remains unchanged. In rodents, which have lower levels of feature organization across V1 (e.g. no orientation pinwheels), synaptic turnover on cortical neurons would likely result in drastically altered tuning properties. Functional maps derived by techniques such as intrinsic optical imaging can only measure the combined tuning and stability of large populations of neurons if they are organized spatially. To understand the consequences of the lack of feature tuning maps in mice, single cell measurements are crucial.

The stability of functional maps in sensory cortices (Shtoyerman et al., 2000; see section 1.3.1), reinforces the idea that basic sensory processing is stable in the absence of interventions. This makes sense if the role of sensory systems is to reliably and consistently extract and represent features relevant to the interpretation of, and reaction to, the sensory environment. In visual cortex, similarly tuned neurons form LLMs. For some visual features, these LLMs can be stabilized through anatonical constraints (see 1.3.1). In the mouse, despite its salt-and-pepper organization of orientation and ocular dominance, similar LLM connectivity has also been found for orientation and direction preference (Ko et al., 2011; Ko et al., 2013; Ko et al., 2014). In addition, many dendritic spines (structures that harbour synapses) survive for weeks (Keck et al., 2008; Hofer et al., 2009), suggesting that even in the absence of visual feature maps, LLMs, and therefore tuning properties of single cells, could be stable. Two-photon microscopy (Denk et al., 1990) and genetically encoded calcium indicators (Miyawaki et al., 1997; Chen et al., 2013) have made this hypothesis testable through repeated neuronal activity monitoring over many weeks.

Repeated measurements of the activity of individual neurons in V1 indicated very little long-term cumulative change over several days to weeks across a range of visual features, including orientation preference, ocular dominance and spatial frequency preference (Mank et al., 2008; Chen et al., 2013; Rose et al., 2016; Jeon et al., 2018). This is in contrast to the instability of neuron place fields (when a neuron is tuned to specific location in space) in higher brain areas such as hippocampus and posterior parietal cortex (Ziv et al., 2013; Driscoll et al., 2017). This was, in part, attributed to the fact that dendritic spine dynamics show more turnover in hippocampus compared to sensory areas (Attardo et al., 2015). In general, the lack of consistency in the response properties of neurons in higher brain areas across days was coined representational drift (Clopath et al., 2017; Rule et al., 2019). In this thesis, I define representational drift to specifically refer to a decrease in tuning similarity of neurons as a function of time, that cannot be attributed to trial-to-trial response variability.

Despite the general consensus that visual cortex neurons represent visual features consistently across long periods of time, Montijn et al. (Montijn et al., 2016) compared the pairwise signal correlation (PSC; correlations of the tuning curves between all pairs of neurons) in V1 in response to drifting gratings. The PSC values were then correlated across days. If cells do not change their tuning properties across days, then the similarity between the PSCs of different days should remain constant. Contrary to the canonical view of stable representation in primary sensory areas the PSC correlation decayed as a function of time, but did not approach zero within the one-month experiment. A similar effect was observed in the pairwise noise correlation matrix, which represents not the stimulus response similarity of neurons, but the similarity in trial-to-trial variance that is thought to reflect the functional connectivity structure of a population of neurons. This indicates that some tuning properties and the network activity correlation structure gradually changes, but does not completely reorganize in the time frames tested to-date. In other words, V1 neurons undergo constrained representational drift as well as functional connectivity drift, though it is

unclear exactly which tuning properties change. Later studies also repeatedly presented natural movies and found greater instability to these more naturalistic stimuli across short (minutes to hours) and long (days and weeks) time intervals (Deitch et al., 2021; Marks and Goard, 2021). This suggests that the core tuning properties of neurons are relatively stable, but other unknown spatiotemporal modulators may be less stable.

A certain level of instability in neuronal tuning properties and population representations have also been found in other sensory areas. A recent study using two-photon imaging in mouse auditory cortex found that the frequency preference of neurons, as well as their complex sound preference, changes over the course of just a few days (Aschauer et al., 2022). In olfactory cortex, chronic electrophysiological recordings have also shown that the representation of odours changes as a function of time (Schoonover et al., 2021). In whisker somatosensory cortex (barrel cortex), the whisker selectivity of neurons has been reported to change across days (Margolis et al., 2012) and the whisker stimulation frequency decoding accuracy from a population of neurons is higher within a day compared to across days (Mayrhofer et al., 2015). In the aforementioned publications, the fact that stimuli could be decoded across days was interpreted to mean that neuronal representations of stimuli are stable. However, under the definition of representational drift that I am using here, the difference in stimulus tuning and decrease in decoding accuracy across days does constitute representational drift. Comparing the magnitude of drift rates across sensory areas is, at this point, likely not possible, since the absence of equivalent stimulus tuning features makes comparisons of neuronal tuning or neuronal stimulus response similarity relatively arbitrary. For instance, comparing the drift rate of whisker stimulation frequency tuning, visual orientation selectivity, odour selectivity and place field position in different neurons makes little sense. Nevertheless, it seems that the phenomenon of representational drift is present across sensory cortices as well as higher cortical areas.

In summary, in mouse visual cortex the single cell representation of features is mostly stable, but the overall similarity of tuning curves partially decays over days. Visual cortex neuronal responses to naturalistic stimuli show more representational drift than responses to drifting gratings. Although representational drift of visual response properties has been demonstrated by the drift of PSC of responses to drifting gratings and tuning curve correlation of responses to natural stimuli, it is unclear which spatiotemporal tuning features are actually drifting. Finally, the presence of drift across a number of sensory and higher cortical areas suggests that this is a widespread phenomenon, at least in the mouse, and likely a fundamental aspect of cortical coding.

1.3.3 Experience-dependent plasticity in the visual system

There are many aspects of vision that are unlikely to change within the lifetime of an animal. Trivially, left is left, down is down, the right eye is on the right, the world is dichromatic (if you're a mouse), and visual scenes contain contours of varying orientations. Other aspects, such as the visual acuity of our eyes, the faces of our friends and sometimes the alphabets that we read change multiple times within our adult life. While representational drift (outlined in the previous section) usually refers to changes that are ongoing under ordinary conditions, experience-dependent plasticity refers to the brain's ability to adapt to such changes in environmental factors. This is of course a very loose definition that could encompass many aspects of brain function, from the adaptation to the loss of an eye, a new sport, a twisted ankle or a particularly badly placed curb on our way to work. Experience-dependent plasticity can also refer to developmental processes that are affected by sensory experience, as well as adaptation during adulthood. In this thesis, I will investigate and discuss the encoding of visual features in V1 and how these remain the same or change in response to persistent alterations in visual scene statistics. To contextualize the perturbations I use in this thesis and aid the later interpretation of my results, I will give an overview of the most common experience-dependent plasticity paradigms that are thought to induce connectivity and coding changes in V1.

One of the earliest and most infamous visual experience-dependent plasticity paradigms that have been performed was the application of image inverting goggles by George Stratton in 1896. George Stratton wore goggles that inverted the visual scene of one eye for 8 consecutive days, while covering the other, and described his subjective experience (Stratton, 1896; Stratton, 1897). The

question he posed was, "Is the inverted image [of the visual scene as projected on to the retina] a necessary condition of our seeing things in an upright position?". In other words, if the visual scene is permanently flipped upside-down, does the brain adjust, to the point where upside-down is perceived as right-way-up, and right-way-up is perceived as upside-down? Stratton found that after a few days, instead of perceiving the world as upside down, he perceived his body to be upside down, but that this feeling was not constant.

> "[When] full attention was given to the outer objects, these frequently seemed to be in normal position, and whatever there was of abnormality seemed to lie in myself, as if head and shoulders were inverted and I were viewing objects from that position, as boys sometimes do from between their legs." (Stratton, 1896)

It can be debated if this fulfils the constraints of 'perceiving' the world as right-way-up, but it has since become clear that visuomotor coupling and oculomotor reflexes can adapt to such manipulations over time (Linden et al., 1999). In terms of processing in the early visual system, the question can be framed differently: do the anatomical and functional characteristics of the early visual system, up until V1, change in response to image inversion in adults? Perhaps unsurprisingly, the retinotopic organization of V1 is not affected. Furthermore, illusions that test perception of shape based on illumination and shading patterns are interpreted as they fall on the retina, rather than as they would appear without the manipulation (Linden et al., 1999). This is likely because millions of years of evolution, in which the sun is overhead, has shaped the visual system to assume the normal location of illumination. Experiments in juvenile and adult cats and monkeys have suggested that similar perturbations to the visual field tend to induce a deterioration of the tuning of V1 neurons (Sugita, 1996; Singer, Tretter, et al., 1979; Singer, Yinon, et al., 1979). Interestingly, in adult mice, a shift of the visual field of one eye by 20° caused a relative shift between the contra- and ipsilateral retinotopic maps, but not enough to compensate for the visual field shift completely (Yoshitake et al., 2013). In general, it is therefore clear that although experience is necessary for the correct development of retinotopy (see 1.3.1), experience alone is not able to dramatically alter the retinotopic organization of V1 in adults.

Possibly the most widely used experience-dependent plasticity paradigm in visual neuroscience is monocular deprivation (MD). In 1963, Wiesel and Hubel discovered that closing one eye of a young cat led to a shift in the distribution of ocular dominance of cells in V1, in favour of the open eye (Wiesel and Hubel, 1963a). This effect was not observed in older cats. This demonstrated the presence of a developmental critical period for binocular vision, during which intact sensory experience is needed for normal development. During the critical period for ocular dominance in cats, and primates, MD causes permanent structural changes. These include changes in retinothalamic axon arbours (Sur et al., 1982), dLGN lamination (Wiesel and Hubel, 1963b; Guillery and Stelzner, 1970) and thalamocortical projections (Hubel et al., 1977; Shatz and Stryker, 1978; Tieman, 1984; Antonini and Stryker, 1993; Antonini and Stryker, 1996), resulting in the enlargement of the ocular dominance columns of the open eye, at the expense of those of the closed eye. It was later found that young mice, also exhibited shifts in the distribution of ocular dominance in V1 after MD (Dräger, 1978; Gordon and Stryker, 1996), resulting in permanently reduced responsiveness to stimuli presented to the previously deprived eye. This is accompanied by an increase in the arborization of nondeprived eye TC projections, similar to cats (Antonini et al., 1999). The closure of this critical period is marked by a reduction in axon motility (Paola et al., 2006; Stettler et al., 2006), a stabilization of the extracellular matrix (Pizzorusso et al., 2002) and an increase in inhibitory neuron activity (Hensch, 2005). The critical period for ocular dominance is crucial for the alignment of eye-specific visual tuning properties in cells that receive input from both eyes, as well as computations that necessitate the interaction of information from both eyes, such as disparity tuning. For this reason, critical period MD also prevents the matching of preferred orientation between the eyes of binocular neurons (Wang et al., 2010) and decreases overall disparity selectivity (Scholl et al., 2017). This demonstrates not only a reduced influence of the deprived eye on V1 activity, but also an impaired ability to combine information from the two eyes appropriately. In general, these findings paint the picture that unlike the development of retinotopic maps, which require retinal waves that are largely uncorrelated between the two eyes, the development of binocular vision requires the experience of correlated vision between the two

eyes after eye opening.

In adult cats, MD fails to cause ocular dominance shifts (Wiesel and Hubel, 1963b), likely because the retinothalamic and thalamocrotical projections are not reorganized. Interestingly, however, mice still show ocular dominance shifts after MD later in life, particularly if they are housed in enriched environments and if deprivation is maintained for longer than 4 days (Sawtell et al., 2003; Greifzu et al., 2014). Axonal sprouting has not been reported to occur after MD in adult mice, but tracking spine and axon dynamics in V1 neurons showed that substantial rewiring occurs (Hofer et al., 2009; Sammons et al., 2018). However, the original network configuration is not lost, as individual cells return to their original tuning after the deprived eye is reopened (Rose et al., 2016). Although it is unclear why, ocular dominance plasticity is able to persist well into adulthood for mice, but not in cats.

Some experience-dependent plasticity paradigms aimed to understand the adaptability of V1 coding by completely silence a specific group of neurons within the visual system, rather than changing the statistics of visual experience from outside of the central nervous system. This includes retinal lesions that involve the destruction of RGCs within a localized area. The retinogeniculate projections within the lesion projection zone of the dLGN are lost completely, and, while surviving, TC cells within this region become permanently insensitive to visual stimulation (Gilbert and Wiesel, 1992). The corresponding region in V1 also becomes silent as local neurons no longer have access to axonal inputs that drive coordinated activity. After some time, however, V1 neuron axons from the surrounding retinotopic area grow into the lesion projection zone and neurons become responsive to visual stimulation again, but now with shifted receptive fields (Gilbert and Wiesel, 1992; Yamahachi et al., 2009; Keck et al., 2008). TC projections, on the other hand, do not remodel during this time (Darian-Smith and Gilbert, 1995). The adaptation to retinal lesions is therefore mediated by cortical remodelling.

Another classical experience-dependent plasticity paradigm is the restriction of vision to contours of one orientation, often referred to as stripe rearing. This is a particularly interesting paradigm because it targets a specific visual tuning property of cortical V1 neurons, namely preferred orientation. The remaining orientation, shown to the animal as stripes in a cylindrical enclosure or using cylindrical lenses mounted in front of the eyes, is referred to as the experienced or permitted orientation. As with MD, it was first used to investigate the development of orientation preference in young animals. By exposing young cats to lines of just one orientation, it was found that the distribution of orientation preferences in V1 was dramatically shifted in favour of the experienced orientation (Blakemore and Cooper, 1970; Hirsch and Spinelli, 1970). If the two eyes were exposed to different orientations, fewer binocular cells were found and the orientation preference of a cell was determined by the experienced orientation of its dominant eye (Hirsch and Spinelli, 1970; Stryker et al., 1978). This bias in the number of cells tuned to the experienced orientation was also reflected in the orientation maps, as measured using intrinsic optical signal imaging. Here, the cortical area responsive to the experienced orientation was increased compared to normally raised cats (Sengpiel et al., 1999). Additionally, the receptive fields were elongated along the axis of the experienced orientation (Sasaki et al., 2015). Strikingly, when adult cats (above P50) were exposed to contours of just one orientation for 2 weeks, the orientation map was largely unaltered (Tanaka et al., 2009). I speculate that the lack of an increase in the representation of the experienced orientation in adult cats could be due to the presence of orientation maps along with a lack of TC projection reorganization in adults, but not kittens, preventing reorganization of these maps in adulthood (see 1.3.1). In mice and rats, on the other hand, the effect of stripe rearing induces an over-representation of the experienced orientation in both young and adult animals (O'Hashi et al., 2007; Kreile et al., 2011), though the effect is weaker in mice beyond ~P60 (Yoshida et al., 2012). It is still unclear if the change in the distribution of neurons observed in adult mice is due to neurons changing their preferred orientation, or if deprived neurons become inactive while others become newly tuned in a way that shifts the population distribution in favour of the permitted orientation.

In summary, visual neuroscience has utilized a number of different manipulations to visual experience in order to elucidate the mechanisms of experience dependent plasticity in the mammalian visual system. These include global transformations of the visual scene, occlusion of one eye, focal lesions to the retina and restriction of perceived orientations, and many that I have not covered in

this short overview. These manipulations were crucial in the discovery of critical periods during development and the ability of the brain to rewire through spine and bouton turnover as well as axon motility to adjust to new environmental conditions. It has also become clear that in the adult brain there is a strong tendency for cells to retain their original tuning, or return to their original tuning after the perturbation is reversed. How the V1 network manages to retain much of its original tuning structure in the face of these perturbations, especially in the absence of anatomical constraints on single cell tuning, remains to be elucidated.

1.3.4 Aims and objective

Neurons in the mouse visual cortex are thought to maintain their tuning to basic visual features. However, the similarity of neuronal response to visual stimuli decreases as a function of time. Given this decrease in tuning similarity over time, some aspects of stimulus tuning are bound to undergo representational drift. Here, I will measure and quantify the stability or drift of the preferred orientation of mouse V1 neurons over several weeks. I will then test the hypothesis that continued experience of the preferred visual features of a neuron is necessary for the stability of its tuning. This will be done by chronically implanting cylinder lens goggles to alter the statistics of the visual environment of mice for several weeks.

2. Materials and Methods

2.1 Materials

2.1.1 Viruses

Resource	Supplier	Identifier
AAV2/2.Syn-ChrimsonR.tdT	Klapoetke et al., 2014; Supplied by University of Pennsylvania Vector core (USA)	Addgene: 59171
AAV2/2.Syn-Chronos.EGFP	Klapoetke et al., 2014; Supplied by University of Pennsylvania Vector core (USA)	Addgene: 59170
AAV2/1.1CamKII0.4.Cre.SV40	Supplied by University of Pennsylvania Vector core (USA)	Addgene: 105558
AAV2/1.Syn.Flex.mRuby2.GSG. P2A.GCaMP6s.WPRE.SV40	Rose et al., 2016; Supplied by University of Pennsylvania Vector core (USA)	Addgene: 68720
AAV2/1.Syn.GCaMP6s.WPRE.SV40	Chen et al., 2013; Supplied by University of Pennsylvania Vector core (USA)	Addgene: 100843
AAV2/1.Syn.mRuby2.GSG.P2A. GCaMP6s.WPRE.SV40	Rose et al., 2016; Supplied by University of Pennsylvania Vector core (USA)	Addgene: 50942

2.1.2 Antibodies

Resource	Supplier	Identifier
Rabbit anti-Calbindin D28k	Swant (Switzerland)	RRID: AB_10000340
Goat anti-Rabbit-Alexa-647	Thermo Fisher Scientific (USA)	RRID: AB_2535812
Guinea Pig anti-RBPMS	Millipore (USA)	MAB5324
Goat anti-Guinea Pig Alexa-647	Thermo Fisher Scientific (USA)	A21450

2.1.3 Reagents

Resource	Supplier	Identifier
Rapi Clear 1.47	SunJin Lab Co. (Taiwan)	RC147001
Triton X-100	Sigma-Aldrich Chemie GmbH (USA)	T8787
Alexa-594	Thermo Fisher Scientific (USA)	A10438
FluoSave Reagent	Millipore (USA)	345789-20ML
Bicuculline	Sigma (Missouri, USA)	14340

2.1.4 Surgical reagents and drugs

Resource	Supplier
Rimadyl	Zoetis (USA)
Xylocain Pumpspray	AstraZeneca GmbH (Germany)
Fentanyl	HEXAL AG (Germany)
Midazolam-ratiopharm	Ratiopharm (Germany)
Medetomidine Dormitor	Orion Pharma (Finland)
Naloxon-ratiopharm	Ratiopharm (Germany)
Flumazenil-HEXAL	HEXAL AG (Germany)
Atipamezol	Orion Pharma (Finland)
Braunol 7.5	B. Braun Melsungen AG (Germany)
Histoacryl	B. Braun Surgical (Spain)
Pattex Ultra Gel	Henkel AG & Co. KGaA (Germany)
Ultrasound Gel	P.J. Dahlhausen & Co. GmbH (Germany)
Paladur	Heraeus Kulzer GmbH (Germany)
Sterofundin	B. Braun Melsungen AG (Germany)
Isopto-Max	Alcon Pharma GmbH (Germany)
Oculotec	Novartis (Switzerland)

2.1.5 Surgical equipment: Intravitreal injections

Resource	Supplier	Identifier
Hamilton syringes	Hamilton Company (USA)	Model 75 RN SYR
32G blunt needles	Hamilton Company (USA)	Small hub RN needle
Stereotaxic apparatus	MPI of Neurobiology inhouse workshop (Germany)	Custom built
Micromanipulator	World Precision instruments (USA)	M3301R
Homeothermic blanket with rectal probe	Harvard Apparatus (USA)	HB101
Dissecting microscope SOM-62	Karl Kaps GmbH (Germany)	SOM-62
Hot glass-bead sterilizer steri 350	Sigma (USA)	Z375858EU
Infra-red lamp	Glamox Luxo GmbH (Germany)	
Paper points.02	Müller & Weygandt GmbH (Germany)	100 649
Dumont #7 11271	Fine Science Tools GmbH (Germany)	11271-30
Dumont #5/45 Cover Slip Forceps	Fine Science Tools GmbH (Germany)	11251-33

2.1.6 Eye dissection equipment

Resource	Supplier	Identifier
Stemi dissection microscope	Zeiss (Germany)	SV 6
Microscissors	Fine Science Tools GmbH (Germany)	15003-08
Dumont #5/45 Cover Slip Forceps	Fine Science Tools GmbH (Germany)	11251-33
Dumont #7 11271	Fine Science Tools GmbH (Germany)	11271-30
Cosmotop-spin paint brush size 1	Da Vinci (Germany)	4 017505 11310 5580
Millicell 0.4 µm filter paper 30mm	Merck KGaA (Germany)	PICM0RG50
Filter paper 70mm	Whatman (UK)	1001-070
Omnifix 3ml syringe	B. Braun Melsungen AG	4617022V
24-well plate	TPP (Switzerland)	Z707791-126EA
Microscope slides 76x26 mm	Carl Roth (Gemrany)	1879
Menzel glass clover slides 18x18 mm	VWR (Germany)	630-1842
iSpacer 0.15 mm deep	SunJin Lab Co. (Taiwan)	IS101

2.1.7 Surgical equipment: Craniotomy, virus injections and cranial window implantation

Resource	Supplier	Identifier
Homeothermic blanket with rectal probe	Harvard Apparatus (USA)	HB101
Stereotaxic apparatus	MPI of Neurobiology inhouse workshop (Germany)	Custom made
Dissecting microscope SOM-62	Karl Kaps GmbH (Germany)	SOM-62
Hot glass-bead sterilizer steri 350	Sigma (USA)	Z375858EU
Dumont #7 11271	Fine Science Tools GmbH (Germany)	11271-30
Dumont #5/45 Cover Slip Forceps	Fine Science Tools GmbH (Germany)	11251-35
Dumont #5/45C Cover Slip Forceps	Fine Science Tools GmbH (Germany)	11251-33
Scalpel handle	Fine Science Tools GmbH (Germany)	10007-12
Scalpel blades	Fine Science Tools GmbH (Germany)	10015-00
Drill bits HM1 005	Meisinger (Germany)	2000001204005
Dental drill (Presto II)	NSK (USA)	
Sugi® versatile cellulose sponge material Sterile	Kettenbach Medical (Germany)	31603
Gelfoam stypro	Curasan (Germany)	9350000020
Omnican 50 syringe	B. Braun Melsungen AG (Germany)	91511117S
Omnican-F syringe	B. Braun Melsungen AG (Germany)	9161406V
Glass capillaries for virus injections (Ø: 0.8 mm, wall thickness: 0.28 mm)	Hilgenberg (Germany)	1408472
Micropipette puller for virus injection pipettes, P-97 Flaming/Brown	Sutter Instruments (USA)	P-97
Parafilm	Sigma-Aldrich Chemie GmbH (Germany)	P7793
Pressure micro-injection system	Toohey Company (USA)	
Pulse generator/trigger Master-8	A.M.P.I (Israel)	Master-8cp
Glass coverslips, round, Ø: 4 mm, thickness: 0. 13 mm	Glaswarenfabrik Karl Hecht GmbH & Co. KG (Germany)	92100101020
Glass coverslips, round, Ø: 10 mm, thickness: 0. 13 mm	Glaswarenfabrik Karl Hecht GmbH & Co. KG (Germany)	41001110
Infra-red lamp	Elstein (Germany)	IOT 150

2.1.8 Two-photon imaging setup

Resource	Supplier
Bergamo 2, benchtop two-photon microscope	Thorlabs (Germany)
Fibre Coupled LED, 530 nm	Thorlabs (Germany)
Fibre Coupled LED, 470 nm	Thorlabs (Germany)
Fibre Coupled LED, 735 nm	Thorlabs (Germany)
1500 MonoChrome Camera	Thorlabs (Germany)
MaiTai HP DeepSee Ti:Sapphire laser	Spectra-Physics (USA)
Pockels cell controller, 302RM	Semrock (USA)
6210H galvanometer scanner, 6 mm mirror	Cambridge technology (USA)
GSI 8kHz resonant scanner	Cambridge technology (USA)
P-726 PIFOC® High-Load Objective Scanner	Physik Instrument (Germany)
Custom notched primary 2P dichroic, longpass 405/473-488/561/705-1600	Semrock (USA)
CFI75 LWD, 16x, 0.8 NA water immersion objective	Nikon (Japan)
Dichroic mirror/beam splitter 560 nm	Conoptics (USA)
Bandpass filter 525/50-25 nm	Semrock (USA)
7-bandpass filter 607/70-25 nm	Semrock (USA)
Short pass filter 720/25 nm	Semrock (USA)
GaAsP photomultiplier tubes, H7422P	Hamamatsu (germany)
PCI digitizer ATS9440, 14bit, 125 MS/s, 4 channels	Alazartech (Canada)
ScanImage 4.2	Vidrio Technology (USA)
Homeothermic blanket with rectal probe	Harvard Apparatus (USA)

2.1.9 Analysis software

Resource	Supplier
MatLab 2018a/2014b	Mathworks (USA)
PsychToolbox	Brainard, 1997; Pelli, 1997; http://psychtoolbox.org /download
Python 3	Rossum and Drake, 2009
ScanImage r4.2	Vidrio Technology (USA)
Ephus	Vidrio Technology (USA)
Suite2P	Pachitariu et al., 2017; https://github.com/MouseLand/suite2p
Fiji (Fiji is just ImageJ)	Schindelin et al., 2012; RRID: SCR_002285
TREES toolbox	Cuntz et al., 2010
Simple Neurite Tracer plugin	Schindelin et al., 2012
LAS X program	Leica Microsystems (USA)

2.1.10 Solutions

2.1.10.1 Cortex buffer

Ingredient	Concentration
NaCl	125 mM
KCl	5 mM
Glucose	10 mM
HEPES	10 mM
$CaCl_2$ + $2H_2O$	2 mM
$MgSO_4$ + $7H_2O$	2 mM
Note:	pH adjusted to 7.4

2.1.10.2 Phosphate-buffered saline (PBS)

Ingredient	Concentration
NaCl	137 mM
KCl	2.7 mM
Na_2HPO_4	8 mM
KH_2PO_4	1.5 mM
Note:	pH adjusted to 7.4

2.1.10.3 Cutting Solution

Ingredient	Concentration
NaCl	85 mM
Sucrose	75 mM
KCl	2.5 mM
Glucose	25 mM
NaH_2PO_4 + H_2O	1.25 mM
$MgCl_2$	4 mM
$CaCl_2$	0.5 mM
$NaHCO_3$	24 mM
Note:	Osmolarity adjusted to 310-325 mOsm; 95% O2 +5% CO2 bubbled

2.1.10.4 Artificial cerebrospinal fluid

Ingredient	Concentration
NaCl	127 mM
KCl	2.5 mM
Glucose	10 mM
$CaCl_2$	2 mM
$MgCl_2$	2 mM
NaH_2PO_4 + H_2O	1.25 mM
Note:	Osmolarity adjusted to 310-325 mOsm; 95% O2 +5% CO2 bubbled

2.1.10.5 Caesium-based internal solution

Ingredient	Concentration
$CsMeSO_4$	122 mM
$MgCl_2$	4 mM
HEPES	10 mM
Na-ATP	4 mM
Na-GTP	0.4 mM
Na-L-ascorbate	3 mM
Na-phosphocreatine	10 mM
EGTA	0.2 mM
QX-314	5 mM
Alexa-594	0.03 mM
Note:	pH adjusted to 7.4; Osmolarity adjusted to 295-300 mOsm

2.1.10.6 Blocking buffer

Ingredient	Added to PBS
Normal Gaot Serum	10%
Triton X-100	2%
Sodium Azide	0.2%

2.1.10.7 Antibody buffer

Ingredient	Added to PBS
Normal Gaot Serum	1%
Triton X-100	0.2%
Sodium Azide	0.2%

2.1.10.8 Washing buffer

Ingredient	Added to PBS
NaCl	2%
Triton X-100	0.2%

2.2 Methods

2.2.1 Eye-specific optogenetic input mapping in mouse dLGN

All animal experiments were conducted in accordance with the Max Planck Society guidelines as well as those of the local government (Regierung von Oberbayern). These following protocols are also described in Bauer et al., 2021.

2.2.1.1 Intravitreal eye injection

Mice (P30-48) were anaesthetized using a mixture of Fentanyl (0.05 mg/kg), Midazolam (5 mg/kg) and Medetomidine (0.5 mg/kg), injected intraperitonially. After checking for anaesthesia depth using the toe pinch reflex, the mice were fixed in a stereotaxic apparatus and 0.5 mg/kg of Carprofen was administered subcutaneously. All surgical equipment was heat sterilized and rinsed with ethanol. Throughout the procedure the eyes were kept moist using eye drops (Oculotec, Novartis). Two separate 32 gauge Hamilton syringes were rinsed with ethanol and distilled water before front filling each with a different virus (AAV2/2.Syn-ChrimsonR.tdT or AAV2/2.Syn-Chronos.EGFP). A small hole was created medial to the corneo-scleral junction using a sharp 0.4 mm syringe tip, while securing the eye with forceps. The virus loaded Hamilton syringe tip was inserted at an oblique angle into the hole using a micromanipulator (M3301R, WPI). The angle of the syringe tip insertion was optimized to avoid damaging the lens. 1-2 µl of virus was injected into the eye and the syringe tip left in place for ~4 min. After removing the syringe tip the eye was covered with eye cream (Isopto-Max, Alcon Pharma). The procedure was repeated with the other eye using the second virus filled Hamilton syringe. Anaesthesia was ended using a mixture of Naloxone (1.2 mg/kg), Flumazenil (0.5 mg/kg) and Atipamezol (2.5 mg/kg). Carprofen (0.5 mg/kg), was administered on the following two days. ChrimsonR-tdTomato and Chronos-EGFP were allowed to express for 5-9 weeks before the animals were used for *in vitro* experiments.

2.2.1.2 Acute Brain slice preparation

Mice were anaesthetized using isoflurane (2%) and decapitated. The brain was removed from the skull and sliced into 320 µm sections (using a vibratome) while immersed in cold cutting solution. After incubating the slices for at least 45 min at 34 °C in cutting solution the brain slices were immersed in ACSF at ~21 °C until use (< 12 hours).

2.2.1.3 Eye-dissection and retinal flat mount preparation and imaging

After removing the brain from the skull, the eyes were removed and transferred to cold ACSF. Microscissors were used to separate the lens from the eye cup (cornea and retina), and the lens was inspected for damage. Vitreous humor was removed and the eye cup was transferred to 4% paraformaldehyde (PFA) for 20-60 min. The retina was then removed from the eye cup, cleaned of debris and attached to a Millicell 0.4 µm cell culture insert (PICM0RG50) using light suction, applied using a 0.1 ml Omnifix-F syringe (Braun) with the tip cut off. A subset of the retinas were subsequently stained for RBPMS (a RGC marker) and imaged to check for transduction efficiency. The retinas were rinsed and fixed again in 4% PFA for 15-30 min after which they were stored in PBS at 4 °C. The retinas were later incubated in blocking buffer for 1 hour at room temperature before incubating with Guinea-Pig anti-RBPMS antibodies (ABN1376, 1:1000 in antibody buffer) overnight at room temperature. After washing out the antibodies three times for 15 min with PBS, the retinas were incubated with the secondary anti-Guinea-Pig Alexa-647 antibodies (A21450, 1:200 in antibody buffer) for 90 min. They were then washed, post-fixed in 4% PFA for 15 min, washed again in PBS and then mounted on glass slides with 150 µm spacers and embedded using FluoSave Reagent (Millipore). The embedded retinas were imaged using a commercial confocal microscope (Sp8, Leica) equipped with a 20x 0.75 NA objective (HX PL APO L 20x/0.75 IMM CORR CS2). The slices were illuminated at 488, 561 and 633nm sequentially (using an argon-ion laser, a diode pumped solid state laser and a Helium-Neon laser, respectively) to evoke fluorescence in EGFP (indicator for Chronos), tdTomato (indicator for ChrimsonR) and Alexa-647 (indicator

for RBPMS). Image stacks were acquired at 1024 x 1024 pixels with 0.54 x 0.54 x 1 µm voxel size. In the example retinas shown in Figure 2.1, over 90% of cells labelled with RBPMS were labelled with GFP-Chronos or Chrimson-tdTomato.

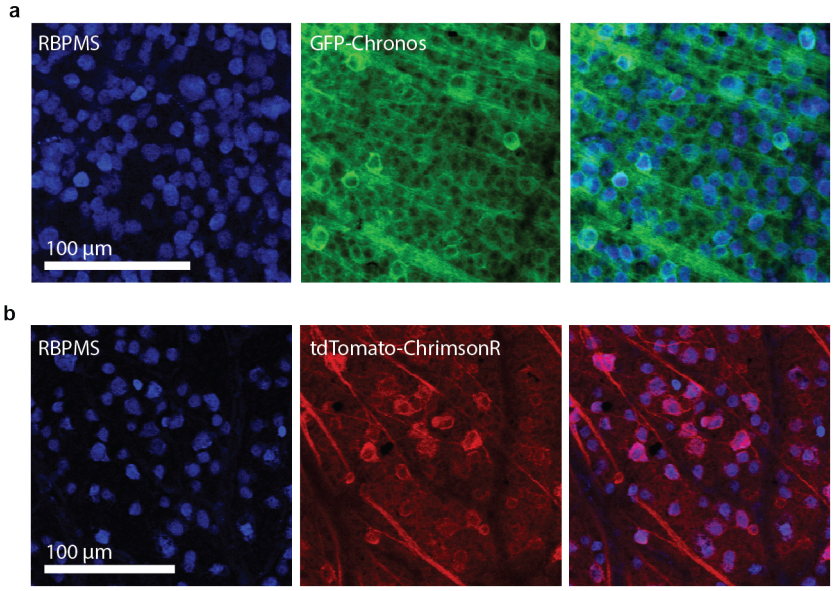

Figure 2.1: Example confocal images of Chronos-EGFP and ChrimsonR-tdTomato transduced retinas. a) Example confocal image of flat mounted retina from Chronos-EGFP transfected retina. left, RBPMS antibody stain (blue); middle, EGFP fluorescence (green); right, combined. b) ChrimsonR-tdTomato transduced retina (from the same mouse as a). left, RBPMS antibody stain (blue); middle, tdTomato fluorescence (red); right, combined.

2.2.1.4 *In vitro* electrophysiological recordings of thalamocortical neurons and optogenetic stimulation of RGC axons

Brain slices containing dLGN were mounted on poly-D-lysine coated coverslips and moved to a perfusion chamber filled with ACSF containing bicuculline (20 µM) at room temperature. Borosilicate glass patch pipettes with 4-5 MΩ were filled with caesium-based internal solution (containing Alexa-594 for visualization of dendritic morphologies) and used to patch-clamp putative thalamocortical neurons in whole-cell configuration. Excitatory post synaptic currents (EPSCs) were measured using a Multiclamp 700 B amplifier (Axon Instruments) and digitized at 10-20 kHz. The brain slices were photo stimulated using 473 and 637 nm light provided by two separate lasers (S3FC473 and S4FC637, Thorlabs). RGC inputs from the two eyes were assessed using a two-step protocol based on the sequential photo-stimulation approach described by Hooks et al. (Hooks et al., 2015). As ChrimsonR can be activated by both blue and red light, the sequential photo-stimulation protocol was necessary in order to first deactivate the ChrimsonR with red light before stimulating the Chronos with blue light. Once a neuron was patch-clamped it was illuminated with 11 light pulses (50 ms, 473 nm) at increasing light intensities ranging from 0-3 mW/mm^3. The blue light intensity that induced the largest EPSC in the patch-clamped neuron was used for the second protocol. In the second protocol, sequential illumination with 637 nm and 473 nm (250 ms red pulse followed by a 50 ms blue pulse) was used with 11 increasing red-light intensity steps from 0-5.1 mW/mm^3. Both of these protocols were applied at -70 and +40 mV membrane holding potential.

The dendritic morphologies of the patch-clamped neurons were imaged using an A-scope two-photon system (Thorlabs) equipped with a MaiTai DeepSee laser (Spectra Physics), 16x NA 0.8 immersion objective (Olympus), 20x 1.0 NA and 40x 0.8 NA objectives (Olympus) and GaAsP photomultiplier tubes (PMTs; Hamamatsu). Alexa-594, with which the cells were filled, was excited at 810 nm and imaged at 1024 x 1024 pixels (0.3 to 0.8) x (0.3 to 0.8) x 1.2 µm voxel size. Several overview image stacks of the EGFP and tdTomato labelled RGC axons were also acquired using

940 nm excitation, at multiple magnifications. These were used to identify the location of the recorded neurons in the Allen common coordinate framework (ACCF; Wang et al., 2020) as well as the subsequently acquired confocal image stacks.

2.2.1.5 Brain slice clearing and confocal imaging

After dual-colour optogenetic input mapping, brain slices were stored in 4% PFA at 4 °C. Brain slices were subsequently washed three times for 10 min before incubating in permeabilization buffer overnight at 4 °C. They were then transferred to blocking buffer for 8 hours at room temperature before incubation with rabbit anti-calbindin antibodies (Swant CB-38a, 1:2000 in antibody buffer) for one night at room temperature and 3 days at 4 °C. The slices were washed in PBS overnight and then incubated with secondary anti-rabbit Alexa-647 antibodies (Thermo Fisher A21244, 1:2000) for 2 days at 4 °C. The slices were washed with washing buffer and PBS before incubation in RapiClear 1.47 (SunJin Lab Co.) for 3 hours and then embedded in RapiClear 1.47 on a cover glass with a 300µm spacer.

The embedded brain slices were imaged using a commercial confocal microscope (Sp8, Leica) equipped with a 20x objective (HX PL APO L 20x/0.75 IMM CORR CS2). The slices were illuminated at 488, 561 and 633 nm sequentially (using an argon-ion laser, a diode pumped solid state laser and a Helium-Neon laser, respectively) to evoke fluorescence in EGFP (indicator linked to Chronos), tdTomato (indicator linked to ChrimsonR) and Alexa-647 (indicator for RBPMS). Multiple stacks of dLGN were acquired at 1.64x1.64x4 µm voxel size and stitched together post-hoc using the LAS X program (Leica).

2.2.1.6 Dual-colour optogenetic input mapping analysis

The current traces were first baseline subtracted individually for each optogenetic stimulation repetition, using the 100 ms pre-stimulation period. The response amplitude was determined as the maximum current between 3 and 30 ms (107 ms at -40mV holding potential) after red light or blue light onset. At +40 mV holding potential an exponential was fit to the red light induced EPSC and subtracted from the trace before measuring the blue light induced EPSC. A cell was considered responsive to stimulation of Chronos or ChrimsonR transduced RGCs if the EPSCs of the last 6 blue or red pulses (of the 11-step sequential photo stimulation ramp protocol) were significantly above baseline (based on a signed-rank test threshold of $p < 0.05$). If the neuron was significantly responsive to light of both colours, the ocular dominance index (ODI) based on dual-colour sequential photo-stimulation was determined as:

$$ODI = \frac{EPSCpeak_{\text{contra}} - EPSCpeak_{\text{contra}}}{EPSCpeak_{\text{contra}} + EPSCpeak_{\text{contra}}}$$

Where EPSC peak was the blue and red evoked EPSC (corresponding to ipsi- or contralateral RGCs), for the stimulation step that evoked the largest red evoked EPSC. If a cell was not significantly responsive to either red or blue light stimulation, the respective response amplitude was considered 0 pA. This process was applied separately for the step protocols at -70 and -40 mV holding potential.

2.2.1.7 Dendritic morphological reconstruction and analysis

The two-photon image stacks of the Alexa-594 filled neurons were traced using the Simple Neurite Tracer plugin (Schneider et al., 2012) for ImageJ. Dendritic reach was defined as the maximum distance from soma centre to dendritic branch tip and total dendritic reach was defined as the sum of all internode distances. Maximum Sholl crossing (Sholl, 1953) was computed using the TREES toolbox (Cuntz et al., 2010), and is the sphere around a cell (in 20 µm increments) with the highest number of branch crossings. Dendritic orientation index (DOi) was calculated as defined in Krahe et al., 2011.

For further analysis, I first 3D interpolated the traced dendritic trees. The dendritic trees were then transformed to match the orientation of the confocal image stacks of the dLGN it came from. The confocal image stacks were aligned to the right dLGN of the ACCF. This meant that for

all subsequent analyses the dendritic morphologies were done with respect to both the ACCF (and therefore corresponded to comparable anatomical coordinates) as well as the local fluorescence gradients around each cell. Since the dLGNs were oriented in the coronal plane, the x, y and z coordinates corresponded to left-right (or medial-lateral), superior-inferior (or dorsal to ventral) and anterior-posterior (or rostral-caudal). Dendritic asymmetry direction and orientation was calculated in the coronal plane as:

$$A\,\mathrm{sym}_{\mathrm{dir}} = \arctan 2(\bar{y}, \bar{x})$$

$$A\,\mathrm{sym}_{\mathrm{ori}} = \arctan(\bar{y}/\bar{x})$$

Where $\bar{x}$ and $\bar{y}$ are the means of x and y positions (relative to soma centre) of all interpolated dendritic tree nodes. The asymmetry magnitude was then calculated as:

$$\mathrm{Asym}_{\mathrm{mag}} = \left| \frac{2 \cdot \sum_{p=1}^{n} \left(x_p - (y_p / \tan\left(-1 \cdot \mathrm{Asym}_{\mathrm{ori}}\right)) > 0\right) - n}{n} \right|$$

Where p denotes the node number and n the total number of nodes. Dendritic elongation was based on principle component analysis and was derived from a similar metric by Morgan et al., 2016. Elongation orientation was defined as:

$$Elong_{ori} = \arctan(v_{(pc1,y)}/v_{(pc1,x)})$$

Where $v_{(pc1,x)}$ and $v_{(pc1,y)}$ are the x and y coefficients of the eigenvector for principle component one. Elongation magnitude was defined as:

$$Elong_{mag} = 1 - (expvar_{(pc2)}/expvar_{(pc1)})$$

Where $expvar_{(pc1)}$ and $expvar_{(pc2)}$ are the explained variances of the first two principle components.

Hartigan's dip test (Hartigan and Hartigan, 1985) was subsequently used to test for multimodality in the distributions of these different morphological metrics.

2.2.1.8 Registration of TC neuron location in confocal stacks and Allen-common-coordinate-framework

The position of recorded neurons was reidentified in the confocal image stacks by either identifying the Alexa-594 filled soma or by comparison to the local RGC innervation patter (EGFP and tdTomato) in the two-photon image stacks acquired on the day of the experiment. The contours of the dLGN were also marked in the confocal stacks. The green and red channels of the confocal image stack (each corresponding to fluorescence from RGCs of either the ipsi- or contralateral eye) were then used to calculate the normalized fluorescence difference (FD) by applying the following formula on a pixel by pixel basis:

$$FD = \frac{F_{\mathrm{contra}} - F_{\mathrm{ipsi}}}{F_{\mathrm{contra}} + F_{\mathrm{ipsi}}}$$

For the binarized FD stacks, a 3D Gaussian filter ($\sigma = 64$µm) was applied to each channel of the two-colour confocal stacks before the pixel wise FD values were computed. The FD values were then binarized (FD < 0 set to -1 and FD > 0 set to 1).

A 10 µm voxel resolution ACCF was downloaded from http://data.cortexlab.net/allenCCF/. This contained pixel wise anatomical region identity, including dLGN, dLGN shell and ipsilateral projection zone of dLGN. The confocal image stacks were rotated and scaled to match the ACCF in 3D. As the position of the neuron in the confocal stacks had been determined previously this gave an estimate of the position of a neuron in the ACCF.

The original data from Piscopo et al., (Piscopo et al., 2013; generously provided by the Niell Lab) were used to generate a visuotopic map of dLGN with respect to the ACCF. This data contained receptive field centre positions (in visuotopic coordinates) of 257 dLGN units, as well as

the medio-lateral and dorso-ventral position of corresponding electrodes in one of three coronal dLGN schematic outlines. These schematics were manually aligned (using custom Matlab code) to the ACCF, resulting in estimates of the unit positions within the ACCF. The aligned receptive field azimuth and elevation data were then interpolated (and extrapolated) in 3D, resulting in a 3D map of dLGN retinotopy. A similar procedure was performed using the dual-colour optogenetic input mapping derived ODI. First the ODI was binarized in order to reduce it to eye preference (ODI < 0 set to -1 and ODI > 0 set to 1) before interpolating and extrapolating in 3D. For the map of monocularity, the absolute ODI of each neuron was taken. To generate a map of eye preference and monocularity across visual space, each neuron was given an estimated visuotopic and azimuth position derived from the corresponding interpolated 3D maps.

2.2.1.9 Ratiometric fluorescence quantification and analysis

In order to estimate the relative availability of ipsi- and contralateral RGC afferents to recorded TC neurons, or at random points across dLGN slices, two metrics were used. Radial mask-based FD (rFD), was derived by generating a spherical density mask based on the radial distribution of dendritic densities from all traced neurons. This mask could then be applied to the FD stack at the location of each neuron, to give the weighted average of FD values around that neuron. The same mask was applied in a 40µm grid pattern across binarized FD stacks. The morphology-based FD (mFD), was derived by generating a spherical density mask for each neuron, where each pixel value denoted the density of dendrites in that location. This morphology-based mask was applied to the FD stack at the location of a given neuron, to give the weighted average of FD values around that neuron. In order to investigate the effect of dendritic orientation on the relative availability of ipsi- and contralateral afferents, the morphology-based mask was also rotated in 10° increments and the mFD value recalculated. If more than 10% of a neuron's dendrites protruded out of the dLGN boundaries at any rotation angle, the neuron was not included in analysis pertaining to mFD after rotation.

In order to calculate the discriminability (d') of mFD distributions of ipsi- and contralateral neurons the following formula was used:

$$d' = \frac{meanFD_c - meanFD_i}{\sqrt{\left(\sigma FD_c^2\left(n_c - 1\right) + \sigma FD_i^2\left(n_i - 1\right)\right) / \left(n_c + n_i - 2\right)}}$$

Where n_i and n_c are the numbers of ipsi- and contralateral neurons, $meanFD_i$, $meanFD_c$, σFD_i and σFD_c are the mean and standard deviation of ipsi- and contralateral neuron mFD values, respectively. The 95% confidence interval of d' was calculated using bootstrap resampling across ipsi- and contralateral neurons independently. To test if d' was different when mFD was based on the true morphology of a neuron rather than a when the morphology was rotated by 180°, bootstrapped distributions of mFD for both cases were obtained to calculate the p-value for the two-sided test for difference between d' from both cases:

$$p = \min\left(\frac{1}{10,000}\sum_{bsh=1}^{10,000}\Delta d'(bsh) \geq 0, \quad \frac{1}{10,000}\sum_{bsh=1}^{10,000}\Delta d'(bsh) \leq 0\right) * 2$$

Where $\Delta d'(bsh)$ denotes d' difference between both versions (0° and 180° rotation) of mFD calculations for each bootstrap iteration.

2.2.1.10 Estimating overall ipsilateral, contralateral and binocular dLGN neuron fractions

The distribution of binarized rFD values was obtained for each dLGN slice, using a 40 µm spaced sampling grid. In order to compensate for uneven sampling across the anterior-posterior axis of the dLGN, instead of computing the mean across all sampling positions from all slices a weighted average was used. For this, sampling positions from slices that were located in underrepresented regions along the anterior-posterior axis had higher weights:

$$sFD_{\text{hist}}(S, FDb) = \frac{SP}{N}$$

$$apFD_{\text{hist}}(sb, FDb) = \frac{1}{n}\sum_{S=1}^{n} sFD_{\text{hist}}(S, FDb)$$

Where SP denotes the number of sampling positions from a slice (S) and N the total number of slices in a given anterior-posterior position bin along the dLGN (sb; based on 6 bins from 7.01 mm to 8.21 mm in the ACCF). FDb denotes the rFD bin (3 bins from -1 to 1). An additional weighting factor was used to compensate for differences in the cross-sectional area along dLGN:

$$W_{sa}(sb) = \frac{\overline{A_{sb}}}{\sum_{sb=1}^{n} \overline{A_{sb}}}$$

Where, $\overline{A_{sb}}$ is the mean cross-sectional area for each anterior-posterior position bin along the dLGN. The overall expected FD distribution across the whole dLGN was then calculated as:

$$rFD_{exp}(FDb) = \frac{1}{n}\sum_{sb=1}^{n} (apFD_{hist}(sb, FDb)W_{sa}(sb))$$

This gave an expected number of ipsilateral dominated cells (rFD < -0.33), contralateral dominated cells (rFD > 0.33) and binocular cells (-0.33 ≥ rFD ≤ 0.33), assuming perfect RGC axonal segregation and unselective input pooling (assuming radial symmetric dendrites).

This process was also performed on the non-binarized FD stacks using 6 rFD bins, and compared to the observed number of neurons in each rFD bin to give a correction factor for each rFD bin:

$$CF(FDb) = \frac{rFD_{exp}(FDb)}{rFD_{obs}(FDb)}$$

This correction factor could then be applied to each of the rFD bins before summing the total number of neurons in each categorical input type (based on ODI):

$$ipsiODI_{\text{total}} = \sum_{FDb=1}^{6} ipsiODI(FDb) \cdot CF(FDb)$$

$$binoODI_{\text{total}} = \sum_{FDb=1}^{6} binoODI(FDb) \cdot CF(FDb)$$

$$contraODI_{\text{total}} = \sum_{FDb=1}^{6} contraODI(FDb) \cdot CF(FDb)$$

$$ipsiODI_{\%} = 100 * \frac{ipsiODI_{total}}{ipsiODI_{total} + binoODI_{total} + contraODI_{total}}$$

$$binoODI_{\%} = 100 * \frac{binoODI_{total}}{ipsiODI_{total} + binoODI_{total} + contraODI_{total}}$$

$$contraODI_{\%} = 100 * \frac{contraODI_{total}}{ipsiODI_{total} + binoODI_{total} + contraODI_{total}}$$

2.2.1.11 Quality control, data exclusion criteria and statistics

Independent evaluation was done on electrophysiological data, confocal imaging, transduction coverage, dendritic tracing and confocal to ACCF alignment. After this quality control procedure 38 neurons were excluded from analysis of AMPAR response and 67 from NMDAR response analysis. A further 14 neurons were excluded when comparing AMPAR and NMDAR responses due to a rise in series resistance between the of >50% two protocols. The dendritic morphologies of 34 neurons were excluded due to poor tracing quality. One neuron had characteristic inhibitory morphology and was excluded from all analysis. 25 neurons were excluded due to poor confocal

imaging quality and ACCF alignment. 17 neurons were excluded from all analysis due to insufficient local RGC transduction. 20 neurons were excluded from mFD calculations due to a >30% of their dendrites protruding out of the confocal image stack, suggesting bad alignment and scaling. The resulting number of neurons included in each analysis are stated in the figure legends. Data are reported as mean +/- standard error of the mean (SEM) unless stated otherwise. In the cases where normality could not be ruled out (using Kolmogorov-Smirnov test) parametric tests were used. If normality could be ruled out Wilcoxon rank-sum, Mann-Whitney U, or Kruskal-Wallis tests were applied. For Circular statistics, the Matlab toolboxes `circ_stats` (Berens, 2009) and cirStatNP (https://github.com/dervinism/circStatNP) were used. Significance threshold crossings are indicated with asterisks: $p < 0.05$ (*), $p < 0.01$ (**), $p < 0.001$ (***).

2.2.1.12 Code and data availability

Code and data were made available at https://gin.g-node.org/Joel-Bauer/dLGN_binocularity and https://github.com/Joel-Bauer/dLGN_binocularity.

2.2.2 Experience-dependent representational drift in mouse V1

All animal experiments were conducted in accordance with the Max Planck Society guidelines as well as those of the local government (Regierung von Oberbayern).

2.2.2.1 Cranial window implant, intrinsic optical signal imaging targeted virus injections

In order to repeatedly measure visual tuning properties of neurons in mouse V1, neurons were virally transduced with the calcium indicator GCaMP6s, and a cranial window implanted over the visual cortex. To this end female C57BL/6 mice between P35 and P45 were anaesthetized using a mixture of Fentanyl (0.05 mg/kg), Midazolam (5 mg/kg) and Medetomidine (0.5 mg/kg), injected intraperitonially. Anaesthesia was maintained by injecting 25% of the original dose after the first 2 hours and then every hour. All surgical equipment was heat sterilized using a bead sterilizer and rinsed with ethanol. After checking for anaesthesia depth using the toe pinch reflex, the mice were placed on a thermostatically controlled heat-blanket (set to 37 °C) and the head fixed in a stereotaxic frame. 0.5 mg/kg of Carprofen was administered subcutaneously as an analgesic. Throughout the procedure the eyes were kept moist and protected from debris using eye-cream (Isopto-Max). The scalp was disinfected using iodine and ethanol, and lidocaine was applied as a local anaesthetic. The scalp was then removed along with the periosteum and the hair along the rim of the wound was fixed using Histoacryl. The skull was then roughened using a scalpel and a custom aluminium head bar was fixed onto the skull using superglue (Pattex Ultra Gel). Dental cement (Paladur) was used to further secure the head-bar to the skull, cover the edges of the scalp wound and cover the exposed skull (except for where the craniotomy would be placed). A rim of cement was built up around the front of the craniotomy in order to form a well. Diluted ultrasonic gel (diluted with cortex buffer in a ratio of 3:1) was placed in this well and a 10 mm cover glass placed over it, making sure to prevent bubbles. This increases the optical transparency of the skull for subsequent intrinsic optical signal (IOS) imaging.

The mice were then moved to an IOS imaging setup. An image of the blood vessel pattern over the visual cortex was taken with 530 nm illumination light (using a tandem 135 mm f/2.0 and 50 mm f/1.2 objective system, pco.edge 4.2 LT CCD camera or a Thorlabs B-Scope equipped with a 4x objective and a 1500 MonoChrome Camera). The skull was then illuminated with 735 nm light and the focal plan lowered to ~400 nm below the surface of the brain. A 700-740 nm bandpass filter was placed in front of the camera sensor. The contralateral eye was covered with a cone made of tape and drifting gratings were presented 7-14 times on a screen 16 cm in front of the mouse (8 directions at 2 cycles/s and 0.04 cycles/° changing direction every 0.6 s, presented for 7 s each time, with a horizontal retinotopic position 0 to -30°). The resulting intrinsic signal changes were analysed using custom written Matlab code. This allowed the visualization of the binocular region of V1, to aid targeting of virus injections in the next phase of the surgery.

The mice were then returned to the stereotaxic frame and a 4 mm craniotomy was performed using a high-speed micro drill with the intended virus injection and two-photon imaging locations at the centre. The skull was kept hydrated using cortex buffer during drilling. A 4 mm bone patch was removed, and the exposed cortex (still covered by dura) was washed repeatedly with cortex buffer until any bleeding stopped. The brain was covered with gelfoam pieces soaked in cortex buffer to keep it moist and protected from debris.

Before the surgery, borosilicate glass injection pipettes were pulled (using a Sutter PC-97 pipette puller). Volumetric markings were drawn onto the borosilicate capillaries before pulling (marks were drawn every 1 mm using black permanent marker, corresponding to 45 nl). The pipette tips were broken off so that the tip diameter was between 25-35 µm and bevelled to a sharp point using a modified computer hard disk (Canfield, 2006). The pipettes were then front loaded with the virus by placing a drop of virus on parafilm, lowering the pipette tip into the virus drop and applying negative pressure. The pipettes were either loaded with a mixture of AAV2/1.1CamKII0.4.Cre.SV40 (titer 1-5 E8), AAV2/1.Syn.Flex.mRuby2.GSG.P2A.GCaMP6s.WPRE.SV40 (titer 1.28 E13) and AAV2/1.Syn.-GCaMP6s.WPRE.SV40 (titer 6 E12), or AAV2/1.Syn.mRuby2.GSG.P2A.GCaMP6s.WPRE.SV40 (titer 1.2 E13). The loaded pipette tips were then kept on ice until use.

The preloaded glass injection pipettes were placed into a patch pipette holder and inserted 300-400 µm into the cortex using a micromanipulator. After waiting 4-5 min, the virus was injected into the brain at ~50 nl/min with a total volume of between 150-250 nl. This was done using 30-40 psi with 20-40 msec pressure pulses at 0.8 Hz controlled by a pulse generator (Master-8) and a pressure micro-injection system (Toohey Company). The pipette was then left in the brain for another 4-5 min before retracting it. The process was repeated for 2-5 injection sites, with a spacing of 50-100 µm. Throughout the injection procedure the brain was kept moist using cortex buffer. After all injections were completed the brain was covered with a 4 mm cranial window (glass cover slip), secured in place using super glue (Pattex Ultra Gel) around the rim of the craniotomy. After allowing the glue to dry, dental cement was used to cover any remaining bone and further secure the glass cover slip.

The mice were then administered 0.5-1 ml Sterofundin subcutaneously and the anaesthesia was ended using Naloxone (1.2 mg/kg), Flumazenil (0.5 mg/kg) and Atipamezole (2.5 mg/kg) also administered subcutaneously. The animals were kept in a warm environment and observed for several hours before returning to their home cage. Wet food was placed into the cages and 0.5 mg/kg of Carprofen was administered for the first 3 days after surgery. Fluorophores were allowed to express for 2-3 weeks before checking expression levels during *in vivo* imaging. If excessive bone-regrowth prevented imaging, a second short surgery was performed to replace the cranial window and remove any bone patches.

After surgeries the mice were placed in a 14/10 h light dark-cycle reversed room, so that the animals could be imaged during their dark cycle. Mice were co-housed with conspecifics (littermates whenever possible) in a large 1500 cm^2 cage containing nesting material, dark retreats and a running wheel. These conditions were upheld during stripe rearing.

2.2.2.2 Intrinsic optical signal imaging and Cylinder lens goggle mounting

2-4 weeks after the virus injection, IOS imaging was repeated (as described above) but without the use of ultrasound gel and using a drifting and inverting checkerboard bar (Fourier stimulus) to map out the retinotopic gradient across V1 (Kalatsky and Stryker, 2003). This stimulus allowed for better outlining of the V1 border. In these experiments, mice were anaesthetised only lightly, with Fentanyl (0.035 mg/kg), Midazolam (3.5 mg/kg) and Medetomidine (0.35 mg/kg), injected intraperitonially. Anaesthesia was maintained by injecting 25% of the original dose every hour. For animals that would later undergo stripe rearing, after IOS imaging the custom aluminium goggle frames (without cylinder lenses) were fitted to the animal's head and adjusted using tongs. The space between the frames and the eyes was such that the animal could still clean their eyes with their forepaws. The goggle frames were then attached to the head bars with small screws.

2.2.2.3 Chronic *in vivo* two-photon calcium imaging in awake mice

Prior to awake head-fixation, mice were handled for 5 days to accustom them to the experimenter, walking on a Styrofoam ball and brief head restraint. For imaging, mice were head-fixed on an air-suspended Styrofoam ball, allowing them to run, under a two-photon imaging system (Thorlabs Bergamo II). The two-photon system was equipped with a pulsed femtosecond Ti:Sapphire laser (Spectra Physics MaiTai DeepSee laser; tuned to 940 nm for calcium imaging or 1050 nm for structural imaging), resonant and galvo scanning mirrors, a 16x NA 0.8 immersion objective (Olympus) as well as a piezoelectric stepper for multiplane imaging. The photon collection pathway had a 720/25 nm short-pass filter followed by a dichroic beam-splitter (FF560) that allowed simultaneous detection of green and red light using two GaAsP photomultiplier tubes (PMTs; Hamamatsu) with either a 500-550 nm or a 572-642 nm bandpass filter. The system was controlled by ScanImage 4.2 (Pologruto et al., 2003). Ultrasound gel (diluted 3:1 with water and centrifuged to remove air bubbles) was placed over the cranial window implant and the 16x objective immersed in the gel. Strips of tape were used to shield the imaging window from external light.

Mice were presented with visual stimuli on a gamma-corrected LCD monitor (60Hz, 2560 x 1440 pixels, 27 inch) 16 cm from the eyes. The screen was either placed directly in front of the mouse if imaging binocular V1 or offset when imaging monocular V1, and the screen tilt was aligned to the angle of the mouse's head. The same screen position was used for repeated sessions of each mouse. Visual stimuli were generated in Matlab using the Psychophysics Toolbox (http://psychtoolbox.org). The visual stimulus consisted of a 25° radius grating (+12° fading-edge) drifting in 12 directions (0.04 cycles/° and 3 cycles/s) on a grey background with a stimulus duration of 5 s and an interstimulus interval of 6 s (grey screen). The mice were presented with these stimuli on 2 separate days before data acquisition began as part of habituation. During these days appropriate fields of view were identified and imaged during stimulus presentation allowing for re-finding on subsequent days. On data acquisition days, the stimuli were presented 32 times.

2.2.2.4 Stripe rearing

Mice that underwent stripe rearing were habituated to the goggle frames for a minimum of 4 days before the baseline imaging sessions. The goggle frames were removed when presenting visual stimuli and recording neuronal calcium signals, and were again fixed to the animal's head bar after the end of the imaging session. When imaging was followed by stripe rearing, the cylinder lenses were pressed into the goggles (sometimes secured with super glue) before attaching them to the animal's head bar again. Mice were subsequently returned to their home cage (which had stripes of black tape oriented along the permitted orientation of the cylinder lenses). Alternatively, mice were housed in a new cage with monitors around two sides of the cage that presented slowly drifting full field gratings moving in 8 directions during the light cycle.

2.2.2.5 Processing of *in vivo* two-photon calcium imaging data and calculation of preferred orientations

Fluorescence traces from *in vivo* data were extracted either using custom Matlab software or Suite2P (Pachitariu et al., 2017). Both methods produced average fluorescence images, single neuron region of interst (ROI) average fluorescence over time, with ROIs independently calculated or drawn for each day. The ROIs were matched manually across days using custom written Matlab code (Multiple ROI Predator, generously provided by Pieter Goltstein). Only neurons that could be reidentified on every imaging session were included in further analysis. The calcium activity of a neuron was defined to be ΔF/F and was calculated as:

$$\Delta \mathrm{F}/F = \frac{\left(F(t) - 0.7 * \left(F_{\mathrm{neuropil}}(t) - \tilde{F}_{\mathrm{neuropil}}\right)\right) - \tilde{F}_{\mathrm{baseline}}}{\tilde{F}_{\mathrm{baseline}}}$$

Where F(t) is the green fluorescence trace of a neuron, $F_{neuropil}(t)$ is the neuropil green fluorescence trace, $\tilde{F}_{neuropil}$ is the median of the neuropil fluorescence trace and $\tilde{F}_{baseline}$ is the median of all 1 s pre-stimulus periods of the ROI fluorescence (Chen et al., 2013).

The stimulus tuning curve of a neuron was defined as the mean ΔF/F during the stimulus presentation across all trials for a given grating direction (resulting in a vector length 12). To calculate the pairwise signal correlation (PSC) matrix, the Pearson's correlation between the stimulus tuning curves of all pairs of neurons were calculated (resulting in a square matrix size neurons x neurons). The pairwise stimulus correlation matrix of each day was vectorized and correlated with the vectorized PSC matrix of every other day (resulting in a square matrix size days x days).

For further analysis, the preferred orientation (PO) was calculated as follows. First, neurons were tested for visual responsiveness. For each stimulus, a rank sum test between the stimulus period mean ΔF/F and the pre-stimulus period mean ΔF/F was applied (with Bonferroni correction significance threshold of $p < 0.05$). If a neuron's ΔF/F was significantly above the ΔF/F during the pre-stimulus period for any stimulus it was considered visually responsive. Second, the PO of each neuron was calculated using the vector sum across all responses:

$$X = \frac{1}{n_{rep} * n_{\text{stim}}} \sum_{\text{rep}=1}^{n_{\text{rep}}} \sum_{\text{stim}=1}^{n_{\text{stim}}} R_{(\text{stim,rep})} \cos\left(2\theta_{(\text{stim,rep})}\right)$$

$$X = \frac{1}{n_{rep} * n_{\text{stim}}} \sum_{\text{rep}=1}^{n_{\text{rep}}} \sum_{\text{stim}=1}^{n_{\text{stim}}} R_{(\text{stim,rep})} \sin\left(2\theta_{(\text{stim,rep})}\right)$$

$$\theta_{PO} = \frac{1}{2} \arctan\left(\frac{Y}{X}\right)$$

Where $R_{(\text{stim,rep})}$ is the stimulus period mean ΔF/F per stimulus per trial, θ_{PO} are the corresponding visual stimulus angles, n_{stim} is the number of different stimulus angles and n_{rep} is the number of stimulus repetitions (usually 32). Bootstrap resampling across all stimulus repetitions is applied in order to obtain a distribution of θ_{PO}. PO is defined as the $\overline{\theta_{PO}}$ across all bootstrap samples. The 95% confidence interval (upper PO_{CI} and lower PO_{CI}) is also calculated from the distribution of θ_{PO}. If the difference between the upper PO_{CI} and lower PO_{CI} is greater than 45°, then the neuron was considered not orientation tuned. A neuron was considered concurrently tuned across a time interval, if it was both visually responsive and tuned on both days. For these neurons the ΔPO was calculated. In order to determine if the PO of a cell was significantly different on two separate days, the PO of the second day had to be outside the PO 95% confidence interval of the first day and the PO of the first day had to be outside the PO 95% confidence interval of the second day.

The permitted orientation during stripe rearing was calculated by taking a photo of the mouse, wearing the goggle frames, from the centre of the stimulus presentation screen. The angle of the goggles in the image was measured using ImageJ. This angle was adjusted based on the angle of the image presentation screen to give the permitted orientation relative to the mouse. To calculate drift direction, the change in a neuron's PO relative to the permitted orientation (i.e. if it moved towards or away from the permitted orientation, perm), was calculated as follows:

$$\text{for stability data: } \Delta|rPO| = |(\text{PO}_{t2} - \overline{\text{perm}}) - (PO_{t1} - \overline{\text{perm}})|$$

$$\text{for stripe rearing data: } \Delta|rPO| = |\ (PO_{\text{post}} - \text{perm}_{\text{mouse}}) - (PO_{\text{pre}} - \text{perm}_{\text{mouse}})\ |$$

Where $\overline{\text{perm}}$ is the mean permitted orientation of the cylinder lens goggles of all stripe reared mice and $perm_{mouse}$ is the permitted orientation for the mouse from which the neuron came.

3. Results

3.1 Limited eye-specific convergence in the dLGN and its causes

The data and figures in this section are adapted from Bauer et al., 2021.

3.1.1 Experimental pipeline

In order to quantify the ratio of eye-specific RGC inputs to individual TC neurons and investigate the morphological factors that influence eye-specific convergence, a data acquisition pipeline was developed (Figure 3.1a). Each eye of P40 mice was injected with AAVs to induce expression of one of two light sensitive ion channels tagged with a fluorophore (AAV2/2.Syn-Chronos.EGFP or AAV2/2.Syn-ChrimsonR.tdT) in RGCs. After 5-7 weeks expression time, acute coronal brain slices were prepared and cells within the dLGN were patch-clamped in whole-cell configuration. Red and blue light pulses were used to stimulate RGC axons that expressed Chronos (blue light sensitive) or ChrimsonR (red light sensitive). The resulting EPSCs were measured in dLGN neurons voltage-clamped at -70 mV. However, ChrimsonR can be excited both by blue as well as red light, meaning that for dLGN neurons that receive input from both RGC axon pools, blue-light pulse induced EPSCs are caused by a combination of inputs from both RGC axon pools. To circumvent this crosstalk between ChrimsonR and Chronos due to the overlapping excitation wavelength profiles, a blue- and then a red-light intensity ramp protocol was applied (Klapoetke et al., 2014; Hooks et al., 2015). First, the blue-light intensity was increased until maximum excitation was elicited. This blue-light pulse intensity was then maintained, while a longer red-light pulse was delivered preceding the blue-light pulse at increasing intensities, until the red-light induced EPSC no longer increased and the blue-light pulse induced EPSC no longer decreased. Crucially, the red-light pulse desensitises the ChrimsonR, so that it can no longer be activated by the blue-light pulse, allowing for accurate and cross-talk free quantification of the maximum inducible EPSC by eye-specific RGC axon stimulation (Hooks et al., 2015; Figure 3.1b). The red-light intensity ramp protocol was repeated at +40 mV voltage-clamp to allow for the measurement of both AMPAR induced EPSCs (at -70 mV) and NMDAR induced EPSCs (at +40 mV). Together, this stimulation protocol allowed for the characterization of dLGN neurons based on their eye-specific RGC input.

After patch-clamp recordings of dLGN neurons, multiple two-photon stacks were acquired to visualize the distribution of EGFP (green; linked to Chronos) and tdTomato (red; linked to ChrimsonR) labelled RGC axons around the recorded neurons and throughout the dLGN (Figure 3.1a). The position of the recorded cells within the Allen common coordinate framework (ACCF) was subsequently estimated based on the shape of the dLGN and its eye-specific projection zones (Figure 3.1c). The intracellular solution of the pipettes used for recording neurons contained Alexa-594, allowing their localization within these two-photon stacks and tracing of their dendrites. The dendritic structure also allowed the exclusion of interneurons from further analysis. The brain slices were then fixed and made transparent by tissue clearing (using RapiClear 1.47) before confocal image stacks were acquired. This was followed by scaling and alignment of the traced dendritic structures to the confocal image stacks, and allowed for characterization of the diversity of dendritic arbour shapes and the estimation of the relative proportion of ipsi- and contralateral RGC axons in proximity to the dendrites of recorded neurons (Figure 3.1d). Together, this data acquisition

and analysis pipeline allowed for the characterization of eye-specific RGC input convergence on single TC neurons and quantification of several morphological factors that may explain the amount of convergence on a single cell and population level.

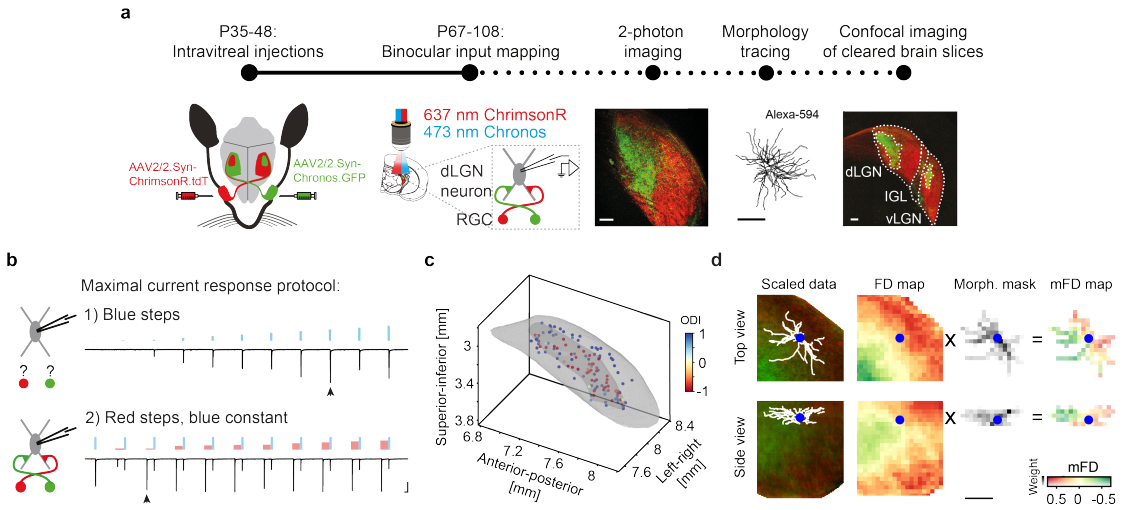

Figure 3.1: Experimental pipeline for investigating eye-specific RGC convergence in the mouse dLGN. a) Data acquisition overview. From left to right: Light sensitive ion channels ChrimsonR-tdTomato and Chronos-GFP are expressed in either retina through intravitreal injection of AAVs. RGC input to single dLGN TC neurons is evaluated using ex vivo whole-cell patch-clamp recordings while stimulating RGCs using red and blue light. Z-projection of two-photon image stack of RGC axon fluorescence in the dLGN. Dendritic tracing of Alexa-594 filled and recorded TC neuron from two-photon image stack. Z-projection of confocal image stack of RGC axon fluorescence after tissue clearing. Scale bars: 100 µm. b) Dual-colour optogenetic input mapping protocol. First, RGC axons are stimulated with blue light pulses of increasing intensity. Second, blue light pulse (at maximum blue light evoked response; arrow in top trace) is preceded by red pulses of increasing intensity. Red and blue light evoked responses (arrow in bottom trace) are used to calculate the ocular dominance index (ODI). Scale bars: 100 ms and 250 pA. c) ODI and estimated location of TC neurons within Allen common coordinate framework (ACCF) defined dLGN outline. d) Dendritic morphology and TC neuron location within confocal image stack (left). Combining the 3D binned fluorescence ratios stack (FD map) with the 3D binned relative dendrite density (morphology mask), gives an estimate of the relative proximity of RGC axons to the dendrites of recorded neurons quantified as the morphology-based FD (mFD) map. Scale bar: 100 µm. Adapted with permission from Bauer et al. (2021).

3.1.2 Limited overall eye-specific convergence on TC neurons in the dLGN

The dual-colour optogenetic input mapping protocol described in Figure 3.1 allowed for the characterization of TC neurons based on their categorical input type (Figure 3.2a). Most of the recorded TC neurons (64%) received input from both eyes, if both AMPAR and NMDAR based responses were considered (Figure 3.2b). This aligns with a previous retrograde rabies virus tracing result (Rompani et al., 2017). The optogenetic stimulation approach additionally allowed for the comparison of the relative input strength from both eyes. Here, the ocular dominance index (ODI) is the difference in EPSC amplitude evoked by stimulation of the contralateral RGC axons minus that of the ipsilateral RGC axons divided by the sum of the two. The distribution of this ODI value across all recorded neurons is shown in Figure 3.2c. Strikingly, although many neurons responded to stimulation of RGC axons from both eyes, there were only very few neurons that had ODI values between -0.333 and 0.333 (corresponding to the non-dominant eye providing at least 50% of the input strength compared to the dominant eye). Most of the neurons responded much more strongly to stimulation of either the ipsi- or the contralateral RGC axons. Overall, there was on average a 36-fold higher response to the dominant eye compared to the non-dominant eye (Figure 3.2d). This indicated that for the TC neurons that were recorded, the majority of their inputs originated from only one of the two eyes.

The focus of these experiments was to investigate convergence of eye-specific inputs to TC neurons. For this reason, more neurons were recorded within and around the ipsilateral projection

zone, likely skewing the distribution in favour of ipsilateral and binocular cells. In order to address this sampling bias, a correction was applied to the distribution using the discrepancy between the distribution of local fluorescence ratios, rFD, of the recorded neurons and the distribution of homogenously sampled locations across all recorded dLGN slices. After this sampling bias correction, the percentage of TC neurons in dLGN that had ODIs between -0.333 and 0.333, was just 0.9% (Figure 3.2e). Therefore, although many TC neurons receive some level of input from RGCs from both eyes, the number of TC neurons that receive similar amounts of input from both eyes is very small.

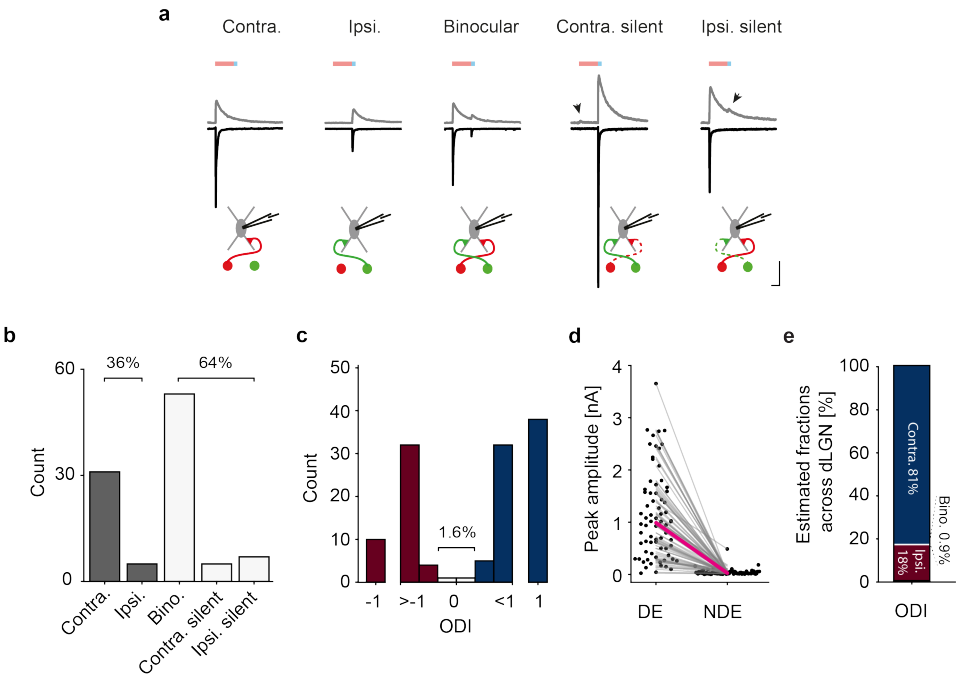

Figure 3.2: Overview of eye dominance and binocularity of RGC inputs to recorded TC neurons. a) Representative current traces from voltage-clamped neurons at -70 mV (black) and +40 mV (grey). Ipsi- and contralateral silent cells receive NMDAR mediated but not AMPAR mediated input from one eye. Arrows indicate input only detectable at +40 mV. Scale bars: 100 ms and 250 pA. b) Fraction of recorded TC neurons that had detectable input from one or both eyes. n = 101 neurons. c) Ocular dominance index distribution of all recorded TC neurons. Colour code same as in e. n = 123 neuronscontralateral eye (ODI > 0.333; blue), ipsilateral eye (ODI < -0.333; red) and comparable input from both eyes (ODI -0.333 $\geq$ and $\leq$ 0.333; white). d) Peak response amplitude of TC neurons evoked by stimulation of dominant and non-dominant RGC input at -70 mV holding potential. Only cells with detectable input from both eyes are included. n = 75 neurons. e) Estimated fraction of TC neurons with dominant input from the contralateral eye (ODI > 0.333; blue), ipsilateral eye (ODI < -0.333; red) and comparable input from both eyes (ODI -0.333 $\geq$ and $\leq$ 0.333; white) after sampling bias correction. ODI of -0.333 $\geq$ and $\leq$ 0.333 corresponds to a non-dominant to dominant input ratio of > 0.5. Adapted with permission from Bauer et al. (2021).

3.1.3 Distribution of TC neuron eye preference and monocularity across dLGN and visuotopy

Mouse dLGN is a complex retinotopic structure with multiple regions of functional specialisation. Importantly, the regions of functional specialisation cannot easily be identified in the single coronal plane in which the brain tissue was sliced for *in vitro* experiments. It was therefore necessary to re-identify the location of the recorded neurons in a 3D representation of dLGN, in order to analyse the organization of single cell eye-specific convergence on a population level. The positions of the recorded neurons were therefore estimated within the Allen common coordinate framework (ACCF), which distinguishes between three functional subregions of dLGN: the shell, the contralateral projection zone of the core and the ipsilateral projection zone of the core (Figure 3.3a,b). As expected, recorded neurons located in the ipsilateral projection region were more commonly dominated by ipsilateral input (40 ipsilateral dominated neurons, 20 contralateral dominated neurons), while those within the contralateral region were more commonly contralateral dominated (12 ipsilateral dominated neurons, 64 contralateral dominated neurons). The recorded neurons within the shell region were always contralateral dominated. However, the ipsi- and contralateral projection zones of the core did contain a substantial number of neurons dominated by the opposite eye, indicating that the functional segregation of eye-dominance did not strictly adhere to the RGC axon projection region (Figure 3.3b). Interestingly, neurons that received input from both eyes were more binocular (lower |ODI|) if their eye dominance was opposite to the projection zone in which their soma was located (Mann-Whitney U-test: $p < 0.001$, $U = 694$, $n = 82$).

In order to describe the distribution of eye-dominance and the degree of single cell eye-specific convergence across visual space (visuotopy), an existing dataset of *in vivo* recorded visuotopy (Piscopo et al., 2013) was registered to the ACCF (Figure 3.3c). Based on the location of a recorded TC neuron within the ACCF, a corresponding visuotopic position could be assigned. Figure 3.3d shows the average eye preference of recorded neurons within 10° bins of visual space, as well as their monocularity (absolute ODI). As expected, TC neurons in locations representing the ventrolateral visual space were more commonly contralaterally dominated, while those in the area representing the dorsomedial visual space, which is viewed by both eyes, could be dominated by input from either the ipsi- or the contralateral eye. However, no portion of the visual space had an average monocularity below 0.8, indicating that no portion of visual space is represented by TC neurons with comparable input from both eyes. Highly binocular TC neurons are therefore rare across all areas of dLGN.

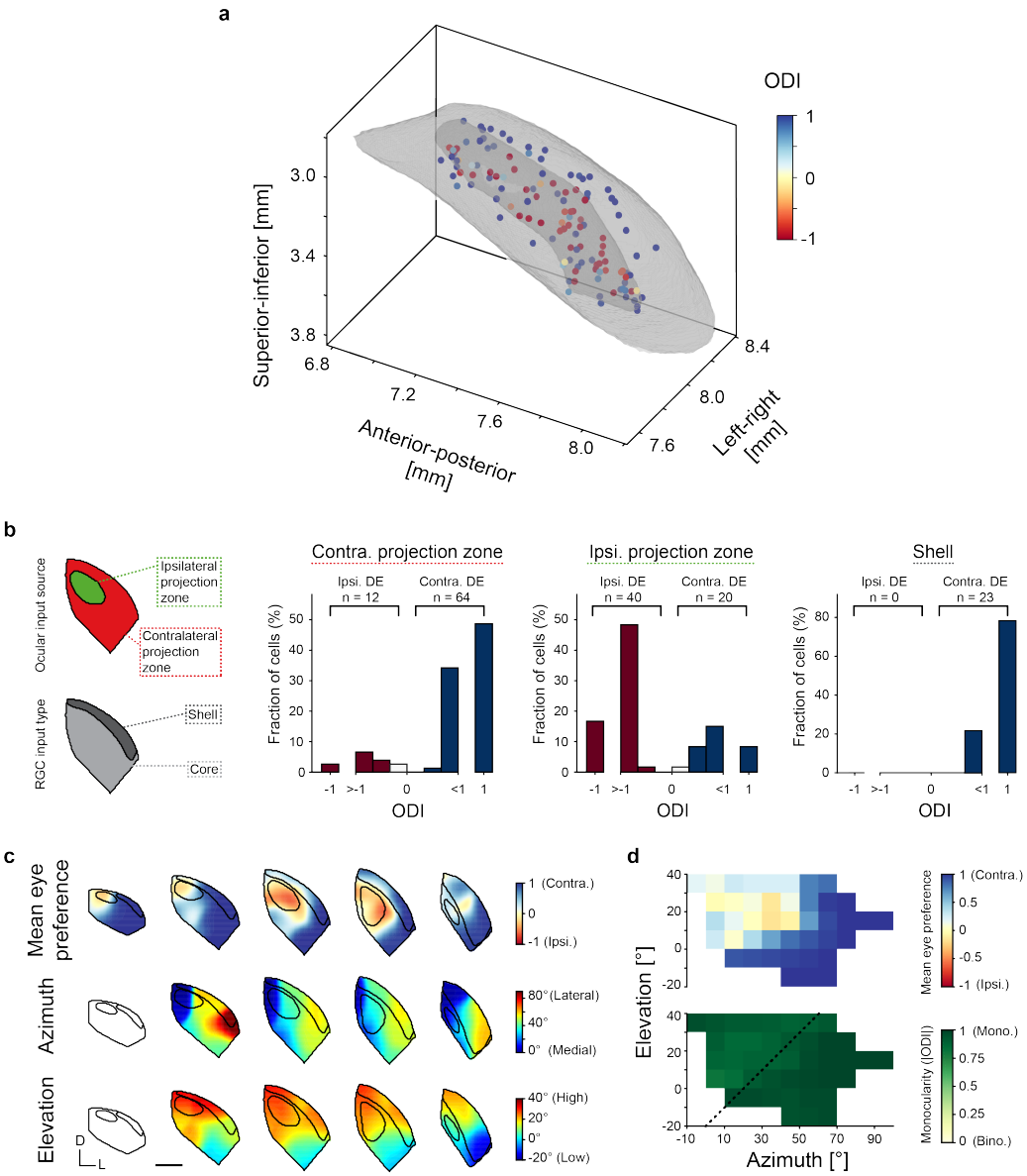

Figure 3.3: Eye-specific RGC input preference to TC neurons across dLGN and corresponding retinotopic organization. a) Estimated position and ODI of 139 TC neurons in the dLGN. ACCF dLGN border in grey. b) Ocular dominance index distributions of cells recorded from three anatomical subregions, as defined on the left. c) 3D interpolated and extrapolated map of mean eye preference, and visuotopic azimuth and elevation in five coronal sections through dLGN. Slices are arranged from anterior (left) to posterior (right). ACCF aligned azimuth and elevation maps based on data provided by the Niell Lab (Piscopo et al., 2013). d) Mean eye preference and monocularity (|ODI|) relative to position within dLGN map of retinotopy. Area left of dashed black line indicates visual space viewed by both eyes, as defined by Dräger, 1978. Adapted with permission from Bauer et al. (2021).

3.1.4 The dendritic morphology of TC neurons cannot be classified into distinguishable types

TC neuron dendritic organization could be described using a variety of different metrics. These included the maximum reach, the total length, the complexity of dendritic branching, and multiple metrics of overall shape (Figure 3.4a). Testing for multimodality (using Hartigan's Dip test) on each of these morphological features indicated that there were no separable distributions or clusters within the data (Figure 3.4a). I found that the shape of the dendritic arbours could best be described by two metrics that did not correlate with one another, asymmetry and elongation (Figure 3.4b-d). Asymmetry quantified the relative total length of dendrites on one side of the soma compared to the other, while elongation quantified the ratio of dendritic length in one axis compared to the orthogonal axis. When the asymmetry and elongation of all recorded TC neurons was plotted, TC neurons that resemble the previously described X, Y and W morphological types (Krahe et al., 2011; see Figure 3.4c cell 1, 2 and 3 respectively) were well separated, but there were no apparent clusters that indicated distinguishable morphological types (Figure 3.4c-d).

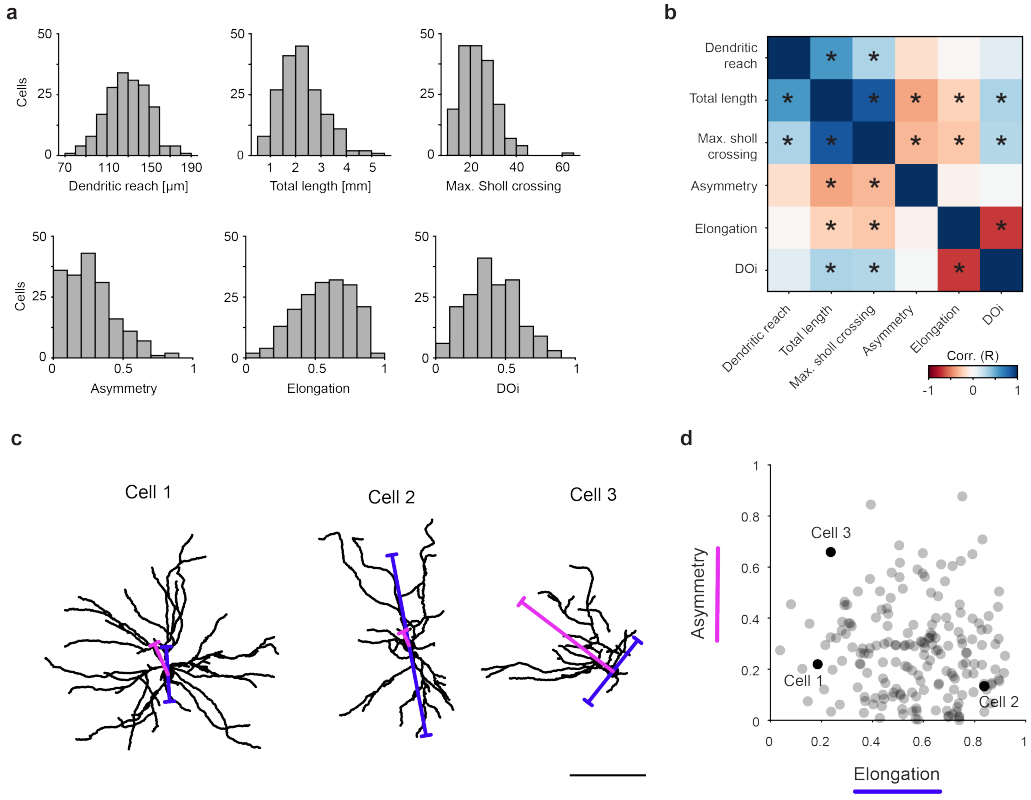

Figure 3.4: TC neuron arbour organization is highly variable, but there are no distinguishable morphological types. a) Histograms of the distributions of six dendritic morphology metrics from 185 TC neurons. b) Correlation matrix for the six metrics in a. Spearman's correlation, $p < 0.05$ indicated with *. c) Dendritic morphologies of three example cells. Magnitude and direction of asymmetry (magenta) and elongation (blue) are superimposed as lines originating from the soma. Scale bar: 100 µm. d) Scatter plot of asymmetry and elongation. Example cells in c are indicated in black. Adapted with permission from Bauer et al. (2021).

3.1.5 Segregation of eye-specific RGC axons cannot account for their low level of convergence on TC neurons

Segregation of eye-specific RGC axons in the mouse dLGN could, in principle, lead to fewer binocular neurons (Figure 3.5a). However, this depends on the reach of TC neuron dendrites. The radial distribution of the recorded and traced neurons was therefore quantified and used to construct a 3D radial mask (Figure 3.5b). In order to simulate perfect eye-specific RGC axon segregation and remove the influence of noise in the confocal image stacks, the dLGN FD stacks were binarized. By homogenously sampling across the binarized dLGN FD stacks with the 3D radial mask, a distribution of rFD values was obtained (Figure 3.5c-e). When this process was repeated for all dLGN slices with sufficiently homogenous RGC axon labelling, 10% of sampling positions had rFD values between -0.333 and 0.333, compared to 12% of positions who's rFD values were under -0.333 (Figure 3.5f). Therefore, the number of positions within the dLGN slices that had similar access to RGC axons from both eyes was roughly equal to the number of positions that had at least twice the access to RGCs of the ipsilateral eye. This is in stark contrast to the estimated 0.9% of neurons across these slices that had an ODI of between -0.333 and 0.333. The segregation of eye-specific RGC axons in combination with the average reach of TC neuron dendrites is therefore not sufficient to explain the low level of binocularity of TC neurons, assuming radial symmetry of dendrites.

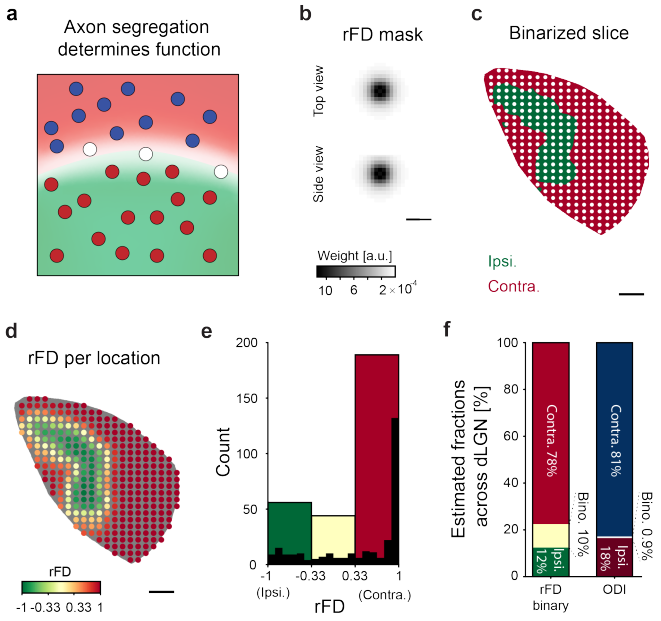

Figure 3.5: Segregation of ipsi- and contralateral RGC axons does not explain the small fraction of binocular TC neurons. a) Schematic illustration representing the putative effect of RGC axon segregation on TC neuron eye dominance. Contralateral neurons in blue, ipsilateral neurons in red, binocular neurons in white. b) Average circular distribution of 3D TC dendrite density. c) Binarized RGC axon fluorescence ratio across representative dLGN coronal section. White points indicate sampling positions. d) rFD values from binary fluorescence at each sampling position in c. e) Histograms of rFD from binary fluorescence of all sampling points in c-d. Histogram based on 30 rFD bins in black. Histogram based on 3 rFD bins in colour (rFD $>$ 0.333 in red; rFD $<$ -0.333 in green; rFD -0.333 $\geq$ and $\leq$ 0.333 in yellow). f) Estimated fraction of TC neurons with rFD from binary fluorescence based on red, green and yellow bins in e. Estimated fraction of TC neurons with dominant input from the contralateral eye (ODI $>$ 0.333; blue), ipsilateral eye (ODI $<$ -0.333; red) and comparable input from both eyes (ODI -0.333 $\geq$ and $\leq$ 0.333; white) after sampling bias correction. All scale bar: 100 µm. Adapted with permission from Bauer et al. (2021).

3.1.6 TC neuron dendritic bias does not prevent eye-specific RGC input convergence

Due to the inhomogeneous distribution of eye-specific RGC axons in dLGN, the diverse organization of TC neuron dendrites could, in principle, alter the relative availability of inputs to TC neurons. Particularly the elongation or asymmetry of dendrites with respect to the soma could mean that a TC neuron has access to different RGCs depending on the direction of dendritic elongation and asymmetry (Figure 3.6a). This is exemplified by the fact that rotating the dendritic arbours of some TC neurons alters the availability of ipsi- and contralateral RGC axons, quantified as a change in mFD (Figure 3.6b). Consequently, on a single cell level the orientation of a neuron's dendritic arbour affects its functional eye preference. This is demonstrated by the fact that the mFD distribution of ipsi- and contralateral dominated cells becomes less discriminable when their dendritic arbours are rotated by 180° (Figure 3.6c). On the other hand, if on a population level the dendritic arbours of TC neurons are organized in such a way that they enhance or reduce overall functional binocularity, then rotating all neurons should either increase or decrease the average mFD. However, there is no circular-linear correlation between the rotation of dendritic arbours and the average mFD (Figure 3.6d-e). This demonstrates that although the position of the dendrites affects the eye preference of an individual neuron, the organization of dendrites across all TC neurons does not predispose the population to either increase or decrease the overall level of binocularity.

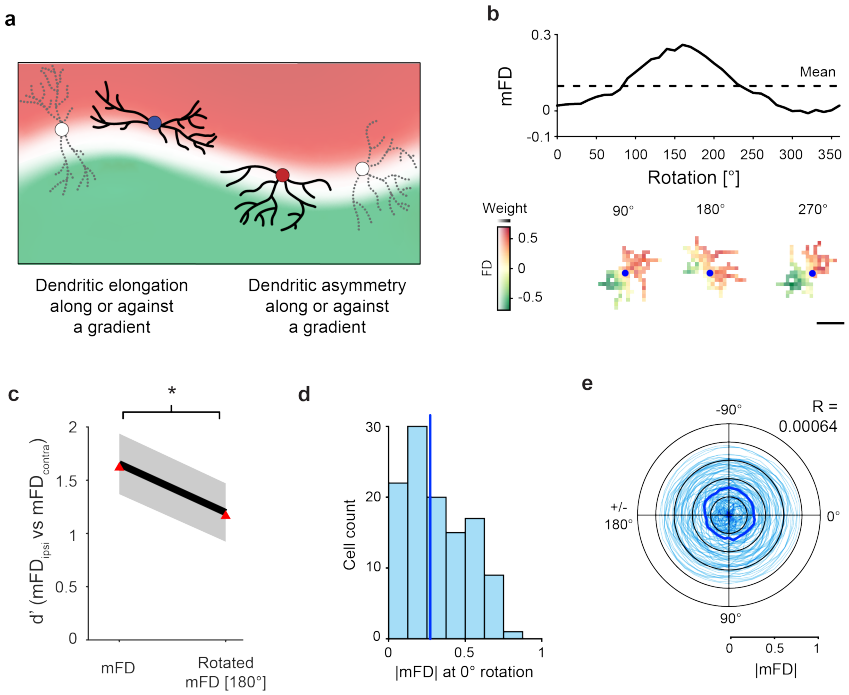

Figure 3.6: Rotating TC dendritic arbours affects availability of RGC axons on a single cell level but not on a population level. a) Schematic illustration representing the effect of elongated or asymmetrical dendritic arbours on the sampling of local RGC axons. b) Masked local fluorescence of example TC neuron when the dendritic arbour is rotated through 360°. Scale bar: 100 µm. c) d' of mFD distributions of ipsi- and contralateral dominant TC neurons at original dendritic arbour orientation and after rotating by 180° (red). Black line and grey area indicate mean and 95% confidence interval of d' from bootstrap resampled data. (n = 82 neurons; two-tailed paired bootstrapped p-value of d' of ipsi- and contralateral dominant TC neuron mFDs at 0° vs 180° rotation of dendritic arbour: p = 0.0142). d) Histogram of TC neuron |mFD| at original orientation of dendrites. Blue line indicates median. e) |mFD| of single cells (light blue) and median (dark blue) when dendritic arbours are rotated through 360°. Circular-linear correlation (n = 114 neurons, circular-linear Spearman's correlation R = 0.00064, p = 0.28). Adapted with permission from Bauer et al. (2021).

3.1.7 TC neuron eye preference is probabilistically determined by relative availability of RGC axons

Eye-specific RGC axons segregation and TC neuron dendritic organization cannot fully explain the low level of binocular integration. This means that the relative availability of ipsi- and contralateral RGC inputs to TC neurons cannot explain the low level of binocular integration observed in the data. This suggests that even if a TC neuron has access to RGC axons from both eyes, it selectively forms stronger and/or more numerous connections with axons from only one eye (Figure 3.7a). This is exemplified by the fact that neighbouring TC neurons recorded from the same acute brain slice, with overlapping dendritic arbours and similar mFD values can have opposite eye preferences (Figure 3.7b). Although on the population level mFD does predict eye preference (Figure 3.6c), TC neurons tend to be monocular across the range of mFD values measured (Figure 3.7c). Therefore, mFD only predicts eye preference in a probabilistic manner (Figure 3.7d).

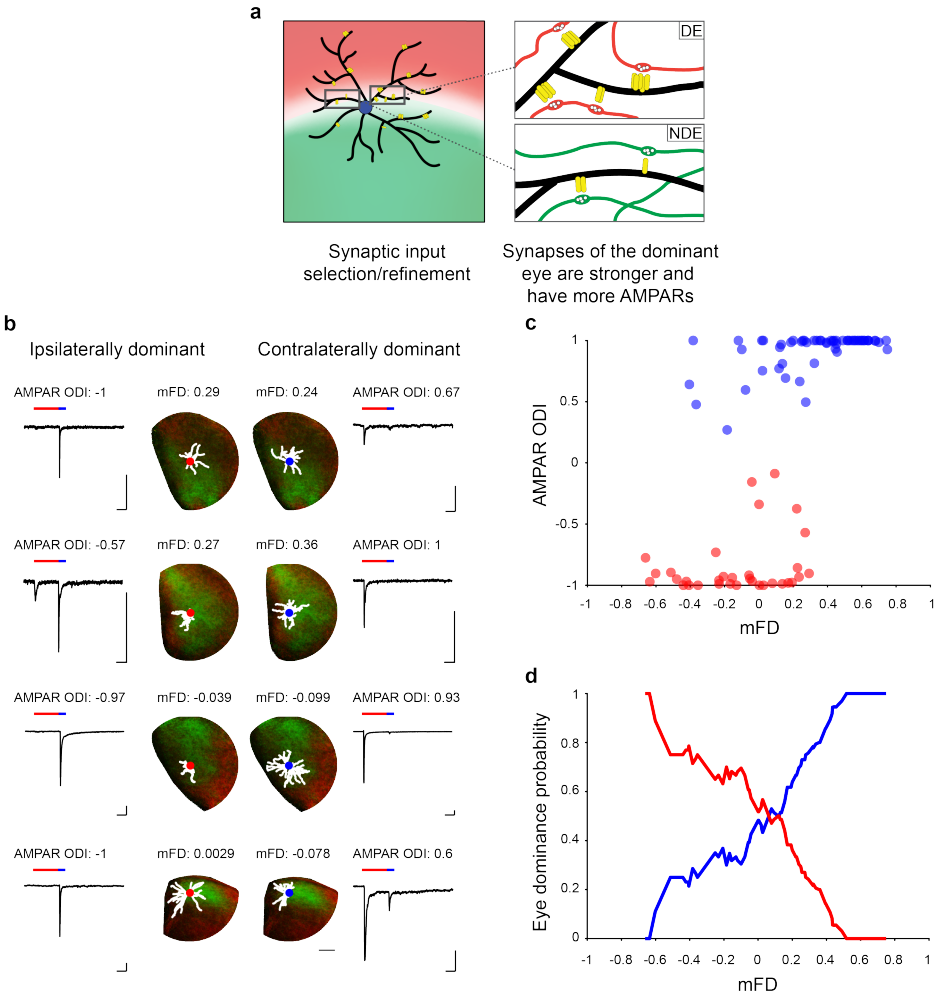

Figure 3.7: Input selection results in functional monocularity of TC neurons. a) Schematic illustration of TC neurons preferentially forming synapses with RGC axons from one eye, when both are available. b) Four examples of neighbouring neurons with similar RGC axon availability (mFD) but opposite eye dominance. AMPAR current traces (holding potential -70mV) in response to optogenetic stimulation of RGC axons. c) Scatter plot of mFD and AMPAR based ODI. Ipsilateral dominant TC neurons in red, contralateral dominant TC neurons in blue. d) Probability of ipsi- (red) or contralateral (blue) eye dominance as a function of mFD. Adapted with permission from Bauer et al. (2021).

3.1.8 Non-dominant eye inputs have lower AMPAR to NMDAR mediated response ratios

The non-dominant eye input strength of binocular TC neurons is not only much weaker than that of the dominant eye (Figure 3.2d), but its AMPAR to NMDAR ratio is also 4X lower (AMPAR and NMDAR mediated responses measured at -70 mV and +40 mV holding potential, respectively; Figure 3.8a). Non-dominant eye synapses therefore differ in their receptor composition to those of the dominant eye. However, across all eye-specific inputs, AMPAR to NMDAR ratio scales non-linearly with AMPAR based input strength (Figure 3.8b), suggesting that weaker inputs may in general have lower AMPAR to NMDAR ratios. In either case, this may explain the somewhat lower monocularity of TC neurons when ODI is calculated based on NMDAR mediated responses instead of AMPAR mediated responses (Figure 3.8c).

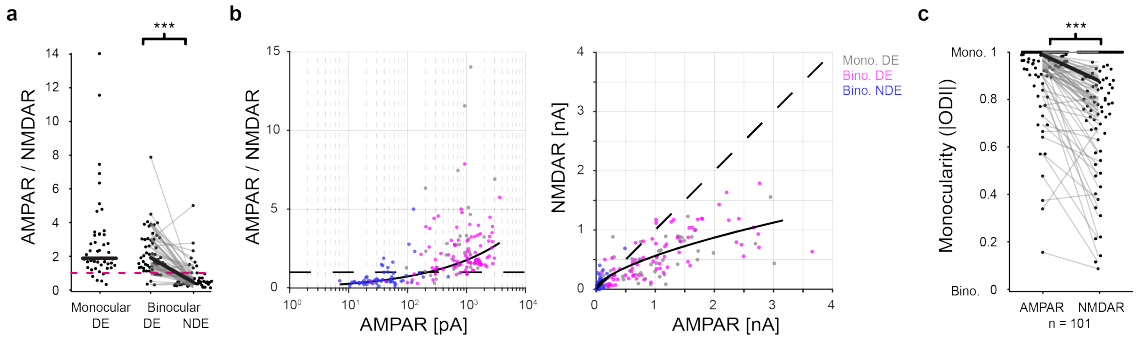

Figure 3.8: AMPAR to NMDAR mediated response ratios of eye-specific RGC inputs. a) AMPAR to NMDAR mediated response ratio for the dominant eye of monocular and binocular TC neurons are not statistically different (Mann-Whitney U test, p = 0.43, n = 48 monocular cells and 53 binocular cells). AMPAR to NMDAR mediated response ratios to stimulation of non-dominant eye inputs of binocular neurons are lower than those for the dominant eye (Wilcoxon signed rank test, $p < 0.001$, n = 53 cells). Dashed magenta line indicates AMPAR/NMDAR ratio of 1. b) AMPAR and NMDAR mediated response strength (right) and AMPAR/NMDAR ratios (left) across all input types. NMDAR mediated input strength increases sub-linearly relative to AMPAR mediated input strength (fit as black line: $NMDAR = 7.32 + 6.99 * AMPAR^{0.63}$). Dominant eye inputs of monocular neurons in grey, dominant eye inputs of binocular neurons in magenta and non-dominant eye inputs in blue. Dashed black line indicates AMPAR/NMDAR ratio of 1. c) Monocularity (|ODI|) of neurons based on AMPAR and NMDAR mediated responses, measured at -70 mV and +40 mV holding potential, respectively. NMDAR is lower than AMPAR based monocularity (Wilcoxon signed rank test, $p < 0.001$, n = 101 cells). Adapted with permission from Bauer et al. (2021).

3.2 Experience dependent drift of orientation tuning in mouse V1

3.2.1 Pairwise signal correlation decay of tuning curves

In order to investigate representational drift, P32 mice were injected with AAVs containing genes for GCaMP6s (a green fluorescent calcium indicator) and mRuby2 (a red fluorescent structural marker) into the V1. This allowed for chronically recording the visually evoked calcium responses of neurons over many weeks (Figure 3.9a). By presenting drifting gratings moving in 12 directions to the mice while performing head-fixed two-photon imaging, tuning curves of the same neurons were repeatedly measured (Figure 3.9b). First, a previous demonstration of representational drift (Montijn et al., 2016) was confirmed by calculating the pairwise signal correlation (PSC) for each imaging time-point and calculating the correlation between all pairs of PSC matrices. As in Montijn et al. (2016), this PSC correlation decreased with longer time intervals (Figure 3.9c).

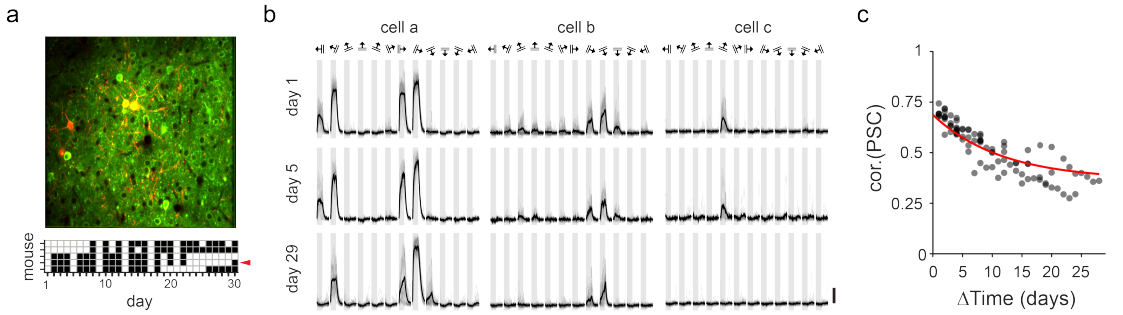

Figure 3.9: Pairwise signal correlation decay of mouse V1 neurons revealed through chronic two-photon calcium imaging. a) Top: Example field of view from one animal. Average GCaMP6s and mRuby2 fluorescence in green and red, respectively. Bottom: imaging timeline of 5 mice. White squares indicate days on which a mouse was imaged. Timeline of example animal in b and c indicated by red arrowhead in a. b) Example stimulus evoked GCaMP6s responses for three cells on three days from the same animal. Grey lines: Responses to individual stimulus repetitions, black lines: average across all repetitions. Grey bars indicate 5 s stimulus window with grating direction indicated above. Scale bar 200 $\Delta F/F$. c) Time dependent correlation decrease of pairwise signal correlation (PSC) for one animal. The correlation between pairwise signal correlation matrices (correlation of the average tuning curves between all pairs of neurons) from different imaging session are plotted in black. Red line indicates exponential decay fit (half-life of 11.5 days).

3.2.2 Drift of preferred orientation of V1 neurons

The direction tuning curves of V1 neurons typically remained similar over the course of 1 month, although neurons that increased or decreased their overall response amplitude, and even gained or lost visual responsiveness completely (cell c in Figure 3.9b), were common. This change in responsiveness of neurons undoubtedly contributes to the overall representational drift measurable through ensemble rate correlation (see Deitch et al., 2021) or PSC. However, when a neuron becomes unresponsive it is not possible to know whether the neuron has become less responsive to visual stimulation in general or simply became tuned to a visual stimulus feature outside the range that was presented in the stimulus set. My aim was to identify specific visual tuning features that undergo cumulative change over time. To this end, the preferred orientations (PO) on consecutive days for all neurons, which remained visually responsive and tuned, were plotted. These responsiveness and tuning criteria were used because in the absence of visual responsiveness or tuning a neuron does not have a reproducible PO. As expected, the PO was similar on consecutive days with a Pearson's correlation of 0.968 (Figure 3.10a). However, if the POs were compared across 20-day intervals, the POs of neurons were less similar, with a Pearson's correlation of 0.800 (Figure 3.10b). When comparing the absolute change in PO across different time intervals it appears that the longer the time interval the larger the PO changes (Figure 3.10c). This suggests that PO changes are a contributing factor to the time dependent decay in tuning curve similarity as measured by pairwise signal correlation decay (Figure 3.9c).

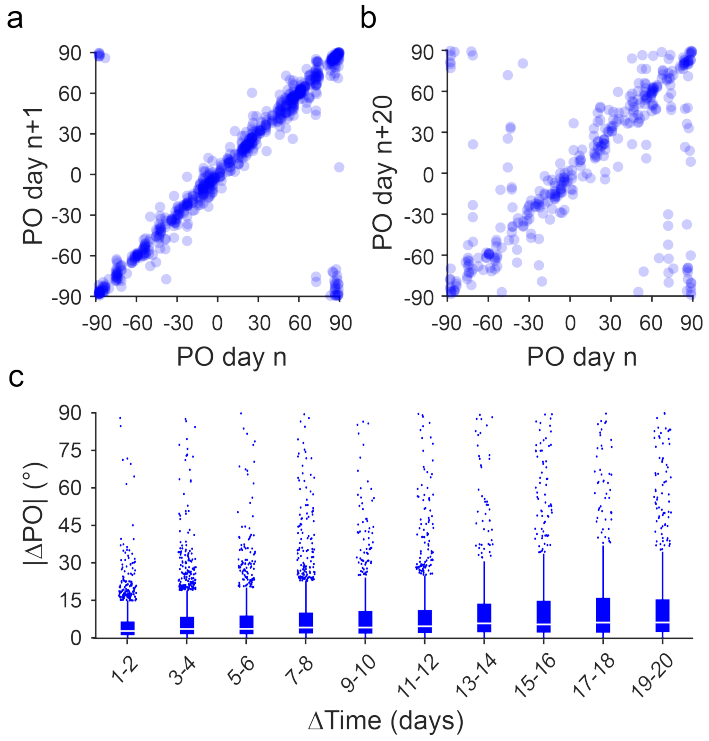

Figure 3.10: Preferred orientation of individual neurons becomes increasingly dissimilar as a function of time interval. a) Start and end preferred orientation (PO) from all comparisons 1 day apart (e.g. day 1 vs 2, and day 7 vs day 8). Circular-circular Pearson's correlation r = 0.968 ($p < 0.005$), n = 781 comparisons from 169 neurons in 5 mice. b) Same as a but for sessions 20 days apart. Circular-circular correlation r = 0.800 ($p < 0.005$), n = 360 from 170 neurons in 5 mice. c) Box plot of absolute change in PO across different time intervals. Each data point is a change in PO across two sessions. n = 11891 from 320 neurons in 5 mice.

Changes in response amplitudes and signal-to-noise ratios could in principle lead to increasingly large apparent PO changes over time. To control for this possibility, a significance threshold on PO changes was introduced by calculating the bootstrapped confidence interval of PO by resampling with replacement across individual stimulus presentations (Figure 3.11a). When applying this significance threshold, the absolute PO changes still increase with larger time intervals (Figure 3.11b) and the proportion of PO changes that passed the significance threshold also increased (Figure 3.11c). To quantify if these PO changes increase over time, the median PO change at different time intervals was plotted. Both for all PO changes and just the significant PO changes, the median of these changes increased as a function of time (Figure 3.11d-f). However, the small size of these changes that occur over a considerable period of time (median|ΔPO| of 0.3 °/day for the 19-20 day interval) indicates that although PO drifts, the degree of drift is small. Unfortunately, not all mice were imaged longer than 21 days, meaning beyond this interval the confidence in the median size of PO changes is lower. For this reason, I cannot accurately estimate when the PO drift saturates. Nevertheless, in the mouse with the highest number of chronically reidentified neurons (176), median PO changes plateaued after roughly 2 weeks, while in other mice a plateau was not evident (data not shown). Together these data show that, while PO drifts over time, on average this drift is small.

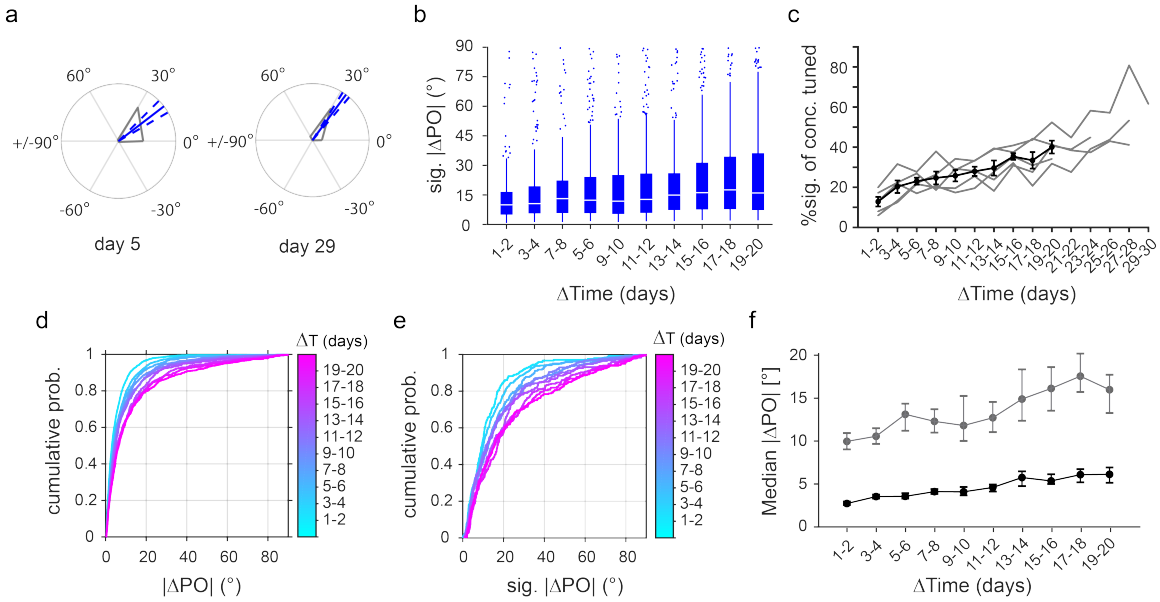

Figure 3.11: The number of statistically significant preferred orientation changes and their size increases as a function of time interval. a) Orientation tuning of an example cell on two days. Mean response amplitude to drifting gratings of six orientations (12 directions) shown in grey. Solid blue line indicates preferred orientation (PO), dashed blue lines indicate bootstrapped 95% confidence intervals. As the PO of the respective day's lie outside of the confidence intervals of the other day, the PO change is considered significant. b) Box plot of significant absolute changes in preferred orientation across different time intervals. Each data point is a change in preferred orientation across two sessions. n = 2895 intervals from 221 neurons in 5 mice. Data is binned based on time interval. c) The percent of PO changes that pass the significance threshold increases as a function of time interval. Individual mice indicated as grey lines, mean across mice indicated in black with error bars as S.E.M. d) Cumulative probability distribution of the absolute size of PO changes for different interval bins. e) Same as d but only including significant PO changes. f) Median absolute PO changes from distributions in d and e, black line: all PO changes, as in d, grey line: significant PO changes, as in e. Error bars are bootstrapped 95% confidence intervals.

3.2.3 Changing the statistics of the visual environment using cylinder lens goggles shifts the population distribution of preferred orientations

A recent study in olfactory cortex has shown that the frequency of stimulus exposure can stabilize stimulus representations (Schoonover et al., 2021). So far, it is unknown if daily exposure to basic visual features similarly stabilizes their representation in visual cortex. Cylinder lens goggles act as contour orientation filter (Figure 3.12), leading to increased exposure to the permitted orientation and eliminating exposure to others. Chronically mounting these goggles over the eyes of mice and housing them in cages with black stripes on the walls for 21 days (starting at P25) has been shown to alter the distribution of POs in V1 (Kreile et al., 2011), and to a lesser extent in adult mice (up to P100; Yoshida et al., 2012). This intervention is often referred to as stripe rearing. In this thesis, similar goggles were mounted over the eyes of P70 mice. For 7 mice the goggles remained on continuously for 28 days before imaging neurons again, while for 8 other mice the goggles were removed every 7 days for a few hours, during which PO was measured using drifting grating presentations. Similar to the previous study, the walls of the home cages were lined with strips of black tape roughly aligned to the permitted orientation of the cylinder lens goggles.

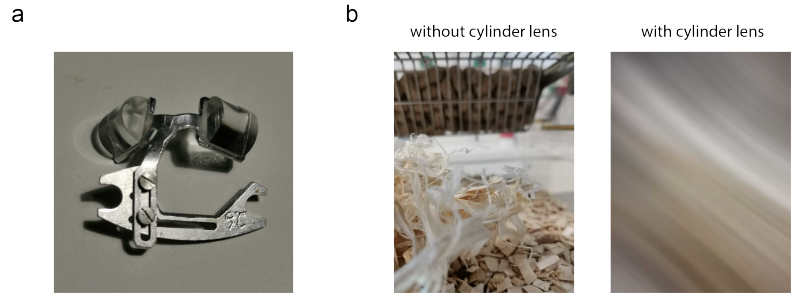

Figure 3.12: Cylinder lens goggles chronically restrict the range of experienced orientations. a) Top view of cylinder lens goggles mounted on a head bar. b) Photo of the home-cage environment without and with a cylinder lens mounted in front of the camera lens.

Similar to the previous study (Kreile et al., 2011), after four weeks of stripe rearing the distribution of POs was altered in favour of the permitted orientation of the cylinder lens goggles, but not after merely one week (Figure 3.13a-b). In contrast to the previous study, the same very neurons were recorded before and after stripe rearing with cylinder lens goggles. This allowed us to selectively analyse the PO distributions of neurons that remained visually responsive and concurrently tuned. Any changes in the PO distribution could then only be attributable to shifts in the PO of individual neurons. Here again, 4 weeks of deprivation altered the PO distribution in favour of the permitted orientation, while one week did not (Figure 3.13c-d). The population of neurons that either became responsive and tuned or unresponsive and untuned could be also isolated (Figure 3.13e-f). Neither one nor four weeks of deprivation caused a statistically significant change in the PO of this group, although there was a statistically nonsignificant tendency for neurons to gain responsiveness and or tuning with a PO around the permitted orientation after 28 days.

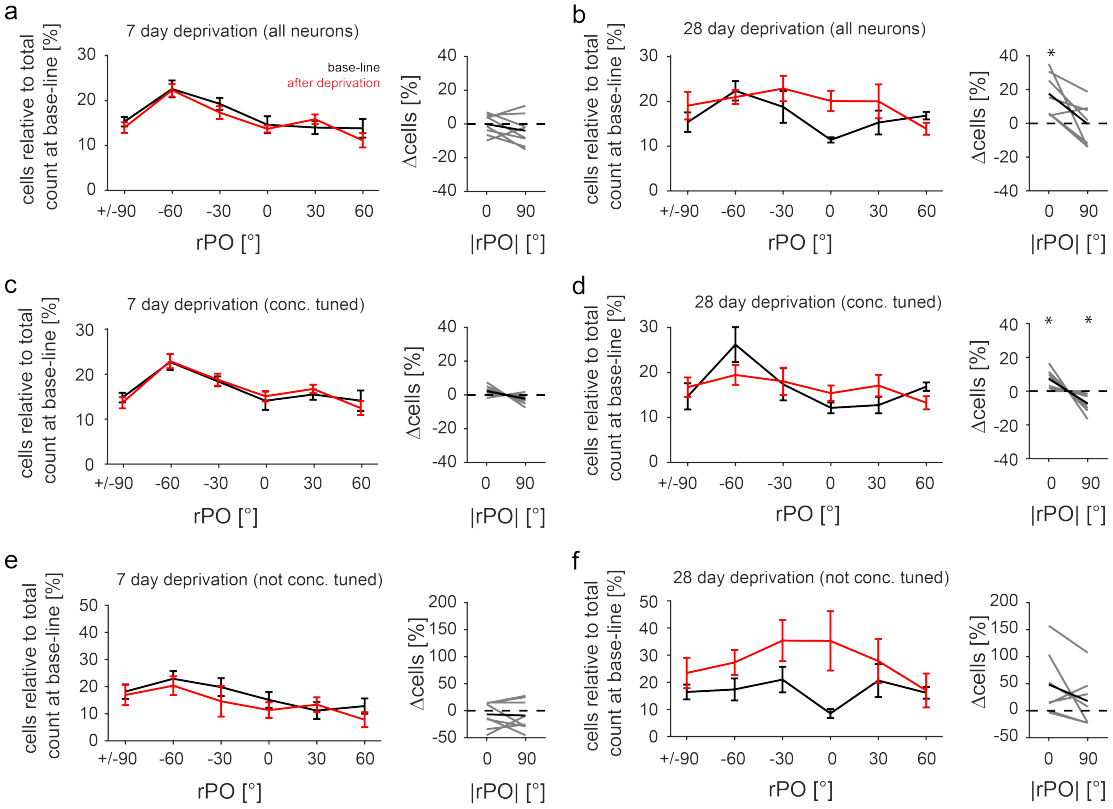

Figure 3.13: The population distribution of preferred orientation shifts in favour of the permitted orientation after 4 but not 1 week of stripe rearing. a) Left: Distribution of PO (relative to the permitted orientation of cylinder lens goggles) before deprivation at baseline (BL; black) and after 7 days of deprivation (red). Bin size 30°. Right: % change in the number of neurons with absolute difference in PO from the permitted orientation split into two bins (0 to +/-45° and +/-45° to +/-90°). Single mice in grey, mean across mice in black. Dashed black line indicates 0. The difference from zero is not significant for either bin. X axis values are bin centres. n = 8 mice. b) Same as a but for 28 days of continuous deprivation. The 0° bin in the right plot significantly above 0 ($p = 0.011$). The difference from 0 is not significant for bin 90°. n = 7 mice. c) Same as a but only for neurons that were visually responsive and tuned before and after deprivation. The difference from 0 is not significant for either bin in right plot ($p = 0.062$ and $p = 0.062$). n = 8 mice. d) Same as c but for 28 days of continuous deprivation. The 0° bin in the right plot is significantly above 0 ($p = 0.018$). The 90° bin is significantly below 0 ($p = 0.018$). n = 7 mice. e) Same as a but only for neurons that were not visually responsive and/or tuned before and after deprivation. Here, changes in the distribution can only be caused by neurons gaining or loosing visual responsiveness and/or tuning. Difference from zero is not significant for either bin in right plot. n = 8 mice. f) Same as e but for 28 days of continuous deprivation. Difference from zero is not significant for either bin in right plot ($p = 0.080$ for bin 0°). n = 7 mice. Significance of difference from zero was determined using one-sample two-tailed t-test. All error bars indicate S.E.M. across mice.

3.2.4 Stripe rearing affects the direction of preferred orientation drift but not its magnitude

After confirming the findings from Kreile et al., (2011), the question remained how individual neuron PO changes lead to the overall population distribution changes (Figure 3.13). Specifically, which neurons change their PO in what direction, and by how much? To this end, the distribution of the absolute PO changes relative to the permitted orientation of the cylinder lens goggles ($\Delta|\text{rPO}|$) was quantified. For control mice that were not stripe reared, rPO was defined as PO minus the average permitted orientation of the cylinder lens goggles mounted on stripe reared mice (-32.6°). If a neuron's $\Delta|\text{rPO}|$ is positive, then the PO shifted closer to the permitted orientation. A median $\Delta|\text{rPO}|$ above 0° then indicates an overall convergence of PO towards the permitted orientation. In mice without cylinder lens goggles, intervals of 7-8 days resulted in an average $\Delta|\text{rPO}|$ of 0° (Figure 3.14a, b and g), while for 7 and 28 days of stripe rearing, $\Delta|\text{rPO}|$ was 1.2° and 2.8° respectively (Figure 3.14c-g). Interestingly, for the 7 day deprivation cohort, additional deprivations with interleaved PO measurements every 7 days did not lead to an increase in the average convergence towards the permitted orientation (Figure 3.14g). This suggests that a few hours of exposure to drifting gratings, necessary to measure PO, was sufficient to prevent further drift in the direction of the permitted orientation.

Given that the direction of drift was influenced by restricting the experience of orientations during stripe rearing, the overall magnitude of PO drift may also be expected to increase. After 7 days of stripe rearing, the median PO change was slightly elevated, but for longer time intervals it was similar to the PO change without stripe rearing (Figure 3.15a). It should be noted, that the baseline estimate for 28 days is based on only 3 mice and is therefore less reliable.

A previous study in mouse piriform cortex shows that odour representations are more stable when the odour is experienced more frequently (Schoonover et al., 2021). We therefore hypothesised that the deprivation of certain orientations during stripe rearing would destabilize the representations of those orientations in V1. However, neurons with POs that were distant from the remaining experienced orientations (beyond 30°) did not drift more than those with POs close to the remaining experienced orientations (within 30°; Figure 3.15b-g). This argues against the hypothesis that visual experience of specific features stabilizes their representation in V1.

Taken together, these results argue against the hypothesis that constant experience of oriented contours stabilizes their representation in V1, but rather show that the experience of one orientation of contours alone pulls the population representation toward this remaining experienced orientation.

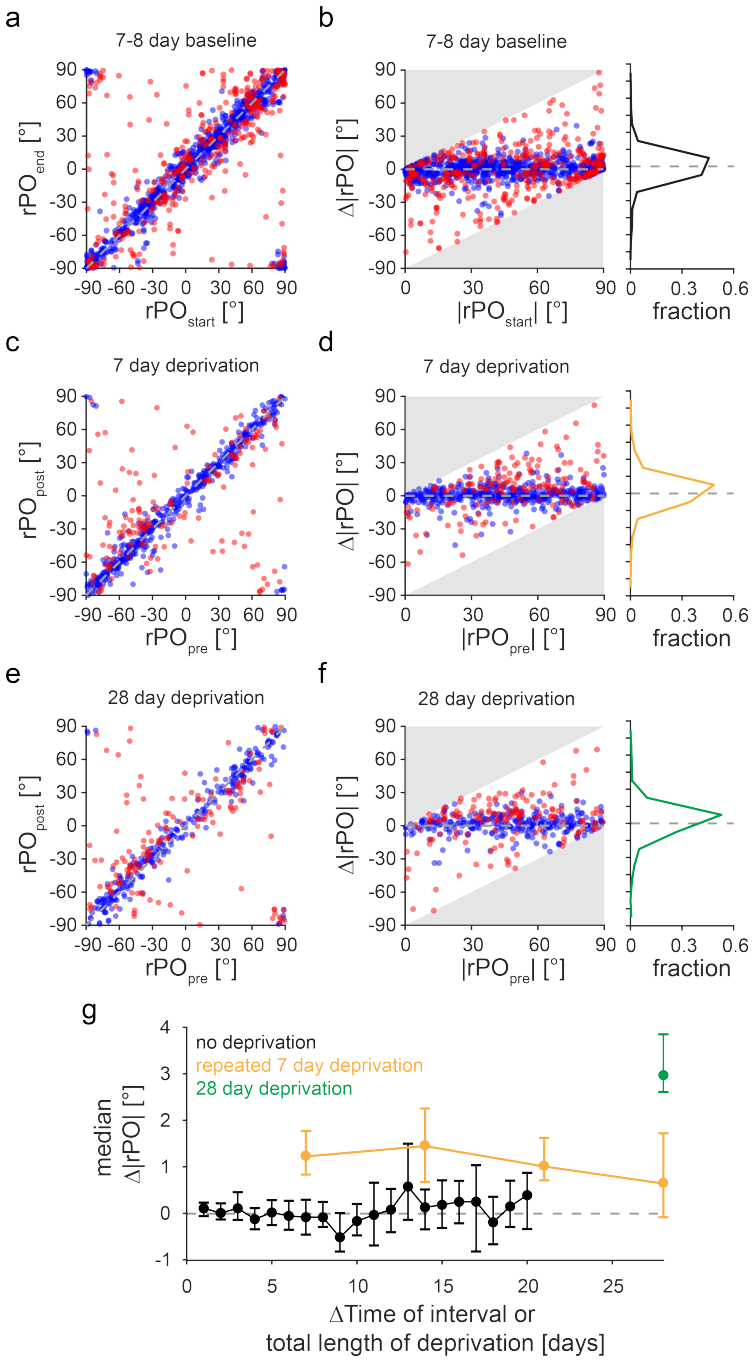

Figure 3.14: Stripe rearing causes PO to drift towards the experienced orientation. a) Scatter plot of relative PO (rPO) at the start and end of 7-8 day intervals without cylinder lens goggles. Red data points in a-f indicate significant changes. b) Left: Scatter plot of the initial absolute rPO versus the change in the absolute rPO after 7-8 days. Positive $\Delta|\text{rPO}|$ indicate changes toward the average permitted orientation of cylinder lens goggles on deprived mice. Right: histogram of overall $\Delta|\text{rPO}|$ distribution (n = 1475 intervals, from 255 cells in 5 mice). c-d) same as a-b, but for 7 days of deprivation with cylinder lens goggles (n = 601 intervals from 601 cells in 8 mice). e-f) same as c-d, but for 28 days of stripe rearing. n = 414 intervals from 414 cells in 7 mice. g) Black: median $\Delta|\text{rPO}|$ across 1-20 day intervals of non-stripe reared mice. Orange: consecutively repeated 7 day deprivation, x-axis indicates the time from first deprivation onset. Green: 28 days of continuous deprivation. Error bars indicate 95% confidence intervals based on bootstrap resampling across single cell PO changes.

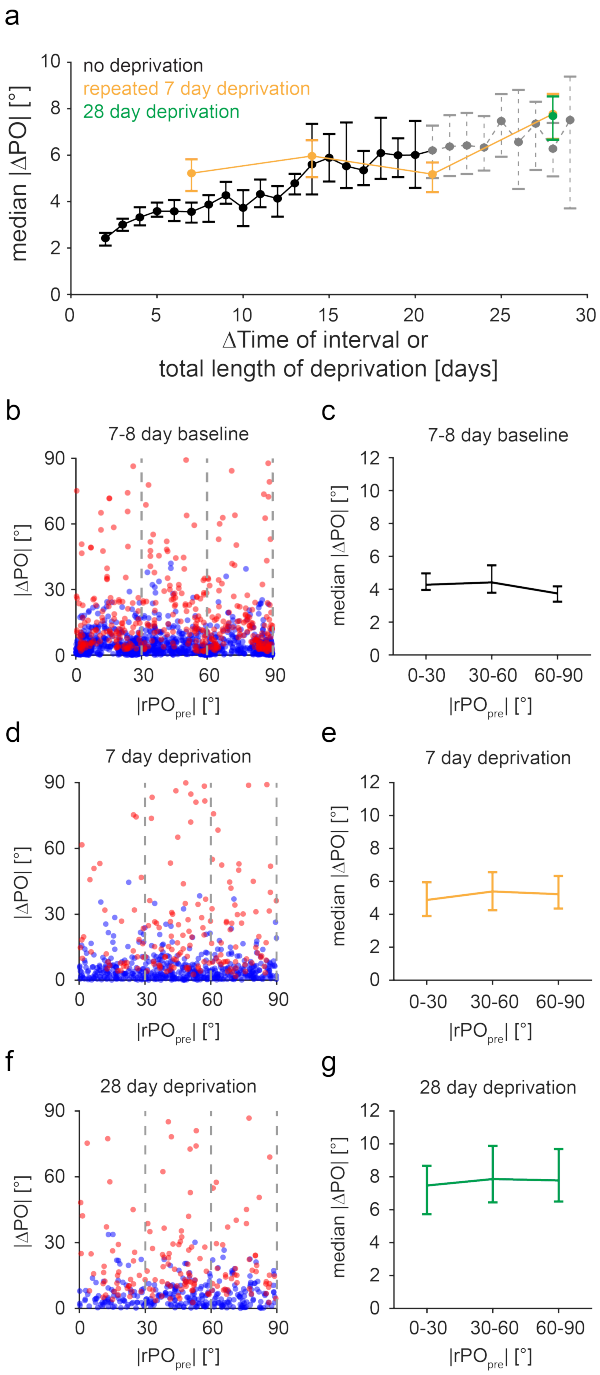

Figure 3.15: PO drift magnitude is largely unaffected during stripe rearing. a) Median absolute PO change (|ΔPO|) across different time intervals. Black and grey: mice with no with no cylinder lens goggles (black: n = 5 mice, grey: < 5 mice). Orange: repeated 7 day stripe rearing indicated in orange (8 mice). Green: continuous stripe rearing for 28 days indicated (7 mice). Error bars indicate 95% confidence interval based on bootstrap resampling. b) Scatter plot of distance from permitted orientation at the start of 7-8 day intervals versus absolute PO change in the absence of stripe rearing. Red data points indicate significant PO changes. Grey dashed lines indicate bin edges for plot in c. c) Line histogram of median PO change across distance from permitted orientation. Error bars are bootstrapped 95% confidence internals (n = 1475 intervals, from 255 cells in 5 mice). d-e) Same as b-c but for 7 days of stripe rearing (n = 601 intervals from 601 cells in 8 mice). f-g) Same as b-c but for 28 days of continuous stripe rearing (n = 414 intervals from 414 cells in 7 mice).

3.2.5 Cell-specific restoration of preferred orientation after recovery from stripe rearing

For mice that underwent continuous stripe rearing for 28 days, the goggles were subsequently removed and the mice returned to cages without striped walls for 21 days, before measuring the PO of V1 neurons a final time. The population distribution of POs returned back to the original distribution observed before the goggles were fixed to the mice (Figure 3.16a-b). Furthermore, the $\Delta|\text{rPO}|$ during stripe rearing versus recovery was negatively correlated, and the median $\Delta|\text{rPO}|$ was positive during the deprivation interval and negative during the recovery interval (Figure 3.16c-d). Furthermore, the median $\Delta|\text{rPO}|$ from before deprivation onset to after recovery was not significantly different from 0° (Figure 3.16e). Taken together, on a single cell level, the neurons that shifted their PO during stripe rearing, on average, shifted back from whence they came.

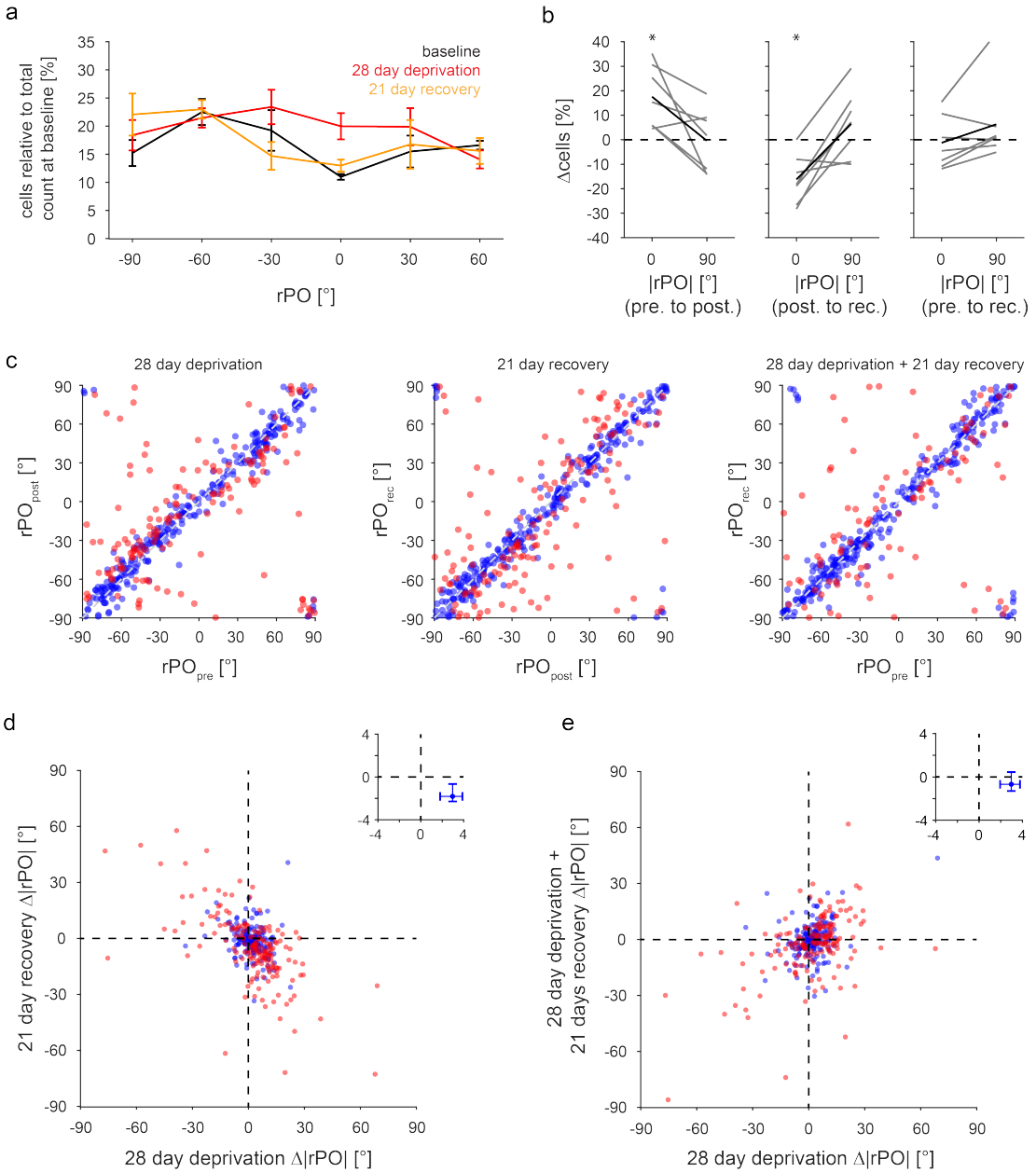

Figure 3.16: Population and cell-specific recovery. a) Distribution of PO relative to the permitted orientation (rPO) before deprivation (black), after 28 days of continuous deprivation (red), and after 21 days of recovery from deprivation (orange). Bin size 30°, x axis values are bin centres. Error bars indicate S.E.M across mice, n = 7 mice. b) % change in the number of neurons with absolute rPO closer to or further from the permitted orientation. Bins are 0 to +/-45° and +/-45° to +/-90°, x axis values are bin centres. Single mice in grey, mean across mice in black. Dashed black line indicates 0. The number of cells with rPO closer to the permitted orientation than the orthogonal orientation increases significantly after 28 days of deprivation ($p = 0.011$, n = 7 mice) and decreases significantly after 21 days of recovery ($p = 0.005$, n = 7 mice), but shows no significant difference when comparing before deprivation to after recovery. Significance of difference from zero was determined using one-sample two-tailed t-test. c) Scatter plots comparing rPO of individual neurons at the three imaging time points. Significant PO changes in red. From left to right n = 414, 431 and 390 cells from 7 mice. d) Scatter plot of the change in absolute rPO of individual neurons from before to after deprivation versus after deprivation to after recovery. Only neurons that retained their visual responsiveness and orientation tuning on all three imaging timepoints were included. Data points from neurons that changed significantly in at least one of the time intervals are indicated in red. The median of all rPO changes across neurons is indicated in the inset on the top right with error bars indicating 95% confidence intervals based on bootstrap resampling. Pearson's correlation r = -0.569 ($p < 0.005$, n = 335 neurons from 7 mice). e) Same as d but comparing rPO changes from before to after stripe rearing, to changes from before stripe rearing to after recovery from stripe rearing. n = 335 neurons from 7 mice. Pearson's correlation r = 0.437 ($p < 0.005$, n = 335 neurons from 7 mice).

4. Discussion

4.1 Synaptic input selection limits eye-specific convergence in the mouse dLGN

The canonical role of the mammalian dorsal lateral geniculate nucleus (dLGN) of the thalamus is to relay segregated visual processing streams to the primary visual cortex (V1), with little to no combination of information from different retinal ganglion cells (RGCs), RGC types or the two eyes. Previous studies have found conflicting evidence for and against convergence of inputs from both eyes onto individual neurons in the mouse dLGN (Grubb and Thompson, 2003; Jaubert-Miazza et al., 2005; Zhao et al., 2013; Howarth et al., 2014; Sommeijer et al., 2017; Jaepel et al., 2017; Rompani et al., 2017; Huh et al., 2020). In light of these conflicting findings, *in vitro* two-colour optogenetic stimulation of RGC axons in dLGN was performed, while electrically recording from putative thalamocortical (TC) neurons. This approach avoided any di-synaptic sources of eye-specific convergence and allowed quantitative measures of the input provided by axons from either eye. TC neurons that received comparable input from RGCs of both eyes were very rare, but most cells in the binocular region of the dLGN received a low level of input from their non-dominant eye. This argues that at least with regard to binocularity, the dLGN of mice largely maintains the segregation of information streams, in line with the canonical view of dLGN.

Though TC neurons do not receive comparable input from both eyes in adult rodents, this is in stark contrast to early in development where eye-specific convergence at TC neurons is the norm (Žiburkus and Guido, 2006). Several mechanisms that could cause the low level of binocular integration at the retinogeniculate synapse in adulthood were evaluated, including: RGC projection segregation, dendritic bias, and synaptic selection and refinement. Synaptic depression of nondominant inputs was not considered as TC neurons begin by receiving many weak synapses early in development, which are reduced in number over time while the remaining inputs are strengthened heterogeneously (Chen and Regehr, 2000; Hooks and Chen, 2006; Lin et al., 2014; Litvina and Chen, 2017). Anatomical constraints that could bias the availability of eye-specific axons to TC neurons could not fully explain the low level of binocularity. In contrast eye-specific synaptic selection and, or, synaptic strengthening decreased the number of binocular cells by at least ~10 fold compared to indiscriminate sampling of available inputs. Based on the difference in the AMPA receptor (AMPAR) to NMDA receptor (NMDAR) response ratio between the dominant and non-dominant eye inputs, synaptic strengthening of the dominant eye inputs is likely the driving force behind this monocular bias.

Here, I will first outline the contradictory findings on mouse dLGN binocularity published in recent years and discuss how the data in my thesis might reconcile these disparate findings. I will also briefly discuss the implications of the lack of morphological TC neuron types in the present data. I will then discuss the mechanisms that could contribute to the low level of binocularity observed in mouse dLGN, and which of these mechanisms are supported by this thesis. Lastly, I will discuss if these findings generalize to RGC type convergence in the mouse LGN.

4.1.1 Reconciling disparate levels of dLGN binocularity from different experimental approaches

Based on studies in non-rodents, information from the two eyes was previously thought to be kept separate in the mammalian dLGN. Over the last two decades a number of experiments, using diverse techniques, measure the level of binocular integration in mouse dLGN, raising the question of whether this integration occurred one synapse earlier in the rodent visual system. These studies can broadly be grouped into: 1) *in vitro* input mapping, 2) retrograde rabies virus input tracing, 3) *in vivo* electrophysiological recordings, and 4) *in vivo* calcium imaging of axonal projections. These approaches have different advantages and drawbacks, such as specificity on the circuit level, physiological relevance, and throughput. The results from these different methods have produced divergent estimates of binocularity in dLGN. Here, I will outline these conflicting findings and discuss how the data in this thesis reconciles these seemingly contradictory findings.

The first two of the aforementioned approaches focus on the direct monosynaptic convergence of RGC inputs onto TC neurons. Two *in vitro* electrophysiology studies used optic nerve stimulation during intracellular recordings of putative TC neurons and found that the proportion of binocularly responsive neurons was high early in postnatal development but later declined until only few neurons responded to stimulation of both ipsi- and contralateral optic nerve stimulation (mice: Jaubert-Miazza et al., 2005; rats: Žiburkus and Guido, 2006). A limitation of these studies is that they did not test animals beyond P20, after which point retinogeniculate synapses still undergo maturation through pruning and strengthening (Chen and Regehr, 2000). In addition, they did not report the ratio between the ipsi- and contralateral input strengths of binocular cells, and the number of recorded dLGN cells was small. A recent study used retrograde rabies tracing from TC neurons to identify the type and eye of origin of RGC inputs (Rompani et al., 2017). They found that roughly half of TC neurons in the mediodorsal part of mouse dLGN were connected to RGCs from both eyes, and that no TC neurons solely received ipsilateral inputs. Although this study included a larger number of neurons and used somewhat older mice (P22-40), rabies tracing does not yield information about the strength of connections (Callaway and Luo, 2015), and it is possible that some of the traced inputs arise from silent synapses (i.e. synapses that do not contain AMPARs and therefore likely do not contribute significantly to postsynaptic cell activity). Furthermore, since none of the above studies precisely mapped out the location of each recorded neuron in the dLGN or their proximity to the ipsi- and contralateral projection zones, it is not possible to know if the discrepancies between the studies might also be caused by differences in sampling location.

In vivo recordings from TC neurons and their axonal projections in adult mice have reported a large range in their binocularity and were therefore likewise inconclusive. One study used *in vivo* electrophysiological recordings and found no binocular cells (Grubb and Thompson, 2003), while another study found a small number of binocular cells which were largely dominated by input from one eye (Zhao et al., 2013). However, two subsequent studies found almost exclusively binocular cells (Howarth et al., 2014; Sommeijer et al., 2017). A further study in rats also found many neurons with strong input from both eyes (Grieve, 2005). Two *in vivo* two-photon calcium imaging studies measured the responses of TC axons in mouse visual cortex, and found few strongly binocular boutons (Jaepel et al., 2017, Huh et al., 2020). Both, *in vivo* electrophysiological measurements as well as calcium imaging of TC axons, can suffer from source separation issues. For instance, neuropil contamination due to inadequately sparse axon labelling for calcium imaging or unsuccessful spike sorting from extracellular recordings are causes of signal contamination which would result in signal source mixing resulting in higher measured binocularity. In general, however, such *in vivo* approaches are advantageous because they measure physiological responses to actual sensory stimulation, but this can also make them harder to interpret than probing monosynaptic responses as in *in vitro* electrophysiology. Reasons for the diverging results among *in vivo* studies may be the different visual stimulation types (either full field luminance changes, full field or subfield drifting gratings) or the statistical criteria for responsiveness and binocularity. Some of these binocular responses likely arose from multisynaptic binocular integration, such as through direct and indirect feedback from V1 to dLGN TC neurons. It is also possible that the different visual stimuli, which varied across studies, have different propensities for recruiting such feedback

circuitry. All of these differences make it hard to compare the level of reported binocularity across these publications, and consequently, I have omitted quoted estimates from these studies. Taken together, the collection of publications over the past two decades have given a confusing and unclear picture of the level of binocular integration in the mouse dLGN.

Despite these contradictory findings, the mouse dLGN was increasingly being seen as having higher levels of binocular convergence than cats and primates (Wallace et al., 2016; Rose and Bonhoeffer, 2018; Kerschensteiner and Guido, 2017). This was an interesting and intriguing idea, primarily because a higher degree of channel mixing in mice fell in line with the fact that mouse dLGN was less structurally organized, with no obvious lamination. Around the same time, it was also found that many neurons in the koniocellular layers of primate LGN (the layers between the M and P layers in primates) responded strongly to stimulation of either eye (Zeater et al., 2015). This suggested that binocularity may be much more widespread in other mammalian LGNs than previously thought, contradicting the canonical view that the LGN in mammals acts like a simple relay. Nevertheless, the idea that mouse dLGN had widespread binocular integration was based on contradictory results that needed clarification.

In an attempt to reconcile the diverse TC neuron binocularity reported in literature, *in vivo* calcium imaging of TC projections to V1 (Bauer et al., 2021) and the *in vitro* input mapping approach outlined in this thesis (Bauer et al., 2021; section 3.1) was used. Boutons on dLGN axons in V1 were imaged across a range of conditions that varied in visual stimulation (full field luminance fluctuations and subfield drifting gratings), cortical depth of the boutons and elevation in visual field. When considering the relative response amplitude from both eyes, there were very few boutons that had non-dominant response amplitudes greater than half the size of the dominant response. This resulted in an average monocularity across all conditions of above 0.8 (corresponding to a dominant to non-dominant input ratio of roughly 10:1). In fact, most boutons only showed detectable responses to visual stimulation of either the ipsi- or the contralateral. The exact fraction of binocularly responding TC boutons varied across conditions. The primary factor that contributed to different levels of binocularity was the statistical threshold for responsiveness, with other factors such as visual stimulus type playing a smaller role. This makes sense because raising the significance threshold increases sensitivity at the cost of also increasing the number of false positive responses to the non-dominant eye, with both effects leading to increased apparent binocularity. Differences in responsiveness criteria and signal to noise ratios are therefore the most likely reason why some *in vivo* electrophysiological studies (Howarth et al., 2014; Sommeijer et al., 2017; Grieve, 2005) found high levels of binocularity.

The second approach (outlined in this thesis), involved optogenetic stimulation of RGC axons in dLGN using two different light sensitive ion channels (ChrimsonR and Chronos), while patch-clamp recording from putative TC neurons in slices of the dLGN. As mentioned above, the major advantages of this technique are that it isolates the monosynaptic RGC inputs and is sensitive to very weak, as well as AMPAR silent inputs. Most recorded neurons received some level of input from both eyes (64%; Figure 3.2a), roughly aligning with the rabies tracing estimates (40-50%; Rompani et al., 2017). For the 10 TC neurons that Rompani et al., (Rompani et al., 2017) reports as being binocular, the neurons received input from ~3x as many RGCs from their dominant compared to their non-dominant eye (ranging from 1.5x to 31x, median ~3x; calculated from Figure S5c of Rompani et al., 2017). On the other hand, for the 75 binocular TC neurons in the dual colour optogenetic input mapping dataset presented here, each neuron received on average 30 times more input from their dominant eye compared to their non-dominant eye (Figure 3.2a-b). This indicates that despite receiving input from both eyes, taking the number and strength of inputs into account, the total input from one eye usually dominates.

I mapped the dual colour optogenetic input mapping dataset, as well as a previously published dataset on retinotopy (Piscopo et al., 2013), to a 3D model of dLGN and found that binocular integration is low across all retinotopic positions (Figure 3.3c). After compensating for uneven sampling across the dLGN, the estimated total fraction of functionally binocular TC neurons was 0.9% (Figure 3.2c; the criteria for functionally binocular being: that the non-dominant input was at least half as large as the dominant input). Taken together, the data in this thesis show that although many TC neurons receive some small amount of input from both eyes, the input from one eye is usually much stronger. The discrepancy in the *in vitro* literature on eye-specific

RGC convergence in dLGN (Jaubert-Miazza et al., 2005; Rompani et al., 2017) can therefore be explained if retrograde rabies tracing is agnostic to synaptic strength.

In light of the results in this thesis, the recently emerging view that mouse dLGN performs widespread binocular integration (Wallace et al., 2016; Rose and Bonhoeffer, 2018; Kerschensteiner and Guido, 2017), is questionable. Given previous estimates of the total number of neurons in mouse dLGN (Evangelio et al., 2018), the results would translate to around 200 of the 20000 neurons in dLGN showing strong responses to stimulation of both eyes. It is, however, possible that these ~200 neurons perform specialized computations (for instance by combining information from specific RGC types, necessary for downstream computations) or reflect the error tolerance of the wiring rule.

4.1.2 No TC neuron morphology types in dLGN

dLGN TC neurons in mice have previously been reported to have one of three distinguishable morphologies (X, Y and W; Krahe et al., 2011). These three morphology types were likened to the three morphologically and functionally distinct TC neuron types described in cat dLGN (Stone, 1983; Hamos et al., 1987). The dendritic morphologies of TC neurons in the dataset presented here were originally traced in order to sort them into these three categories. I expected that ipsilateral dominated cells would primarily have X like morphology due to the reported location of X type cells. These three cell types were identified in a previous study using a metric termed DOi (dendritic orientation index), which was reported to show three separable distributions, corresponding to the three cell types (Krahe et al., 2011). In the data presented in this thesis there were no separable distributions of DOi values (Figure 3.4). In an effort to characterize the features that define X, Y and W cells (X: radially symmetrical, Y: elongated along one axis, W: asymmetrical relative to soma) in separate dimensions, I quantified elongation and asymmetry separately. Again, there were no separable distributions. Though contradicting the findings of Krahe et al., (Krahe et al., 2011), this matches another study that found no separable morphological types using electron microscopy data (Morgan et al., 2016). Furthermore, it also aligns with genetic studies that failed to find separable cell types based on mRNA expression patterns (Kalish et al., 2018; Bakken et al., 2021). Given these data, it is questionable if TC neurons are classifiable into different cell types on the basis of morphology or genetics in the mouse, and until further experiments demonstrate otherwise, TC neurons should probably not be treated as such.

4.1.3 To what degree does eye-specific RGC projection segregation contribute to eye-specific channel segregation?

Before the view emerged that mouse dLGN might be more binocular, the prevailing assumption was that ipsi- and contralateral responsive cells were segregated because of the segregation of eye-specific RGC axons. This view implicitly meant that during development the number of binocular dLGN neurons dropped because of ongoing RGC axon segregation (Grubb and Thompson, 2003; Jaubert-Miazza et al., 2005; Coleman et al., 2009). This was entirely plausible since RGC boutons are generally located on proximal dendrites of TC neurons (Rafols and Valverde, 1973; Morgan et al., 2016); so even if some dendrites crossed into the region of the other eye (Krahe et al., 2011), TC neurons in the ipsilateral projection zone should have better access to ipsilateral inputs. However, this was not directly tested by mapping out ipsi- and contralateral RGC axons relative to the recorded cells. Therefore, until now, this was not directly demonstrated. Because the dendritic morphology of the TC neurons as well as the location of eye-specific projection zones were acquired and quantified, this hypothesis could be directly tested for the first time.

The spatial arrangement of RGC axons and postsynaptic dendrites could influence monocularity in two ways: either axon segregation alone could increase the level of monocularity, or the shape of TC neuron dendrites with respect to the eye-specific projection zones could increase the level of monocularity. To test these two mechanisms separately, I first assumed that all neurons have radially symmetrical dendrites. In order to estimate an upper limit of the effect of eye-specific axon segregation, I binarized the tdTomato and EGFP fluorescence ratios of each slice, simulating perfect axon segregation. The average radial dendritic density of reconstructed TC neurons was

then used to sample across the binarized dLGN fluorescence stacks, obtaining distributions of relative input availability for each brain slice (Figure 3.5). If eye-specific axon segregation was absent, then there would have been no positions in the dLGN with higher ipsilateral compared to contralateral input availability, given the relative number of RGCs projections from both eyes. On the other hand, if axon segregation was the primary cause of monocularity of TC neurons in the dLGN, then there should be very few locations in which neurons had roughly equal access to both inputs. However, under the simulated conditions there were about the same number of locations that were dominated by ipsilateral input as there were locations that had roughly equal access to inputs from both eyes. This shows that eye-specific RGC axon segregation results in locations where TC neurons have greater access to ipsilateral inputs, but it cannot explain the low level of binocularity found in the data. In fact, binocularity in dLGN was found to be 10 times lower than this simulation of local input pooling would predict (Figure 3.5f).

The second conceivable way in which axon segregation could contribute to decreasing binocularity in the dLGN is by TC neuron dendrites selectively avoiding one of the two projection zones. In order to test this, the dendritic arbours of TC neurons were rotated and an estimate of the relative axon availability at different rotation angles was obtained (Figure 3.6). The axon availability based on dendritic rotation was easured by the mFD metric (morphology-based fluorescence difference). For some neurons, rotation changed the relative availability of inputs (Figure 3.6b) and decreased predictability of eye preference from mFD (Figure 3.6c). However, rotation had no effect on the overall level of binocularity. Axodendritic overlap is therefore predictive of eye preference for individual cells, but dendritic morphology does not enhance the effectiveness of RGC segregation at reducing binocularity.

Although in mice TC neuron dendrites are not biased towards either the ipsi- or contralateral RGC projection zones, such biases have been observed elsewhere. For instance, in L4 spiny stellate neurons in cat and primate V1. These cortical stellate neurons selectively arborize within the home ocular dominance column allowing both TC projection segregation and dendritic bias to work in tandem (Katz et al., 1989; Kossel et al., 1995). Based on the timing of the development of TC neuron dendrites in mice, a similar bias should be possible. RGC projection segregation completes slightly before TC neuron dendrites reach their full size (Godement et al., 1984; Krahe et al., 2011). If TC neuron dendritic branches are stabilized through synaptic activity, as they are for other neurons (Rajan and Cline, 1998; Butz et al., 2009), this could lead to dendritic biases to either the ipsi- or the contralateral projection zones. During this period, TC neurons still have a large number of weak synapses (Chen and Regehr, 2000) and there are some reports that binocular responses are still common (Jaubert-Miazza et al., 2005; Žiburkus and Guido, 2006). The lack of dendritic bias could suggest that the specificity of postsynaptic activity may not be high enough to direct dendritic growth with respect to the RGC projection zones. Though speculative, it would be interesting to know if developing TC neuron dendrites possess the potential for activity guided growth, and if so, why this is not expressed with respect to the eye-specific RGC projection zones.

4.1.4 Eye-specific input selection and synaptic strengthening as mechanisms for channel segregation in dLGN

Because eye-specific RGC axon segregation and dendritic asymmetries cannot explain the low level of binocularity, input selection and strengthening could play a significant role in separating eye-specific channels in dLGN. This is particularly evident in such cases where neighbouring neurons with overlapping dendrites and similar morphologically based fluorescence difference (mFD: estimate of axodendritic overlap) values have opposite eye preferences (Figure 3.7). TC neurons in the adult mouse therefore do not indiscriminately sample across all inputs they have access to. Instead, eye-specific axodendritic overlap skews the probability of a TC neuron being dominated by input from one eye or the other, but each TC neuron eliminates or strengthens select few inputs from the many weak ones it initially starts with early in development (Chen and Regehr, 2000).

The question then is which of the two mechanisms, synaptic selection or synaptic strengthening, contributes more strongly to the development of monocularity. In the first case, TC neurons would selectively eliminate synapses connecting to axons from one eye, while in the latter, synapses from one eye would be selectively strengthened. These mechanisms are by no means mutually

exclusive, meaning that demonstrating the presence of one does not eliminate the possibility of the other also being true. Minimal stimulation protocols (reducing excitation strength until only a few inputs are activated) during *in vitro* electrophysiological recordings have been used to assess the overall distribution of retinogeniculate synaptic strengths in the past (Chen and Regehr, 2000). Unfortunately, using a minimal stimulation protocol to obtain the distribution of synaptic inputs from both eyes did not work, because the smallest synaptic inputs were below the noise threshold. This would have been necessary to conclusively determine whether synaptic selection or strengthening contributed more towards the emergence of monocularity. However, I consider an eye-specific synaptic strengthening process to play a somewhat more important role for the following reasons.

Firstly, ipsilaterally dominated neurons located in the contralateral projection zone were more binocular than those in the ipsilateral projection zone, and vice versa (Figure 3.3b). This could result from neurons first unselectively receiving inputs from axons in their vicinity and then strengthening a small number of inputs from one eye, making that eye dominant. If a neuron strengthens one to two inputs from the eye it receives fewer inputs from, then the sum of the weak inputs from the non-dominant eye would be greater than if it had strengthened one to two inputs from the eye it had more weak inputs from. For example, if a neuron initially receives 3 weak ipsilateral inputs and 7 weak contralateral inputs, and then strengthens 1 ipsilateral input, it would end up having 1 strong ipsilateral input, 2 weak ipsilateral inputs and 7 weak contralateral inputs. On the other hand, if one of the contralateral inputs is strengthened then the neuron would end up with 3 weak ipsilateral inputs, 6 weak contralateral inputs and 1 strong contralateral input. The assumptions for such a scenario are, that initial synaptic selection is relatively unbiased and that the synapses that are strengthened come from the same eye. Higher binocularity for neurons outside of their expected projection zone, therefore argues in favour of these two assumptions.

Secondly, in the retrograde rabies virus tracing study by Rompani et al. (2017), TC neurons that received input from both eyes on average received input from ~3 times as many RGCs from the dominant eye (median across 10 TC neurons calculated from Figure S5c of Rompani et al., 2017). This ratio is substantially lower than the ~30 times higher overall input strength from the dominant eye measured using dual-colour optogenetic input mapping (Figure 3.2c). Binocularity measured based on the functional input ratio is therefore much more biased toward one eye than the relative number of input RGCs.

Thirdly, in binocular TC neurons, non-dominant inputs had substantially lower AMPAR to NMDAR response ratios, compared to the dominant eye inputs (Figure 3.8a). AMPAR to NMDAR response ratios (A/N ratio), measured using single fibre (axon) stimulation, are known to increase with age in mouse dLGN, which has previously been attributed to a maturation of the retinothalamic synapse and a reduction in silent synapses (Chen and Regehr, 2000). This maturation, however, may not be uniform across synapses, with higher levels of maturation occurring at strongly potentiated synapses. This could result in an A/N ratio increase as a function of synaptic strength (Figure 3.8b). The total RGC input strength to TC neurons is known to be dominated by a small number of very strong inputs, with a larger number of weaker inputs (~10 total functional inputs with only ~3 strong inputs; Litvina and Chen, 2017). Therefore, the few strong synapses that likely come from the same eye might have even higher A/N ratios as would be predicted from the fitted exponential in Figure 3.8b. This is because the overall A/N ratio of inputs from one eye reflects the average of both strong (probably with low A/N) and weak inputs (probably with high A/N). If true, this would explain why the AMPAR response based monocularity is higher than the NMDAR response based monocularity (Figure 3.8c), as the NMDAR number would be less heterogeneous than the AMPAR number. Unfortunately, the A/N ratio as a function of AMPAR response strength (or the slope of AMPAR to NMDAR response) for single inputs has not been reported for the retinogeniculate synapse. However, in hippocampal CA1 dendritic spines the slope of NMDAR response strength with respect to AMPAR response strength is ~0.23 (inferred from Figure 7H of Noguchi et al., 2005), suggesting that synaptic potentiation increases AMPAR number more strongly than NMDAR number. It is therefore plausible, that a similar effect occurs at the retinogeniculate synapse. In order to quantify the relationship of AMPAR to NMDAR response strength at single retinogeniculate synapses, single fibre stimulation (as in Chen and Regehr, 2000) or two-photon glutamate unchanging (e.g. as in Noguchi et al.,

2005) could be used in future experiments.

Nevertheless, as axodendritic overlap fails to explain the high level of monocularity, synaptic selection and strengthening are the most probable mechanisms. Though the data in this thesis cannot conclusively demonstrate if eye-specific synaptic selection or strengthening plays a larger role, the three reasons given above argue in favour of eye-specific synaptic strengthening playing the crucial role in increasing TC neurons monocularity.

4.1.5 Implications for other forms of visual stream segregation and integration

The canonical view of the mammalian dLGN is that TC neurons relay information from RGCs to V1. Recent studies have called into question whether RGCs from both eyes (Howarth et al., 2014; Sommeijer et al., 2017; Rompani et al., 2017) and from different RGC types (Rompani et al., 2017; Liang et al., 2018; Rosón et al., 2019) connect to different TC neurons in mice. In this thesis, I have shown that TC neurons receive the majority of their input from one eye only, contradicting some of these publications (Howarth et al., 2014; Sommeijer et al., 2017), but aligning with the canonical view. The dual-colour optogenetic input mapping approach would also be ideal for assessing the level of convergence of different RGC types onto TC neurons.

In primates and cats, dLGN neurons are often dominated by a single RGC input (Sincich et al., 2009; Masri et al., 2020; Usrey et al., 1999; Kremkow and Alonso, 2021), whereas in mice, RGCs of different types seem to converge onto the same TC neurons. For instance, RGC boutons that share selectivity to some features while differing in others converge in clusters on the same TC neuron dendrites (Liang et al., 2018). TC neuron visual responses are also congruent with a convergence of a few RGC types (Rosón et al., 2019). These studies suggest a higher degree of convergence of RGC types onto TC neurons, compared to primates and cats. Although the evidence in favour of RGC type convergence based on *in vivo* recordings is arguably stronger and more consistent than for binocular convergence, direct input mapping in the fashion presented in this thesis, should still be done to confirm these results.

A recent study has investigated the level of convergence of ON-OFF direction selective retinal ganglion cells (ooDSGC) onto dLGN neurons (Jiang et al., 2022). To do this, the authors transduced ooDSGC types that preferred either vertical movement (both dorsal movement preferring ooDSGCs and ventral movement preferring ooDSGCs) or only ventral movement with channelrhodopsin-2 in separate animals. They compared the postsynaptic currents induced either through optogenetic stimulation of ooDSGC subtypes or through electrical stimulation of the optic tract. This gives a rough estimate of the relative contribution of the ooDSGC type to the total RGC input to the TC neuron. They found that the two groups of ooDSGCs generally only weakly drove TC neurons, with $< 5\%$ of TC neurons receiving ooDSGC input that contributed over 50% of their total retinal input. By comparing distributions of the normalized currents measured across the recorded population, they showed that the response amplitudes evoked through stimulation of either the vertical movement or ventral movement only preferring ooDSGCs was congruent with a model in which ooDSGCs with opposite direction preference generally innervated separate populations of TC neurons. This approach is not as direct as the one described in this thesis, but it nevertheless argues in favour of mouse dLGN maintaining separation of RGC types. However, the separation of RGC types is likely to be specific to the RGC types being compared. In the case of ooDSGCs tuned to movement in opposite directions, as well as RGCs from different eyes, they are less likely to be coactivated than, for instance, ventral movement preferring ooDSGCs and horizontal contour selective (i.e. orientation selective) RGCs. It would be interesting to identify the RGC types that most commonly converge, or are least likely to converge, using previously published *in vivo* datasets (Rosón et al., 2019), and systematically test these pairs using the dual-colour optogenetic input mapping approach described in this thesis.

At this point it is not clear to what extent the information from different RGC types converge onto TC neurons in mice. *In vivo* recordings argue in favour of higher levels of convergence than in monkeys and cats but not indiscriminate mixing. In general, I do not think that the low level of binocular integration shown in this thesis, or that of oppositely tuned ooDSGCs recently reported (Jiang et al., 2022), generalizes to all combinations of RGC types. Both of these are examples where

the activity patterns evoked by retinal waves, or the visual environment, have low or even negative correlation with respect to the two input types being compared. Further *in vitro* experiments systematically testing the convergence of pairs of RGC types onto TC neurons, using the wide range of RGC type driver lines (Martersteck et al., 2017), are therefore still needed. Additionally, it is not known if eye-specific RGC or RGC type convergence in dLGN is similar in other retinorecipient areas, such as the superior colliculus and could also be tested using the dual colour optogenetic input mapping approach.

4.1.6 Summary and outlook

Using data from the dual-colour optogenetic input mapping approach, I have shown that inputs from the two eyes generally do not provide comparable input strength to individual TC neurons in mice. The level of binocular retinogeniculate integration in the mouse dLGN is therefore much more similar to other mammals than has recently been suggested by *in vivo* recordings (Howarth et al., 2014; Sommeijer et al., 2017) and rabies tracing (Rompani et al., 2017). This fits the canonical view that eye-specific input channels are largely kept separate in the dLGN of mammals. In this thesis, I show that the segregation of eye-specific axonal projections cannot explain the low level of binocular integration, as has previously been assumed. Instead, input selection and strengthening decrease the level of binocularity by at least an order of magnitude compared to axon segregation alone. However, I was not able to definitively demonstrate that selective synaptic strengthening played a more important role than input selection, though several arguments strongly suggest this. Minimal stimulation of eye-specific inputs could solve this problem in the future. It would be interesting to know if this is similar in other mammals in which eye-specific projection segregation was also thought to cause the segregation of ipsi- and contralateral responsive TC neurons, such as in primates and cats. Recent experiments have found binocularly responsive neurons in monkey LGN koniocellular layers adjacent to the ipsi- and contralateral projection regions (Zeater et al., 2015). It is conceivable that these binocular koniocellular layer neurons in primates extend their dendrites into both projection zones and omit the synaptic selection and strengthening process observed in mouse dLGN.

A pertinent question is whether the finding that retinogeniculate convergence is lower than some *in vivo* studies have suggested, is also true for RGC type convergence. Another recent study has shown that ooDSGCs that have opposite movement direction preferences also generally do not provide strong input to the same TC neurons (Jiang et al., 2022). However, eye-specific input as well as opposing movement are likely to evoke low or negatively correlated activity in the RGC population. I therefore do not think that channel separation is necessarily a given between all pairs of RGC types.

Further experiments are still necessary to find out how widespread channel separation in mouse dLGN is, and whether axodendritic overlap or synaptic selection and strengthening play different roles for different combinations of RGC types. It would be useful if a precise map of axonal projection pattern of all RGC types was assembled for this purpose and compared to the existing *in vivo* datasets of RGC type integration by TC neurons (Rosón et al., 2019). I have mapped out the acquired data, as well as a previously existing dataset of dLGN retinotopy, to the three-dimensional model of dLGN within the ACCF and uploaded that data with spatial coordinates to an online repository. This has given me an appreciation for the complexity of understanding the three-dimensional nature of the dLGNs structural and functional organization. Given this complexity, it will be necessary for future experiments to make data available online with estimated recording positions within the ACCF. This would allow future analyses to consider the spatial organization of various anatomical and functional features and unify our understanding of the dLGN.

4.2 Stability and drift of orientation tuning in mouse V1

Representational drift, the continuous change in the response properties of neurons, challenges our understanding of how visual computations are reliably implemented and interpreted by the brain. Previous studies have identified representational drift in mouse V1 using tuning curve and population response similarity metrics. In this thesis, I for the first time show that a specific tuning feature, preferred orientation (PO), undergoes representational drift. In olfactory cortex, repeated exposure to odorants stabilized their neural representation (Schoonover et al., 2021). To test if the representation of visual features is likewise stabilized by their repeated exposure, cylinder lens goggles were used to remove contours with all but a limited range of orientations from the visual experience. Individual neurons that were not exposed to their PO for four weeks did not show increased PO drift compared to neurons whose PO was still experienced. However, the direction of PO drift shifted in favour of the experienced orientation resulting in a redistribution of POs across neurons. Neurons also recovered their initial PO after normal vision was restored for three weeks.

Here, I will first compare the finding of PO drift to a number of recent papers elucidating various aspects of drift in V1, highlighting how my findings contribute to this field. I will summarize a few possible behavioural and learning effects that could confound these findings. This will be followed by a discussion of what factors might alter tuning drift rate in a network. I will then discuss the possible consequences of drift in the visual system and what compensatory mechanisms might mitigate the negative effects of drift. Finally, I will mention several avenues that I believe will be interesting to follow up on in the future.

4.2.1 PO drift as a novel aspect of representational drift in V1

Representational drift and what visual tuning features it effects is not well defined. Various groups have published observations that fall within different interpretations of what representational drift encompasses. Here, I will use the following definition of representational drift: a decrease in neuronal tuning similarity as a function of time, that cannot be attributed to trial-to-trial response variability (adapted from Clopath et al., 2017; Rule et al., 2019). Disentangling the effects of variability (not intrinsically time dependent) and drift (intrinsically time dependent) is nontrivial, because both can result in the change of neural responses to the same stimuli measured at different times. However, their distinction is crucial, because different mechanisms likely underly both phenomena: response variability is likely caused by stochastic response properties, due to random noise in the network or differences in behavioural states (Renart and Machens, 2014), whereas drift is likely caused by cumulative processes, e.g. synaptic weight changes or changes in connectivity (Mongillo et al., 2017). Variability can be measured by comparing groups of stimulus presentations that are closely spaced in time, such as the even versus the odd trials across tens of repetitions in a given experiment. If variability is measured across trials that are not proximal in time then the mechanisms associated with drift can contribute to measured variability. Conversely, if response differences across days are measured, not all of the differences can be attributed to drift, because trial-to-trial variability will also contribute to the observed differences. Distilling out what proportion of stimulus response differences are attributable to drift can therefore only be done by comparing measured variability across different time intervals.

Several groups have published findings under a definition of drift that is far removed from the one above. These include publications that treat stimulus responses changes across different time interval lengths as equivalent and so do not distinguish between trial-to-trial variability and cumulative changes (Aitken et al., 2021), or focus on neuronal responses that are not linked to stimulus encoding, but rather to inferred connectivity motifs from noise-correlations (or ensembles; Pérez-Ortega et al., 2021). I will largely omit comparison of the findings in this thesis to such publications.

The first publication demonstrating representational drift in mouse V1 showed time dependent decay in the correlation of pairwise signal correlations (PSC; Montijn et al., 2016). This effect is also seen in this thesis (Figure 3.9c). Since then, several studies have reported cell-specific differences in tuning features across days, including stimulus size preference (Ranson, 2017), PO (Chen et al., 2013; Jeon et al., 2018) and orientation tuning width (Jeon et al., 2018). However,

quantifying the across day variability for a single time interval is not sufficient to unequivocally identify representational drift. One study (Rose et al., 2016) compared visual tuning parameter differences across several time intervals. Rose et al. found that PO, as well as ocular dominance and orientation selectivity changes, were not significantly different between 4 day versus 12-14 day intervals, suggesting that both of these tuning features were either stable beyond what could be explained by trial-to-trial variability, or that drift was saturated within 4 days. Taken together, these studies demonstrated representational drift on the level of tuning curve similarity, but also concluded that individual tuning properties do not show changes beyond day-to-day variability. This is not entirely plausible, because if tuning properties do not change, then what causes the decorrelation of signal correlations?

Based on the conclusion that representational drift is present in primary visual cortex and that tuning to basic visual features does not drift, recent publications have focused on five main questions: how widespread is drift in the visual processing pathway (very widespread: Deitch et al., 2021; Bauer and Rose, 2021), is drift larger for representations of some stimulus sets compared to others (yes: Marks and Goard, 2021; Deitch et al., 2021; see Bauer and Rose, 2021), is drift due to changes in stimulus tuning or responsiveness of neurons (both: Deitch et al., 2021; see Bauer and Rose, 2021), is drift parallel or orthogonal to stimulus coding dimensions (both: Xia et al., 2021; see also section 4.2.6), and is there a high dimensional population code that is stable despite changes of individual neurons (maybe: Deitch et al., 2021; Xia et al., 2021; see section 4.2.6)? As these questions have now largely been addressed, in this thesis I have addressed the question: what tuning features underly the decorrelation of tuning curves in response to both complex and simple stimuli?

I have focused on reassessing the variability and drift magnitude of one basic tuning feature, PO, and have shown that it undergoes representational drift. PO of neurons is on average ~3° (median) different on consecutive days and ~6° different when measured ~2 weeks apart (Figure 3.11f). If all of the changes that occur on a day-to-day basis were attributed to trial-to-trial variability, then on average ~3° of PO change is attributable to variability and ~3° to drift. Although the average magnitude of this effect is not large, individual neurons can undergo large significant changes in PO that cannot be explained by the trial-to-trial variability on individual days (Figure 3.11). This finding directly contradicts the previous study by Rose et al. (Rose et al., 2016). This discrepancy is likely due to higher trial numbers per stimulus, smaller angular intervals within the stimulus set and differences in the PO quantification method. These differences suggest an improved signal to noise ratio in the new dataset. This is supported by the substantially lower average PO change observed within 3-4 days (mean ~6°) compared to the previous study (mean ~13°; Rose et al., 2016). The increased signal to noise in the data presented in this thesis was therefore necessary in order to detect PO drift.

Collectively, recent publications have provided conclusive evidence that certain aspects of visual encoding in V1 and HVAs are not stable over time. This instability is not just due to trial-to-trial variability, but also caused by time dependent changes. These changes occur on the level of neuronal tuning as well as the population representation (Deitch et al., 2021). This thesis goes beyond these findings to identify one tuning property, PO, for which tuning drift can reliably be measured. Although PO is likely not the only visual tuning feature that undergoes drift, experiments and analysis in the future could aim to identify additional drifting features and compare their relative contribution to visual stimulus coding.

4.2.2 Effects of behaviour and repeated stimulus exposure on V1 tuning

There are several behavioural variables that can alter the encoding of visual stimuli in V1, such as running, pupil diameter, eye position and stimulus novelty. Before discussing the potential mechanism that control drift and the impact of continuous visual experience on stability, I will review the effects of behaviour and learning on the direction and orientation tuning of neurons in mouse V1. Experience can also shape the salience of specific stimuli and induce learning, for instance changes in stimulus novelty can affect the way in which V1 neurons respond to the same stimulus over time. It is therefore important to compare the PO drift in this thesis, to the neuronal tuning changes that occur due to behaviour and learning.

In my experiments, mice are head-fixed, in order to gain precise control over their visual input. However, mice are still able to move their eyes, which could confound measurements of visual tuning properties. Most relevant for the experiments in this thesis is eye torsion, which could directly affect PO. Previous studies have shown that under non-head-fixed conditions, mice show a host of complex eye movements. These include nonconjugate convergence and divergence of the eyes that change the binocular overlap, horizontal and vertical conjugate eye movements that stabilize and direct gaze (Meyer et al., 2020) and nonconjugate and conjugate torsional movements that compensate for head roll and pitch (Holmgren et al., 2021). However, under head-fixed conditions their eye movements are almost completely gone, except for some horizontal saccades associated with attempted head movement remaining (Mineault et al., 2016; Meyer et al., 2020). In particular, the complete lack of eye torsion means that eye movements are unlikely to cause the drift in PO observed in data presented in this thesis. Furthermore, the fact that neurons can shift in opposite directions across the same time interval (Figure 3.9b) also speaks against eye torsion as a cause. When experience of contours was restricted to those oriented at a specific angle, using cylinder lens goggles, the PO of neurons shifted in favour of this experienced orientation (Figure 3.13). This cannot be explained by eye movements because eye rotation would induce an apparent rotation across all POs rather than a convergence towards a specific orientation. Eye movements can therefore not explain either of the main findings.

Running and states of arousal can strongly influence the activity of neurons in the visual cortex (Niell and Stryker, 2010). During the experiments in this thesis, the mice were placed on spherical treadmills allowing them to walk or run forwards and backwards. Although this prevents the mice from moving in space, running in place still increases the firing rate of V1 neurons acting as a gain modulator (Niell and Stryker, 2010), with a slightly larger effect on high-spatial frequency tuned neurons (Mineault et al., 2016). States of arousal, usually inferred from pupil diameter, are also expected to fluctuate during awake recordings. Running and states of arousal can cause changes in some tuning features. These include an increase in temporal frequency preference (Andermann et al., 2011), orientation selectivity (Reimer et al., 2014) and receptive field size (Ayaz et al., 2013), as well as a decrease in surround suppression (Ayaz et al., 2013). Other tuning features, including spatial frequency preference and – importantly – PO, are unaffected (Mineault et al., 2016). However, because running and arousal act as a gain modulator on stimulus induced responses of neurons (Mineault et al., 2016), signal to noise ratio is affected, which in turn results in a decrease in the measurement accuracy of tuning features, including PO. If, for instance, arousal decreases over time it would result in an apparent drift of PO, merely because a decrease in signal to noise ratio would result in larger apparent PO differences. For this reason, I calculated bootstrapped confidence intervals of PO (Figure 3.11) and used these as significance thresholds. Because this applies a constant false positive threshold, it eliminates apparent drift caused by changes in signal to noise ratio alone. When selectively looking at just the significant PO changes, PO drift was still present (Figure 3.11e-f). Together, this argues against signal to noise ratio changes (i.e. due to running and arousal) causing the PO drift.

Stimulus specific associations to reward can also alter the apparent tuning of neurons to stimulus features. In one study (Poort et al., 2015), mice were trained to run down a corridor in virtual reality. After traveling down the corridor for a given distance they were randomly presented with either a rewarded (conditioned stimulus; CS+) or a non-rewarded stimulus (non-conditioned stimulus/ distractor; CS-). V1 neurons responsive to the CS+ before learning developed reward anticipation responses, i.e. they responded more strongly and for a longer time if their preferred stimulus was followed by licking and reward (also known as a hit). These same neurons also developed anticipatory activity when the mouse approached the position where either of the two stimuli would be presented, even though the mouse did not know which stimulus would occur. In the experiments in this thesis, stimuli are never paired with reward, so there is no reason why particular stimuli would increase in saliency over others and confound the neuronal tuning measures.

Novelty or familiarity, on the other hand, could affect the data by causing a change in activity depending on the familiarity across the stimulus set. Familiarity is known to cause an increase in activity when assessed using electrophysiological methods, but a decrease in calcium responses (Frenkel et al., 2006; Cooke and Bear, 2015; Makino and Komiyama, 2015). Both effects are

generally observed over the course of a few days of daily stimulus presentations and are stimulus specific. The source of this discrepancy between electrical and calcium activity is not known (Montgomery et al., 2022), but as stimulus tuning was assessed using two-photon calcium imaging in this thesis, a decay in stimulus specific responses could be expected in the data. In order to avoid confounders due to stimulus novelty, the animals were therefore presented with the full stimulus set on at least 2 days before the first tuning measurements were made. All stimuli are also presented the same number of times during each session so that no individual stimuli would appear more familiar. In the stripe rearing experiments, there is an overall increase in the number of neurons with POs close to the experienced orientation during deprivation (Figure 3.13b). Importantly, this effect is opposite to what would be expected from the effects of stimulus novelty.

Although arousal states, stimulus reward association and novelty have profound effects on the response amplitude of V1 neurons, they are not reported to change the basic tuning properties of individual neurons. In other words, a neuron does not have a different PO or receptive field positions depending on the context of location or stimulus novelty. These contexts provide additional information on top of the visual tuning properties of neurons, because they are specific to the context itself and can be viewed as additional tuning properties of neurons. It is therefore unlikely that the PO drift, or the PO convergence towards the experienced orientation during stripe rearing, can solely be explained through these potential confounds. However, this is rather a conceptual framework and has not been directly tested. On the other hand, there are other learning related changes that are known to directly influence the visual tuning properties of neurons outside of the relevant context.

4.2.3 What modulates drift speed?

In this thesis I show PO drift over the course of days and weeks, possibly due to the lack of anatomical constraints on the orientation preference of neurons (section 1.3), but the magnitude of this drift is relatively small (on average ~3° per day and ~6° over 2 weeks). Given the ongoing turnover of inputs onto V1 neurons under baseline conditions (~1.5% of dendritic spines lost and gain per day; Keck et al., 2008; Hofer et al., 2009), we may expect even larger PO drift. There are two theories that stand out. First, a small number of strong synaptic connections, not susceptible to turnover, provide a permanent "back-bone" of inputs, preventing a neuron from altering its tuning too much. Second, repeated activation of a network - by feed-forward or recurrent inputs - induces correlated activity between similarly tuned and connected neurons, repeatedly strengthening their connectivity through Hebbian processes, thus reinforcing existing correlation structures.

The idea of permanent dendritic spines and synapses as the locus of long-term information storage in the cortex, has a long history in neuroscience (Chang and Greenough, 1984; Bailey and Kandel, 1993; Engert and Bonhoeffer, 1999). I will refer to this as the synaptic trace theory. One argument in favour of this theory is that induction of experience-dependent plasticity happens faster when the animal has experienced the same intervention earlier in life, with spine gain only occurring during the first induction (Hofer et al., 2005; Hofer et al., 2009). This has been interpreted to mean, that for the first plasticity event new spines are required, but for the second event, the previously gained spines provide the "memory" of the first event and can be reused (Hofer et al., 2009). However, the synaptic trace theory has been questioned on the basis of the ongoing turnover of spines observed throughout the cortex (Mongillo et al., 2017). Nevertheless, the lack of PO drift previously observed (Rose et al., 2016), has also been hypothesized to be due to permanent "back-bone" spines (Clopath et al., 2017). Although we do find PO drift, its relatively small magnitude may be due to a small number of "back-bone" spines that prevent larger drift magnitudes. For instance, these spines may provide a PO set-point, around which small amounts of drift can still occur due to turnover of other inputs. Unfortunately, the tools to specifically remove spines that have been present for long periods of time or were formed during a specific plasticity or learning event are not available to test these hypotheses directly.

Repeated reactivation of circuits as a self-stabilizing mechanism in the brain is a more recent idea. The appeal of this theory is that it can easily be reconciled with the ongoing spine turnover observed throughout the cortex (Mongillo et al., 2017). A theoretical model has demonstrated the ability of spontaneous activity to maintain the connectivity of neuron pairs in a network (Fauth and

van Rossum, 2019). Interestingly, this model showed progressively fewer remaining synapses, but did not reach a point where all synapses were turned-over within the runtime of the model. It would have been interesting to remove this small fraction of pre-existing synapses to see if they played an important role for the tuning stability of the modelled neurons. Since any given neuron pair could connect via multiple synapses, it is possible that some of the synapses between a pair were stable over the runtime of the model, whereas others disappeared transiently. There is therefore no particular reason why the stable synapses would have contributed more to tuning stability than those that transiently disappeared. This model demonstrated stable ensemble coding of discrete sensory inputs, however, not all sensory features are discrete. How the representations of continues variables, such as PO, could be stably encoded was recently addressed in a different model by Rule and O'Leary (Rule and O'Leary, 2022). They found that the tuning stability of a readout population receiving input from an unstable but redundant input population, can be increased through a Hebbian homeostasis process. The readout population is initialized with similarly tuned input neurons being selectively connected. As the input population accumulates drift, the readout neurons no longer experience a large driving force due to the decorrelation of their inputs. This triggers Hebbian synaptic weight updates to strengthen inputs that correlate with the firing of the output neurons. The Hebbian homeostasis process was controlled via a correlation estimate between the input and output activity of the readout neuron, across the entire stimulus space. In terms of the brain, this could mean that the input network either has to be exposed to the full range of the stimulus space or simulate that exposure. Of course, these models only demonstrate the feasibility of recurrent and feedforward activity as a mechanism to stabilize neuronal tuning, under specific assumptions.

Recently, it has been shown that odours repeatedly experienced are represented more stably in the mouse piriform cortex than odours which are less frequently experienced (Schoonover et al., 2021). Although odours are likely represented discretely (Schoonover et al., 2021; Khona and Fiete, 2022), this provides empirical evidence that feed-forward activation through stimulus exposure could fulfil the role of maintaining functional representations through reactivation of specific connectivity networks. Whether this is a specific attribute of the olfactory cortex or a general principle across multiple sensory cortical areas has so far not been directly tested. In the visual cortex, every neuron is likely visually stimulated every day, inducing correlated activity through feed-forward reactivation with similarly tuned neurons. As a result, the neuronal population may naturally enter a stable state that best encodes the statistics of the visual environment it is exposed to, updating neuronal tuning only if the statistics of the visual environment change. To test this idea, the visual environment must be continuously and rigidly altered for the visual cortex to update the tuning of its neurons. In this thesis cylinder lens goggles were used to prevent the experience of all but one orientation, which resulted in the PO of V1 neurons slowly converging towards the remaining experienced orientation (Figure 3.14). However, if indeed visual experience stabilizes tuning, then neurons that are no longer exposed to contours aligned with their PO should show higher levels of PO drift compared to those with a PO aligned with the experienced orientation. I do not find this to be the case (Figure 3.15). This is somewhat surprising, since cumulative drift in the same direction, rather than in random directions, might be expected to result in higher overall measured drift. We therefore have two seemingly contradictory findings regarding the effect of experience on PO drift. Nonetheless, it appears that while experience is necessary to stabilize the representation of odours in olfactory cortex (Schoonover et al., 2021), a lack of experience of specific orientations does not dramatically destabilize the representation of those orientations in visual cortex. This is in line with a recent study in mouse V1 (Jeon et al., 2022) that found that preferred orientations appeared more stable over the course of 8 days of continues dark exposure, compared to the previous 8 days under normal conditions. The cause for this difference is entirely unclear and I can only speculate whether this difference is due to a difference in the neuronal substrate (different plasticity rules or circuit connectivity motifs) or a difference in the relationship between the stimuli being encoded (a single circular similarity relationship between stimuli as with contour orientations, and the more complex relationship between different odours). It would have been interesting if Rule and O'Leary (Rule and O'Leary, 2022) had assessed the effect of calculating the input output correlation across a restricted range of the continuous stimulus space in their model, simulating a restriction of the input feature. Would they have observed a change in

the direction of drift, as is the case in this thesis (Figure 3.14), or a stimulus specific change in drift magnitude, as I originally expected (Figure 3.15)?

4.2.4 Perceptual learning and its effects on visual tuning properties

During the stripe rearing paradigm used in this thesis, the distribution of V1 neuron POs shifts in favour of the experienced orientation. This results in an increase of the number of neurons that represent the experienced orientation and orientations close to it. This is reminiscent of some observations during perceptual learning, which refers to the improvement in a sensory detection or discrimination task (Li, 2016). During perceptual learning, neurons in the visual system can sometimes undergo tuning changes, which are thought to be crucial for the increase in perceptual abilities during this type of learning. Here, I will outline what is known about neuronal tuning changes during perceptual learning and compare these to the changes observed in this thesis.

Perceptual learning paradigms in animal experiments rely on learning of associations between stimuli and reward. In mice, it is not always easy to dissociate neuronal response and tuning changes associated with the learning of task parameters (e.g. lick when a stimulus is presented) from perceptual improvements (e.g. detecting stimulus A, or distinguishing stimulus A from B). For this reason, effects on stimulus representations associated with perceptual learning are typically assessed outside of the task context. In reward association learning paradigms, increases in stimulus selectivity (e.g. between vertical and vertical -40° gratings; Poort et al., 2015) are hard to separate into reward anticipation responses and tuning changes. Nevertheless, several studies have found interesting changes in V1 tuning when mice learned to distinguish stimuli from one another by presenting a larger range of stimuli out of task. Goltstein et al., (Goltstein et al., 2013) found that when mice learned to distinguish two orthogonally moving gratings in a paired conditioning task (e.g. gratings moving to the left were followed by a reward and gratings moving upwards were not), there were associated changes in the tuning distribution of V1 neurons measured under anaesthesia. Neurons with POs closer to the CS+ had higher direction selectivity and lower orientation selectivity compared with neurons whose PO aligned with the CS-. Another study assessed tuning changes in response to a similar task with orthogonal gratings for CS+ and CS-, but under head fixed conditions and using silicon probes (Jurjut et al., 2017). They likewise found a broadening of orientation tuning width for neurons that had POs close to the CS+, this time assessed in awake but out of task mice. Mouse V1 therefore undergoes modifications in its population distribution of tuning properties in response to task learning.

The tuning changes that occur in V1 neurons depend strongly on the task being learned and are specific to the stimulus features that are most informative for the task. For instance, when mice were trained to discriminate the retinotopic location of two identical drifting grating stimuli in a conditioning task, the spatial separation of the encoded stimuli in V1 increased. However, this only occurred for stimuli with the same grating orientation on which the mice were trained (Goltstein et al., 2018). In this particular task, the spatial location of the stimuli was the informative feature, but perceptual enhancement of this feature was specific to the type of stimulus on which the mouse was trained (gratings moving in a specific direction), and did not generalize to other features (gratings moving in other directions).

The results mentioned so far (Goltstein et al., 2013; Poort et al., 2015; Jurjut et al., 2017; Goltstein et al., 2018), did not track the change in neuronal tuning over the course of learning. It is therefore not possible to know from these data if neurons change their tuning or if the cause of these population changes is neurons that were previously unresponsive or untuned that become tuned to specific features. A recent study, in tree shrews, measured the tuning of individual neurons over the course of a stimulus discrimination paradigm, using two-photon calcium imaging (Schumacher et al., 2022). CS+ and CS- (static gratings) were initially separated by 45°, but this was reduced to 22.5° over time. The authors found that neurons with POs on one side of the CS+, the side that was further away from the CS-, altered multiple aspects of their visual responsiveness. These neurons increased their responsiveness overall, increased the asymmetry of their tuning curves toward the CS+ and shifted their PO toward the CS+. They also found that these changes were detrimental to the performance of discrimination between CS+ and a new CS- on the other side of the CS+ (i.e. From CS+ at 0 and CS- at 22.5° to CS+ at 0 and CS- at -22.5). These data indicate

that the type of tuning changes that occur in response to perceptual learning are highly specific to the task being learned, leave lasting changes measurable outside the context of the task, and can also have negative effects on perception in the context of a new task.

It is tempting to speculate that the PO changes observed over the course of stripe rearing are related to the neuronal changes observed during perceptual learning. PO drift converged when the visual environment was manipulated so that all but a few orientations were removed from the experience of the animal for several weeks. Grating presentations for 1 hour during imaging once a week prevented further convergence of PO beyond what was observed after the first week. A key question is whether PO convergence towards the experience orientation, was caused by either: passive feed-forward adaptation associated with an intrinsic mechanism of the visual system to adapt to the statistics of the sensory environment, or active engagement involving top-down feed-back (e.g. attention) and learning. On the one hand, the idea that the visual cortex develops a probabilistic representation of the visual environment through passive experience of the natural environment is not new and is integrated into some models of cognitive processes (Knoblich et al., 2002; Girshick et al., 2011; Li et al., 2022). However, this concept alludes to a passive feed-forward process in which the relevance of the features in the visual environment do not factor in. On the other hand, the expression of perceptual learning in humans seems to depend strongly on top-down mechanisms, such as attention to specific features (Choi and Watanabe, 2012; Li, 2016). During stripe rearing, the mice presumably continue to use vision to navigate within their home cage (though this was not systematically assessed). The alteration of the visual environment can therefore not be interpreted as engaging purely passive adaptation mechanisms of the early visual system, up to V1. It may be, that PO convergence is caused by perceptual learning during stripe rearing as the animal adapts to using a restricted range of visual features. Nevertheless, if the PO convergence was caused by top-down mechanisms controlled by attention (akin to perceptual learning), then I would not expect passive presentations of drifting gratings for ~1 hour every week to completely abolish further PO convergence (Figure 3.14g). However, the experiments in this thesis were not designed to differentiate between these two possible mechanisms. Future investigations could restrict vision to sessions in either open or closed loop virtual reality (while wearing cylinder lens goggles), to compare the effect of relevance and visuomotor coupling on PO convergence during stripe rearing.

Independent of the underlying cause, a pertinent question is whether the PO convergence we observed has consequences on sensory perception. As outlined above, perceptual learning is associated with changes in neuronal representations of relevant stimuli outside of the specific task context. Using stripe rearing we may be able to test if the converse is true. In other words, can we predict the perceptual improvements based on the changes in neuronal tuning we observe after stripe rearing. I would guess that this increase in the representation of the permitted orientation (Figure 3.13), through PO convergence (Figure 3.14), increases detection of low contrast contours aligned to the permitted orientation due to an overall activity gain to orientations around the permitted orientation. We did not find an accompanying increase in orientation and direction selectivity, around the permitted orientation, suggesting there may not be an accompanying increase in orientation discriminability around the permitted orientation. It would be interesting to test both predictions of the perceptual impact of the neuronal changes during stripe rearing in future experiments.

4.2.5 Cell-specific restoration of PO coding

Do neurons return to their original tuning, and does this tell us anything? After the cylinder lens goggles were removed, we waited 21 days before recording PO of V1 neurons a final time. We found that the distribution of POs returns to the pre-deprivation state (Figure 3.16). The negative correlation between the PO change during stripe rearing and during the recovery from stripe rearing indicates that this recovery happened in a cell-specific manner. This is reminiscent of what has previously been observed after recovery from MD (Rose et al., 2016). In that publication, it was suggested that this cell specific recovery may be due to a subset of synapses that are not eliminated during MD plasticity and allow individual neurons to regain their original function. It is conceivable that the observation of PO recovery is caused by such stable synapses. However, for both findings

there is an alternative explanation, namely, local input biases. Ocular dominance is organized in a salt-and-pepper manner in mouse V1, but it is not entirely clear how homogenous the ratio of ipsi- and contralaterally dominant dLGN projections are within binocular visual cortex. For instance, I would expect the ratio of ipsi- to contralateral thalamocortical axons to increases gradually within the binocular portion of V1; with the ratio favouring ipsilateral input in the ipsilateral portion of the binocular visual field and the ratio favouring contralateral input in the contralateral portion of the binocular visual field. Additionally, although ocular dominance columns are generally considered to be absent in mice, recent experiments have shown patch like organization of ocular dominance in mouse V1 (Goltstein et al., 2022). It may therefore be, that the post-MD cell specific recovery of ocular dominance reflects the local ratio of ipsi- and contralateral inputs available to these cells. Similarly, PO is also organized into a salt-and-pepper like fashion in mouse V1. However, biases in the distribution of PO have been reported to exist (bias toward horizontal orientations in monocular V1: Kreile et al., 2011; similar tuning for neurons within ~50 µm from one another: Ringach et al., 2016 and Tring et al., 2022; retinotopic dependent bias in PO across V1: Fahey et al., 2019). Furthermore, a similar correlation in PO drift during deprivation and recovery could arise from nonuniform distributions in intrinsic drift rate across neurons and an intrinsic property of the network to distribute stimulus representations across neurons. A neuron with a high intrinsic drift rate is thus pulled further toward the experienced orientation during deprivation than a stable neuron, but also drifts away from the then overrepresented orientation during recovery. It is therefore impossible to interpret the recovery of PO as evidence for either a synaptic trace, bias in the availability of inputs, or an inherent property of the circuit to self-organizing its representation of the sensory features being experienced.

4.2.6 Consequences of drift in V1

Consider an artificial neural network where the first stages comprise multiple convolutional layers followed by a fully connected layer that can encode the contents of the input image into a latent space. The network is then trained to recognise if the input image contains a face. In a superficial sense the network resembles a biological visual system, all be it oversimplified. But then the connection weights between the neurons are randomly shuffled one-by-one. The performance of the network at recognizing faces would progressively decline until it becomes completely useless. This is not what representational drift in the early visual system of the mouse looks like. Representational drift does not seem to have an increasingly negative impact on the ability of the brain to interpret and react to the visual environment, and there are a number of hypotheses why this might be.

I will outline four main hypotheses on how the negative consequences of representational drift could be mitigated. 1) The structural and functional changes that underly representational drift are irrelevant because they effect aspects of neuronal response properties that don't contribute to stimulus encoding. 2) A subpopulation of neurons remains stable and downstream areas ignore information from unstable neurons. 3) The way in which downstream areas read out information from the visual cortex is inherently agnostic to the changes that happen on the single cell level, because what matters is the stability of a population code, which does not drift. 4) Downstream areas compensate for the changes that occur in visual cortex by updating their connections accordingly.

The first hypothesis is that not all changes to the stimulus response properties of individual neuron are equally important to the stimulus representation by the neuronal population. Some changes might be detrimental to the information being encoded by V1 and some changes might be irrelevant. In other words, representational drift might be orthogonal to the coding dimensions relevant for downstream readout. The assessment of the orthogonality of trial-to-trial variability with respect to stimulus responses, is a common analysis approach to quantify the degree to which noise degrades information encoding (Panzeri et al., 2022). To this end, dimensionality reduction (e.g. through principle component analysis) followed by manifold fitting (fitting of a low dimensional structure in a high dimensional space) can be used. This can reveal a low dimensional shape that describes the representation of the stimulus set by the neural population. The direction of the variability is then quantified relative to this manifold. The angle of the noise relative to the manifold gives an estimate of whether the noise compromises the encoding of the stimulus or not.

This principle was used to look at day-to-day variability in mouse V1 by Xia et al., (Xia et al., 2021). The authors found that the ratio of noise perpendicular versus parallel to the manifold was greater across weeks than within weeks. Although, a comprehensive time-course of this shift in the relative angle of the noise was not determined, these data indicate that day-to-day noise is more damaging to the encoding of a variable for longer time intervals. These data suggest that at least part of the changes that happen due to representational drift are damaging to the encoding of the stimuli. Taken together, a portion of representational drift does appear to be parallel to stimulus representations, and thus in principle destructive, though it is unclear if these changes actually affect the readout of downstream neurons.

The second hypothesis is that drift is highly inhomogeneous across the neural population, and only information from the stable population is used by downstream areas. In this thesis I have shown that although the number of large changes increases as a function of time, there are many neurons that remain highly stable over long time intervals. Under this condition, the downstream areas could ignore the unstable populations and only connect to the stable populations, but this hypothesis lacks experimental evidence. On the other hand, even if a population of neurons shows highly stable PO tuning, it is not clear if they remain stable in their selectivity to other visual features (e.g. direction preference or receptive field shape). How a downstream area would integrate information from such a population, where each neuron might encode multiple features but only some that are stable over time, is not entirely clear. Although this hypothesis may be plausible for the visual system, with its relatively limited drift, for brain areas that are less stable, such as the hippocampus, PPC and olfactory cortex (Ziv et al., 2013; Driscoll et al., 2017; Schoonover et al., 2021), this seems unlikely. The hypothesis that only information from stable neuronal populations is utilized by downstream areas is therefore unlikely to be a general compensatory mechanism for representational drift across the brain.

The third hypothesis of how the consequences of drift could be mitigated in the brain is that single cell changes are inherently irrelevant to downstream areas. If downstream areas read out how the V1 population as a whole is responding to visual stimuli, there might be circumstances in which single cell changes are inconsequential. In the artificial neural network analogy, there may be countless configurations of the network that result in similar performance outcomes, at least for a given set of stimuli. If drift is restricted to transitions between these equivalent states then there is no impact on the performance of the network. Deitch et al., (Deitch et al., 2021) calculated the internal structure of neuronal responses in V1, and other visual areas, to the presentation of a short movie sequence. This internal structure essentially describes the distribution of tuning curves across neurons (Bauer and Rose, 2021). Inherent to this metric is the fact that shuffling neuronal identity, independently for each day, has no effect on the internal structure compared across days. Internal structure can therefore be completely stable across days, especially if a large number of cells across many mice are included in the calculation, as long as drift does not alter the statistics of tuning. This is because, at the population level, drift in the tuning of one cell is compensated for by another. So far, however, there is no theory, that could tell us how the internal structure can be read out and used by downstream areas. A problem I see with the internal structure metric in general, is that it is not designed for generalization to other stimuli. Given an internal structure, it is hard, if not impossible, to predict the response of the neural population to a different random natural image, or how the single cell drift in the neuronal population would affect the encoding of this new image.

The fourth hypothesized mechanism is that representational drift is compensated for by synaptic updates in the connections to a downstream readout population. This can be modelled using neuronal ensembles to connect a group of input neurons to a group of output neurons. Ensembles are inherently stable over time even if the members of those ensembles are shuffled and replaced. But changes in the members of the ensembles must be compensated for in order for the ensemble to continuously provide the link between a group of input neurons and a group of output neurons. This can be achieved using simple spike timing dependent plasticity rules (Kossio et al., 2021; see also Fauth and van Rossum, 2019). However, the current models of drifting ensembles represent discrete variables and do not generalize to continuous variables. In a set of alternative models, presented by Rule and O'Leary (Rule and O'Leary, 2022), the stability of a downstream readout of a continuous variable can be increased using Hebbian homeostatic weight updates

(Hebbian plasticity rules that are modulated by the deviation from an activity setpoint) and made almost completely stable with recurrent feedback. Applying multiple of these compensatory models in sequence would probably results in increasingly stable representations, but this does not seem to be the case, at least not across the hierarchy of the visual system (Deitch et al., 2021). In general, however, compensatory synaptic weight update could mitigate the effects of representational drift, under somewhat biologically plausible assumptions.

In summary, the results presented in this thesis, as well as previous publications (Xia et al., 2021), suggest the first hypothesis is not true. PO drift is by its nature not orthogonal to the coding direction, because PO is a coding dimension. The idea that downstream areas may simply ignore information from unstable neurons (second hypothesis), may be plausible in the visual system, but is unfeasible as a general drift compensation mechanism across the brain. With regard to a stable population code (third hypothesis), if data is pooled across many animals, drift does not appear to alter the internal structure in the absence of perturbations or learning (Deitch et al., 2021). Although the hypothesis that downstream areas are able to compensate for representational drift through ongoing synaptic weight update is largely theoretical (fourth hypothesis), I consider it to be the most likely and generalizable mechanism across the brain.

4.2.7 Summary and outlook

Representational drift is now a well-established phenomenon in the mouse visual cortex, with several studies demonstrating its existence and measuring its dynamics (e.g. Montijn et al., 2016; Deitch et al., 2021; Xia et al., 2021). The results in this thesis contribute to this field, by for the first time identifying a visual tuning feature that undergoes time dependent representational drift, preferred orientation (PO). The magnitude of PO drift is small, which likely explains why previous studies have not observed it (Rose et al., 2016). In olfactory cortex, frequent experience of odours stabilizes their representation (Schoonover et al., 2021). In visual cortex, visual features are experienced almost daily, which may explain why they show such limited drift. We investigate the hypothesis that continuous experience of visual features limits the magnitude of this PO drift by chronically restricting the range of orientations mice are exposed to. We replicated the redistribution of orientation preference observed in a previous study (Kreile et al., 2011) and discovered that this is largely due to cells changing their PO in favour of the remaining experienced orientation. We found that this convergence is time dependent, but that the brief exposure to drifting gratings during the interleaved imaging sessions prevented any further convergence of PO compared to mice that experienced continuous deprivation for an equal amount of time. This argues in favour of PO drift being experience dependent. However, we did not find that the drift rate of PO was related to the initial distance of a neurons PO to the experienced orientation, arguing against the hypothesis that continuous experience of visual features is necessary for their stable representation in V1. Taken together, I would conclude that experience does not stabilize the tuning of neurons, but that overall the population will start to overrepresent a subspace of a visual feature if only exposed to that subspace for an extended period of time.

There are a number of additional experiments which would be exciting to follow up on in light of the data presented in this thesis. First, it would be interesting to test to what degree the psychometrics of orientation perception are affected by stripe rearing using contrast sensitivity and orientation discrimination tasks. Second, it is likely that altering the excitation inhibition balance, can change the rate of representational drift as it would affect the correlation structure of spontaneous activity, which is speculated to stabilize sensory representations (Fauth and van Rossum, 2019). Third, quantifying the time course of drift for other features (such as spatial frequency, temporal frequency, receptive field location etc.) would allow us to integrate these dynamics into computational models of the visual system in order to test if these models are robust to representational drift.

Bibliography

Aitken, K., Garrett, M., Olsen, S., & Mihalas, S. (2021). The geometry of representational drift in natural and artificial neural networks. *18*(11), e1010716.

Almeida, I., Soares, S. C., & Castelo-Branco, M. (2015). The distinct role of the amygdala, superior colliculus and pulvinar in processing of central and peripheral snakes. *PLoS ONE*, *10*(6), e0129949.

Andermann, M. L., Kerlin, A. M., Roumis, D. K., Glickfeld, L. L., & Reid, R. C. (2011). Functional specialization of mouse higher visual cortical areas. *Neuron*, *72*(6), 1025–1039.

Antonini, A., Fagiolini, M., & Stryker, M. P. (1999). Anatomical correlates of functional plasticity in mouse visual cortex. *Journal of Neuroscience*, *19*(11), 4388–4406.

Antonini, A., & Stryker, M. P. (1993). Rapid remodeling of axonal arbors in the visual cortex. *Science*, *260*(5115), 1819–1821.

Antonini, A., & Stryker, M. P. (1996). Plasticity of geniculocortical afferents following brief or prolonged monocular occlusion in the cat. *Journal of Comparative Neurology*, *369*(1), 64–82.

Aschauer, D. F., Eppler, J.-B., Ewig, L., Chambers, A. R., Pokorny, C., Kaschube, M., & Rumpel, S. (2022). Learning-induced biases in the ongoing dynamics of sensory representations predict stimulus generalization. *Cell Reports*, *38*(6), 110340.

Assali, A., Gaspar, P., & Rebsam, A. (2014). Activity dependent mechanisms of visual map formation - From retinal waves to molecular regulators. *Seminars in Cell & Developmental Biology*, *35*, 136–146.

Attardo, A., Fitzgerald, J. E., & Schnitzer, M. J. (2015). Impermanence of dendritic spines in live adult CA1 hippocampus. *Nature*, *523*(7562), 592–596.

Ayaz, A., Saleem, A. B., Schölvinck, M. L., & Carandini, M. (2013). Locomotion controls spatial integration in mouse visual cortex. *Current Biology*, *23*(10), 890–894.

Baden, T., Berens, P., Franke, K., Rosón, M. R., Bethge, M., & Euler, T. (2016). The functional diversity of retinal ganglion cells in the mouse. *Nature*, *529*(7586), 345–350.

Bailey, C. H., & Kandel, E. R. (1993). Structural changes accompanying memory storage. *Annual Review of Physiology*, *55*(1), 397–426.

Bakken, T. E., van Velthoven, C. T., Menon, V., Hodge, R. D., Yao, Z., Nguyen, T. N., Graybuck, L. T., Horwitz, G. D., Bertagnolli, D., Goldy, J., Yanny, A. M., Garren, E., Parry, S., Casper, T., Shehata, S. I., Barkan, E. R., Szafer, A., Levi, B. P., Dee, N., ... Tasic, B. (2021). Single-cell and single-nucleus RNA-seq uncovers shared and distinct axes of variation in dorsal LGN neurons in mice, non-human primates, and humans. *eLife*, *10*, e64875.

Barlow, H. B., Hill, R. M., & Levick, W. R. (1964). Retinal ganglion cells responding selectively to direction and speed of image motion in the rabbit. *Journal of Physiology*, *173*(3), 377–407.

Barlow, H. B., & Hill, R. M. (1963). Selective sensitivity to direction of movement in ganglion cells of the rabbit retina. *Science*, *139*(3553), 412–414.

Bauer, J., & Rose, T. (2021). Mouse vision: Variability and stability across the visual processing hierarchy. *Current Biology*, *31*(19), R1129–R1132.

Bauer, J., Weiler, S., Fernholz, M. H., Laubender, D., Scheuss, V., Hübener, M., Bonhoeffer, T., & Rose, T. (2021). Limited functional convergence of eye-specific inputs in the retinogeniculate pathway of the mouse. *Neuron*, *109*(15), 2457–2468.

Beltramo, R., & Scanziani, M. (2019). A collicular visual cortex: Neocortical space for an ancient midbrain visual structure. *Science*, *363*(6422), 64–69.

Bennett, C., Gale, S. D., Garrett, M. E., Newton, M. L., Callaway, E. M., Murphy, G. J., & Olsen, S. R. (2019). Higher-order thalamic circuits channel parallel streams of visual information in mice. *Neuron*, *102*(2), 477–492.

Berens, P. (2009). CircStat : a MATLAB toolbox for circular statistics. *Journal of Statistical Software*, *31*(10), 1–21.

Bickford, M. E., Zhou, N., Krahe, T. E., Govindaiah, G., & Guido, W. (2015). Retinal and tectal "driver-Like" inputs converge in the shell of the mouse dorsal lateral geniculate nucleus. *Journal of Neuroscience*, *35*(29), 10523–10534.

Bishop, P. O., Kozak, W., Levick, W. R., & Vakkur, G. J. (1962). The determination of the projection of the visual field on to the lateral geniculate nucleus in the cat. *Journal of Physiology*, *163*(3), 503–539.

Blakemore, C., & Cooper, G. F. (1970). Development of the brain depends on the visual environment. *Nature*, *228*(5270), 477–478.

Bliss, T. V. P., & Collingridge, G. L. (1993). A synaptic model of memory: long-term potentiation in the hippocampus. *Nature*, *361*(6407), 31–39.

Bonhoeffer, T., & Grinvald, A. (1991). Iso-orientation domains in cat visual cortex are arranged in pinwheel-like patterns. *Nature*, *353*(6343), 429–431.

Boone, H. C., Samonds, J. M., Crouse, E. C., Barr, C., Priebe, N. J., & McGee, A. W. (2021). Natural binocular depth discrimination behavior In mice explained by visual cortical activity. *Current Biology*, *31*(10), 2191–2198.

Brainard, D. H. (1997). The Psychophysics Toolbox. *Spatial Vision*, *10*(4), 433–436.

Butz, M., Wörgötter, F., & Ooyen, A. v. (2009). Activity-dependent structural plasticity. *Brain Research Reviews*, *60*(2), 287–305.

Buzás, P., Eysel, U. T., Adorján, P., & Kisvárday, Z. F. (2001). Axonal topography of cortical basket cells in relation to orientation, direction, and ocular dominance maps. *Journal of Comparative Neurology*, *437*(3), 259–285.

Buzás, P., Kovács, K., Ferecskó, A. S., Budd, J. M., Eysel, U. T., & Kisvárday, Z. F. (2006). Model-based analysis of excitatory lateral connections in the visual cortex. *Journal of Comparative Neurology*, *499*(6), 861–881.

Cai, D., Cohen, K. B., Luo, T., Lichtman, J. W., & Sanes, J. R. (2013). Improved tools for the Brainbow toolbox. *Nature Methods*, *10*(6), 540–547.

Callaway, E. M., & Luo, L. (2015). Monosynaptic circuit tracing with glycoprotein-deleted rabies viruses. *Journal of Neuroscience*, *35*(24), 8979–8985.

Canfield, J. G. (2006). Dry beveling micropipettes using a computer hard drive. *Journal of Neuroscience Methods*, *158*(1), 19–21.

Cang, J., Kaneko, M., Yamada, J., Woods, G., Stryker, M. P., & Feldheim, D. A. (2005). Ephrin-As guide the formation of functional maps in the visual cortex. *Neuron*, *48*(4), 577–589.

Cang, J., Rentería, R. C., Kaneko, M., Liu, X., Copenhagen, D. R., & Stryker, M. P. (2005). Development of precise maps in visual cortex requires patterned spontaneous activity in the retina. *Neuron*, *48*(5), 797–809.

Chalupa, L. M., & Williams., R. W. (Eds.). (2008). *Eye, retina, and visual system of the mouse*. MIT press.

Chang, F.-L. F., & Greenough, W. T. (1984). Transient and enduring morphological correlates of synaptic activity and efficacy change in the rat hippocampal slice. *Brain Research*, *309*(1), 35–46.

Chapman, B., Stryker, M. P., & Bonhoeffer, T. (1996). Development of orientation preference maps in ferret primary visual cortex. *Journal of Neuroscience*, *16*(20), 6443–6453.

Chen, C., & Regehr, W. G. (2000). Developmental remodeling of the retinogeniculate synapse. *Neuron*, *28*(3), 955–966.

Chen, S.-K., Badea, T. C., & Hattar, S. (2011). Photoentrainment and pupillary light reflex are mediated by distinct populations of ipRGCs. *Nature*, *476*(7358), 92–95.

Chen, T.-W., Wardill, T. J., Sun, Y., Pulver, S. R., Renninger, S. L., Baohan, A., Schreiter, E. R., Kerr, R. A., Orger, M. B., Jayaraman, V., Looger, L. L., Svoboda, K., & Kim, D. S.

(2013). Ultrasensitive fluorescent proteins for imaging neuronal activity. *Nature*, *499*(7458), 295–300.

Cheng, S., Butrus, S., Tan, L., Xu, R., Sagireddy, S., Trachtenberg, J. T., Shekhar, K., & Zipursky, S. L. (2022). Vision-dependent specification of cell types and function in the developing cortex. *Cell*, *185*(2), 311–327.

Choi, H., & Watanabe, T. (2012). Perceptual learning solely induced by feedback. *Vision Research*, *61*, 77–82.

Clopath, C., Bonhoeffer, T., Hübener, M., & Rose, T. (2017). Variance and invariance of neuronal long-term representations. *Philosophical Transactions of the Royal Society of London. B, Biological Sciences*, *372*(1715), 20160161.

Coleman, J., Law, K., & Bear, M. (2009). Anatomical origins of ocular dominance in mouse primary visual cortex. *Neuroscience*, *161*(2), 561–571.

Collingridge, G. L., Kehl, S. J., & McLennan, H. (1984). The action of some analogues of the excitatory amino acids in the dentate gyrus of the rat. *Canadian Journal of Physiology and Pharmacology*, *62*(4), 424–429.

Cooke, S. F., & Bear, M. F. (2015). Visual recognition memory: a view from V1. *Current Opinion in Neurobiology*, *35*, 57–65.

Cruz-Martín, A., El-Danaf, R. N., Osakada, F., Sriram, B., Dhande, O. S., Nguyen, P. L., Callaway, E. M., Ghosh, A., & Huberman, A. D. (2014). A dedicated circuit linking direction selective retinal ganglion cells to primary visual cortex. *Nature*, *507*(7492), 358–361.

Cuntz, H., Forstner, F., Borst, A., & Häusser, M. (2010). One rule to grow them all: A general theory of neuronal branching and its practical application. *PLoS Computational Biology*, *6*(8), e1000877.

Daniel, P. M., & Whitteridge, D. (1961). The representation of the visual field on the cerebral cortex in monkeys. *Journal of Physiology*, *159*(2), 203–221.

Darian-Smith, C., & Gilbert, C. (1995). Topographic reorganization in the striate cortex of the adult cat and monkey is cortically mediated. *Journal of Neuroscience*, *15*(3), 1631–1647.

Deitch, D., Rubin, A., & Ziv, Y. (2021). Representational drift in the mouse visual cortex. *Current Biology*, *31*(19), 4327–4339.

Denk, W., Strickler, J. H., & Webb, W. W. (1990). Two-photon laser scanning fluorescence microscopy. *Science*, *248*(4951), 73–76.

Dräger, U. C. (1978). Observations on monocular deprivation in mice. *Journal of Neurophysiology*, *41*(1), 28–42.

Dräger, U. C. (1974). Autoradiography of tritiated proline and fucose transported transneuronally from the eye to the visual cortex in pigmented and albino mice. *Brain Research*, *82*(2), 284–292.

Dräger, U. C. (1975). Receptive fields of single cells and topography in mouse visual cortex. *Journal of Comparative Neurology*, *160*(3), 269–289.

Dräger, U. C., & Olsen, J. F. (1980). Origins of crossed and uncrossed retinal projections in pigmented and albino mice. *Journal of Comparative Neurology*, *191*(3), 383–412.

Driscoll, L. N., Pettit, N. L., Minderer, M., Chettih, S. N., & Harvey, C. D. (2017). Dynamic reorganization of neuronal activity patterns in parietal cortex. *Cell*, *170*(5), 986–999.

Ellis, E. M., Gauvain, G., Sivyer, B., & Murphy, G. J. (2016). Shared and distinct retinal input to the mouse superior colliculus and dorsal lateral geniculate nucleus. *Journal of Neurophysiology*, *116*(2), 602–610.

Engert, F., & Bonhoeffer, T. (1999). Dendritic spine changes associated with hippocampal long-term synaptic plasticity. *Nature*, *399*(6731), 66–70.

Espinosa, J. S., & Stryker, M. P. (2012). Development and plasticity of the primary visual cortex. *Neuron*, *75*(2), 230–249.

Evangelio, M., García-Amado, M., & Clascá, F. (2018). Thalamocortical projection neuron and interneuron numbers in the visual thalamic nuclei of the adult C57BL/6 mouse. *Frontiers in Neuroanatomy*, *12*, 27.

Fahey, P. G., Muhammad, T., Smith, C., Froudarakis, E., Cobos, E., Fu, J., Walker, E. Y., Yatsenko, D., Sinz, F. H., Reimer, J., & Tolias, A. S. (2019). A global map of orientation tuning in mouse visual cortex. *bioRxiv*, 745323.

Fauth, M. J., & van Rossum, M. C. (2019). Self-organized reactivation maintains and reinforces memories despite synaptic turnover. *eLife*, *8*, e43717.

Finlay, B. L., Franco, E. C. S., Yamada, E. S., Crowley, J. C., Parsons, M., Muniz, J. A. P., & Silveira, L. C. L. (2008). Number and topography of cones, rods and optic nerve axons in New and Old World primates. *25*(3), 289–299.

Frenkel, M. Y., Sawtell, N. B., Diogo, A. C. M., Yoon, B., Neve, R. L., & Bear, M. F. (2006). Instructive effect of visual experience in mouse visual cortex. *Neuron*, *51*(3), 339–349.

Gale, S. D., & Murphy, G. J. (2014). Distinct representation and distribution of visual information by specific Cell types in mouse superficial superior colliculus. *Journal of Neuroscience*, *34*(40), 13458–13471.

Gilbert, C. D. (1983). Microcircuitry of the visual cortex. *Annual Review of Neuroscience*, *6*(1), 217–247.

Gilbert, C. D., & Wiesel, T. N. (1989). Columnar specificity of intrinsic horizontal and corticocortical connections in cat visual cortex. *Journal of Neuroscience*, *9*(7), 2432–2442.

Gilbert, C. D., & Wiesel, T. N. (1992). Receptive field dynamics in adult primary visual cortex. *Nature*, *356*(6365), 150–152.

Girshick, A. R., Landy, M. S., & Simoncelli, E. P. (2011). Cardinal rules: Visual orientation perception reflects knowledge of environmental statistics. *Nature Neuroscience*, *14*(7), 926–932.

Godement, P., Salaün, J., & Imbert, M. (1984). Prenatal and postnatal development of retinogeniculate and retinocollicular projections in the mouse. *Journal of Comparative Neurology*, *230*(4), 552–575.

Goltstein, P. M., Coffey, E. B. J., Roelfsema, P. R., & Pennartz, C. M. A. (2013). In vivo two-photon Ca2+ Imaging reveals selective reward effects on stimulus-specific assemblies in mouse visual cortex. *Journal of Neuroscience*, *33*(28), 11540–11555.

Goltstein, P. M., Laubender, D., Bonhoeffer, T., & Hübener, M. (2022). Ocular dominance columns in mouse visual cortex [Program No. 546.05. 2021 Neuroscience Meeting Planner].

Goltstein, P. M., Meijer, G. T., & Pennartz, C. M. (2018). Conditioning sharpens the spatial representation of rewarded stimuli in mouse primary visual cortex. *eLife*, *7*, e37683.

Goltstein, P. M., Reinert, S., Bonhoeffer, T., & Hübener, M. (2021). Mouse visual cortex areas represent perceptual and semantic features of learned visual categories. *Nature Neuroscience*, *24*(10), 1441–1451.

Goodale, M. A., & Milner, A. (1992). Separate visual pathways for perception and action. *Trends in Neurosciences*, *15*(1), 20–25.

Gordon, J. A., & Stryker, M. P. (1996). Experience-dependent plasticity of binocular responses in the primary visual cortex of the mouse. *Journal of Neuroscience*, *16*(10), 3274–3286.

Greifzu, F., Pielecka-Fortuna, J., Kalogeraki, E., Krempler, K., Favaro, P. D., Schlüter, O. M., & Löwel, S. (2014). Environmental enrichment extends ocular dominance plasticity into adulthood and protects from stroke-induced impairments of plasticity. *Proceedings of the National Academy of Sciences*, *111*(3), 1150–1155.

Grieve, K. L. (2005). Binocular visual responses in cells of the rat dLGN. *Journal of Physiology*, *566*(1), 119–124.

Grubb, M. S., & Thompson, I. D. (2003). Quantitative characterization of visual response properties in the mouse dorsal lateral geniculate nucleus. *Journal of Neurophysiology*, *90*(6), 3594–3607.

Grubb, M. S., & Thompson, I. D. (2004). Biochemical and anatomical subdivision of the dorsal lateral geniculate nucleus in normal mice and in mice lacking the β2 subunit of the nicotinic acetylcholine receptor. *Vision Research*, *44*(28), 3365–3376.

Grünert, U., & Martin, P. R. (2020). Cell types and cell circuits in primate retina. *Progress in Retinal and Eye Research*, *78*, 100844.

Guillery, R. W. (1995). *The Optic Chiasm of the Vertebrate Brain* (Vol. 7).

Guillery, R. W., & Stelzner, D. J. (1970). The differential effects of unilateral lid closure upon the monocular and binocular segments of the dorsal lateral geniculate nucleus in the cat. *Journal of Comparative Neurology*, *139*(4), 413–421.

Hammer, S., Monavarfeshani, A., Lemon, T., Su, J., & Fox, M. A. (2015). Multiple retinal axons converge onto relay cells in the adult mouse thalamus. *Cell Reports*, *12*(10), 1575–1583.

Hamos, J. E., Horn, S. C. V., Raczkowski, D., & Sherman, S. M. (1987). Synaptic circuits involving an individual retinogeniculate axon in the cat. *Journal of Comparative Neurology*, *259*(2), 165–192.

Han, X., Vermaercke, B., & Bonin, V. (2022). Diversity of spatiotemporal coding reveals specialized visual processing streams in the mouse cortex. *Nature Communications*, *13*(1), 1–18.

Hartigan, J. A., & Hartigan, P. M. (1985). The dip test of unimodality. *The Annals of Statistics*, 70–84.

Hensch, T. K. (2005). Critical period plasticity in local cortical circuits. *Nature Reviews Neuroscience*, *6*(11), 877–888.

Hirsch, H. V. B., & Spinelli, D. N. (1970). Visual experience modifies distribution of horizontally and vertically oriented receptive fields in cats. *Science*, *168*(3933), 869–871.

Hofer, S. B., Mrsic-Flogel, T. D., Bonhoeffer, T., & Hübener, M. (2005). Prior experience enhances plasticity in adult visual cortex. *Nature Neuroscience*, *9*(1), 127–132.

Hofer, S. B., Mrsic-Flogel, T. D., Bonhoeffer, T., & Hübener, M. (2009). Experience leaves a lasting structural trace in cortical circuits. *Nature*, *457*(7227), 313–317.

Holmgren, C. D., Stahr, P., Wallace, D. J., Voit, K.-M., Matheson, E. J., Sawinski, J., Bassetto, G., & Kerr, J. N. (2021). Visual pursuit behavior in mice maintains the pursued prey on the retinal region with least optic flow. *eLife*, *10*, e70838.

Hooks, B. M., Lin, J. Y., Guo, C., & Svoboda, K. (2015). Dual-channel circuit mapping reveals sensorimotor sonvergence in the primary motor cortex. *Journal of Neuroscience*, *35*(10), 4418–4426.

Hooks, B. M., & Chen, C. (2006). Distinct roles for spontaneous and visual activity in remodeling of the retinogeniculate rynapse. *Neuron*, *52*(2), 281–291.

Hooks, B. M., & Chen, C. (2008). Vision triggers an experience-dependent sensitive period at the retinogeniculate synapse. *Journal of Neuroscience*, *28*(18), 4807–4817.

Horton, J. C., Greenwood, M. M., & Hubel, D. H. (1979). Non-retinotopic arrangement of fibres in cat optic nerve. *Nature*, *282*(5740), 720–722.

Howarth, M., Walmsley, L., & Brown, T. M. (2014). Binocular integration in the mouse lateral geniculate nuclei. *Current Biology*, *24*(11), 1241–1247.

Hoy, J. L., Bishop, H. I., & Niell, C. M. (2019). Defined Cell Types in Superior Colliculus Make Distinct Contributions to Prey Capture Behavior in the Mouse. *Current Biology*, *29*(23), 4130–4138.

Hubel, D. H., & Wiesel, T. N. (1959). Receptive fields of single neurones in the cat's striate cortex. *Journal of Physiology*, *148*(3), 574–591.

Hubel, D. H., & Wiesel, T. N. (1962). Receptive fields, binocular interaction and functional architecture in the cat's visual cortex. *Journal of Physiology*, *160*(1), 106–154.

Hubel, D. H., & Wiesel, T. N. (1972). Laminar and columnar distribution of geniculo-cortical fibers in the macaque monkey. *Journal of Comparative Neurology*, *146*(4), 421–450.

Hubel, D. H., & Wiesel, T. N. (1974). Sequence regularity and geometry of orientation columns in the monkey striate cortex. *Journal of Comparative Neurology*, *158*(3), 267–293.

Hubel, D. H., Wiesel, T. N., & LeVay, S. (1977). Plasticity of ocular dominance columns in monkey striate cortex. *Philosophical Transactions of the Royal Society of London. B, Biological Sciences*, *278*(961), 377–409.

Huberman, A. D., Manu, M., Koch, S. M., Susman, M. W., Lutz, A. B., Ullian, E. M., Baccus, S. A., & Barres, B. A. (2008). Architecture and activity-mediated refinement of axonal projections from a mosaic of genetically identified retinal ganglion Cells. *Neuron*, *59*(3), 425–438.

Huberman, A. D., Wei, W., Elstrott, J., Stafford, B. K., Feller, M. B., & Barres, B. A. (2009). Genetic identification of an on-off direction- selective retinal ganglion cell subtype reveals a layer-specific subcortical map of posterior motion. *Neuron*, *62*(3), 327–334.

Huh, C. Y. L., Abdelaal, K., Salinas, K. J., Gu, D., Zeitoun, J., Velez, D. X. F., Peach, J. P., Fowlkes, C. C., & Gandhi, S. P. (2020). long-term monocular deprivation during juvenile critical

period disrupts binocular integration in mouse visual thalamus. *Journal of Neuroscience*, *40*(3), 585–604.

Illing, R.-B., & Wässle, H. (1981). The retinal projection to the thalamus in the cat: A quantitative investigation and a comparison with the retinotectal pathway. *Journal of Comparative Neurology*, *202*(2), 265–285.

Isa, T., Marquez-Legorreta, E., Grillner, S., & Scott, E. K. (2021). The tectum/superior colliculus as the vertebrate solution for spatial sensory integration and action. *Current Biology*, *31*(11), R741–R762.

Isaac, J. T., Nicoll, R. A., & Malenka, R. C. (1995). Evidence for silent synapses: Implications for the expression of LTP. *Neuron*, *15*(2), 427–434.

Jaepel, J., Hübener, M., Bonhoeffer, T., & Rose, T. (2017). Lateral geniculate neurons projecting to primary visual cortex show ocular dominance plasticity in adult mice. *Nature Neuroscience*, *20*(12), 1708–1714.

Jang, J., Song, M., & Paik, S.-B. (2020). retino-cortical mapping ratio predicts columnar and salt-and-pepper organization in mammalian visual cortex. *Cell Reports*, *30*(10), 3270–3279.

Jaubert-Miazza, L., Green, E., Lo, F.-S., Bui, K., Mills, J., & Guido, W. (2005). Structural and functional composition of the developing retinogeniculate pathway in the mouse. *Visual Neuroscience*, *22*(5), 661–676.

Jeffery, G. (1985). Retinotopic order appears before ocular separation in developing visual pathways. *Nature*, *313*(6003), 575–576.

Jeon, B. B., Fuchs, T., Chase, S. M., & Kuhlman, S. J. (2022). Visual experience has opposing influences on the quality of stimulus representation in adult primary visual cortex. *eLife*, *11*, e80361.

Jeon, B. B., Swain, A. D., Good, J. T., Chase, S. M., & Kuhlman, S. J. (2018). Feature selectivity is stable in primary visual cortex across a range of spatial frequencies. *Scientific Reports*, *8*(1), 1–14.

Jeon, C.-J., Strettoi, E., & Masland, R. H. (1998). The major cell populations of the mouse retina. *Journal of Neuroscience*, *18*(21), 8936–8946.

Jiang, Q., Litvina, E. Y., Ledesma, H. A., Shu, G., Sonoda, T., Wei, W., & Chen, C. (2022). Functional convergence of on-off direction-selective ganglion cells in the visual thalamus. *Current Biology*, *32*(14), 3110–3120.

Jin, J., Wang, Y., Swadlow, H. A., & Alonso, J. M. (2011). Population receptive fields of ON and OFF thalamic inputs to an orientation column in visual cortex. *Nature Neuroscience*, *14*(2), 232–238.

Jin, M., & Glickfeld, L. L. (2020). Mouse higher visual areas provide both distributed and specialized contributions to visually guided behaviors. *Current Biology*, *30*(23), 4682–4692.

Jurjut, O., Georgieva, P., Busse, L., & Katzner, S. (2017). Learning enhances sensory processing in mouse V1 before improving behavior. *Journal of Neuroscience*, *37*(27), 6460–6474.

Kaas, J. H., & Baldwin, M. K. L. (2019). The evolution of the pulvinar complex in primates and its role in the dorsal and ventral streams of cortical processing. *Vision*, *4*(1), 3.

Kaas, J. H., Qi, H.-X., & Stepniewska, I. (2021). Escaping the nocturnal bottleneck, and the evolution of the dorsal and ventral streams of visual processing in primates. *Philosophical Transactions of the Royal Society B*, *377*(1844), 1–17.

Kalatsky, V. A., & Stryker, M. P. (2003). New paradigm for optical imaging temporally encoded maps of intrinsic signal. *Neuron*, *38*(4), 529–545.

Kalish, B. T., Cheadle, L., Hrvatin, S., Nagy, M. A., Rivera, S., Crow, M., Gillis, J., Kirchner, R., & Greenberg, M. E. (2018). Single-cell transcriptomics of the developing lateral geniculate nucleus reveals insights into circuit assembly and refinement. *Proceedings of the National Academy of Sciences*, *115*(5), E1051–E1060.

Kandel, E. R., Koester, J. D., Mack, S. H., Siegelbaum, S. A., Marder, E., & Clapham, D. E. (Eds.). (2021). *Principles of Neural Science* (Sixth Edition). McGraw-Hill.

Katz, L. C., Gilbert, C. D., & Wiesel, T. N. (1989). Local circuits and ocular dominance columns in monkey striate cortex. *Journal of Neuroscience*, *9*(4), 1389–1399.

Keck, T., Mrsic-Flogel, T. D., Afonso, M. V., Eysel, U. T., Bonhoeffer, T., & Hübener, M. (2008). Massive restructuring of neuronal circuits during functional reorganization of adult visual cortex. *Nature Neuroscience*, *11*(10), 1162–1167.

Kerschensteiner, D., & Guido, W. (2017). Organization of the dorsal lateral geniculate nucleus in the mouse. *Visual Neuroscience*, *34*, E008.

Khona, M., & Fiete, I. R. (2022). Attractor and integrator networks in the brain. *Nature Reviews Neuroscience*, *23*(12), 744–766.

Kim, I.-J., Zhang, Y., Meister, M., & Sanes, J. R. (2010). Laminar restriction of retinal ganglion cell dendrites and axons: subtype-specific developmental patterns revealed with transgenic Markers. *Journal of Neuroscience*, *30*(4), 1452–1462.

Klapoetke, N. C., Murata, Y., Kim, S. S., Pulver, S. R., Birdsey-Benson, A., Cho, Y. K., Morimoto, T. K., Chuong, A. S., Carpenter, E. J., Tian, Z., Wang, J., Xie, Y., Yan, Z., Zhang, Y., Chow, B. Y., Surek, B., Melkonian, M., Jayaraman, V., Constantine-Paton, M., ... Boyden, E. S. (2014). Independent optical excitation of distinct neural populations. *Nature Methods*, *11*(3), 338–346.

Knoblich, U., Riesenhuber, M., Freedman, D. J., Miller, E. K., & Poggio, T. (2002). Visual categorization: how the monkey brain does it. In *Biologically Motivated Computer Vision* (pp. 273–281). Springer Berlin Heidelberg.

Ko, H., Mrsic-Flogel, T. D., & Hofer, S. B. (2014). Emergence of feature-specific connectivity in cortical microcircuits in the absence of visual experience. *Journal of Neuroscience*, *34*(29), 9812–9816.

Ko, H., Cossell, L., Baragli, C., Antolik, J., Clopath, C., Hofer, S. B., & Mrsic-Flogel, T. D. (2013). The emergence of functional microcircuits in visual cortex. *Nature*, *496*(7443), 96–100.

Ko, H., Hofer, S. B., Pichler, B., Buchanan, K. A., Sjöström, P. J., & Mrsic-Flogel, T. D. (2011). Functional specificity of local synaptic connections in neocortical networks. *Nature*, *473*(7345), 87–91.

Kossel, A., Lowel, S., & Bolz, J. (1995). Relationships between dendritic fields and functional architecture in striate cortex of normal and visually deprived cats. *Journal of Neuroscience*, *15*(5), 3913–3926.

Kossio, Y. F. K., Goedeke, S., Klos, C., & Memmesheimer, R.-M. (2021). Drifting assemblies for persistent memory: Neuron transitions and unsupervised compensation. *Proceedings of the National Academy of Sciences*, *118*(46), e2023832118.

Krahe, T. E., El-Danaf, R. N., Dilger, E. K., Henderson, S. C., & Guido, W. (2011). Morphologically distinct classes of relay cells exhibit regional preferences in the dorsal lateral geniculate nucleus of the mouse. *Journal of Neuroscience*, *31*(48), 17437–17448.

Kreile, A. K., Bonhoeffer, T., & Hübener, M. (2011). Altered visual experience induces instructive changes of orientation preference in mouse visual cortex. *Journal of Neuroscience*, *31*(39), 13911–13920.

Kremkow, J., & Alonso, J. M. (2021). Functional specificity of afferent connections in visual thalamus. *Neuron*, *109*(15), 2368–2370.

Kremkow, J., & Alonso, J.-M. (2018). Thalamocortical circuits and functional architecture. *Annual Review of Vision Science*, *4*(1), 1–23.

Kuffler, S. W. (1953). Discharge patterns and functional organization Of mammalian retina. *Journal of Neurophysiology*, *16*(1), 37–68.

Laing, R., Turecek, J., Takahata, T., & Olavarria, J. (2015). Identification of eye-specific domains and their relation to callosal connections in primary visual cortex of long evans rats. *Cerebral cortex*, *25*(10), 3314–3329.

Lee, K.-S., Huang, X., & Fitzpatrick, D. (2016). Topology of ON and OFF inputs in visual cortex enables an invariant columnar architecture. *Nature*, *533*(7601), 90–94.

Lee, W.-C. A., Huang, H., Feng, G., Sanes, J. R., Brown, E. N., So, P. T., & Nedivi, E. (2006). Dynamic remodeling of dendritic arbors in GABAergic interneurons of adult visual cortex. *PLoS Biology*, *4*(2), e29.

Levick, W. R. (1967). Receptive fields and trigger features of ganglion cells in the visual streak of the rabbit's retina. *Journal of Physiology*, *188*(3), 285–307.

Levy, M., Lu, Z., Dion, G., & Kara, P. (2014). The shape of dendritic arbors in different functional domains of the cortical orientation map. *Journal of Neuroscience*, *34*(9), 3231–3236.

Li, A. A., Wang, F., Wu, S., & Zhang, X. (2022). Emergence of probabilistic representation in the neural network of primary visual cortex. *iScience*, *25*(3), 103975.

Li, W. (2016). Perceptual learning: use-dependent cortical plasticity. *Annual Review of Vision Science*, *2*(1), 109–130.

Liang, L., & Chen, C. (2020). Organization, function, and development of the mouse retinogeniculate synapse. *Annual Review of Vision Science*, *6*(1), 261–285.

Liang, L., Fratzl, A., Goldey, G., Ramesh, R. N., Sugden, A. U., Morgan, J. L., Chen, C., & Andermann, M. L. (2018). A fine-scale functional logic to convergence from retina to thalamus. *Cell*, *173*(6), 1343–1355.

Liao, D., Hessler, N. A., & Malinow, R. (1995). Activation of postsynaptically silent synapses during pairing-induced LTP in CA1 region of hippocampal slice. *Nature*, *375*(6530), 400–404.

Lin, D. J., Kang, E., & Chen, C. (2014). Changes in input strength and number are driven by distinct mechanisms at the retinogeniculate synapse. *Journal of Neurophysiology*, *112*(4), 942–950.

Linden, D. E. J., Kallenbach, U., Heinecke, A., Singer, W., & Goebel, R. (1999). The myth of upright vision. A psychophysical and functional imaging study of adaptation to inverting spectacles. *Perception*, *28*(4), 469–481.

Litvina, E. Y., & Chen, C. (2017). Functional convergence at the retinogeniculate synapse. *Neuron*, *96*(2), 330–338.

Lomber, S. G., Payne, B. R., Cornwell, P., & Long, K. D. (1996). Perceptual and cognitive visual functions of parietal and temporal cortices in the cat. *Cerebral Cortex*, *6*(5), 673–695.

Makino, H., & Komiyama, T. (2015). Learning enhances the relative impact of top-down processing in the visual cortex. *Nature Neuroscience*, *18*(8), 1116–1122.

Malpeli, J. G., & Baker, F. H. (1975). The representation of the visual field in the lateral geniculate nucleus of Macaca mulatta. *Journal of Comparative Neurology*, *161*(4), 569–594.

Mank, M., Santos, A. F., Direnberger, S., Mrsic-Flogel, T. D., Hofer, S. B., Stein, V., Hendel, T., Reiff, D. F., Levelt, C., Borst, A., Bonhoeffer, T., Hübener, M., & Griesbeck, O. (2008). A genetically encoded calcium indicator for chronic in vivo two-photon imaging. *Nature Methods*, *5*(9), 805–811.

Margolis, D. J., Lütcke, H., Schulz, K., Haiss, F., Weber, B., Kügler, S., Hasan, M. T., & Helmchen, F. (2012). Reorganization of cortical population activity imaged throughout long-term sensory deprivation. *Nature Neuroscience*, *15*(11), 1539–1546.

Marks, T. D., & Goard, M. J. (2021). Stimulus-dependent representational drift in primary visual cortex. *Nature Communications*, *12*(1), 1–16.

Marques, T., Nguyen, J., Fioreze, G., & Petreanu, L. (2018). The functional organization of cortical feedback inputs to primary visual cortex. *Nature Neuroscience*, *21*(5), 757–764.

Martersteck, E. M., Hirokawa, K. E., Evarts, M., Bernard, A., Duan, X., Li, Y., Ng, L., Oh, S. W., Ouellette, B., Royall, J. J., Stoecklin, M., Wang, Q., Zeng, H., Sanes, J. R., & Harris, J. A. (2017). Diverse central projection patterns of retinal ganglion cells. *Cell Reports*, *18*(8), 2058–2072.

Martin, K. A. C., Roth, S., & Rusch, E. S. (2014). Superficial layer pyramidal cells communicate heterogeneously between multiple functional domains of cat primary visual cortex. *Nature Communications*, *5*(1), 1–13.

Mason, C., & Slavi, N. (2020). Retinal ganglion cell axon wiring establishing the binocular circuit. *Annual Review of Vision Science*, *6*(1), 215–236.

Masri, R. A., Grünert, U., & Martin, P. R. (2020). Analysis of parvocellular and magnocellular visual pathways in human retina. *Journal of Neuroscience*, *40*(42), 8132–8148.

Mayrhofer, J. M., Haiss, F., Helmchen, F., & Weber, B. (2015). Sparse, reliable, and long-term stable representation of periodic whisker deflections in the mouse barrel cortex. *NeuroImage*, *115*, 52–63.

McLaughlin, T., Hindges, R., Yates, P. A., & O'Leary, D. D. M. (2003). Bifunctional action of ephrin-B1 as a repellent and attractant to control bidirectional branch extension in dorsal-ventral retinotopic mapping. *Development*, *130*(11), 2407–2418.

McPeek, R. M., & Keller, E. L. (2004). Deficits in saccade target selection after inactivation of superior colliculus. *Nature Neuroscience*, *7*(7), 757–763.

Meyer, A. F., O'Keefe, J., & Poort, J. (2020). Two distinct types of eye-head coupling in freely Moving Mice. *Current Biology*, *30*(11), 2116–2130.

Mineault, P. J., Tring, E., Trachtenberg, J. T., & Ringach, D. L. (2016). Enhanced spatial resolution during locomotion and heightened attention in mouse primary visual cortex. *Journal of Neuroscience*, *36*(24), 6382–6392.

Mishkin, M., & Ungerleider, L. G. (1982). Contribution of striate inputs to the visuospatial functions of parieto-preoccipital cortex in monkeys. *Behavioural Brain Research*, *6*(1), 57–77.

Miyawaki, A., Llopis, J., Heim, R., McCaffery, J. M., Adams, J. A., Ikura, M., & Tsien, R. Y. (1997). Fluorescent indicators for Ca2+based on green fluorescent proteins and calmodulin. *Nature*, *388*(6645), 882–887.

Molotkov, D., Boissonnet, T., & Asari, H. (2022). Topographic projection of retinal ganglion cell axons at single-cell precision underlies retinotopy in the mouse superior colliculus. *bioRxiv*.

Monavarfeshani, A., Sabbagh, U., & Fox, M. A. (2017). Not a one-trick pony: Diverse connectivity and functions of the rodent lateral geniculate complex. *Visual Neuroscience*, *34*.

Mongillo, G., Rumpel, S., & Loewenstein, Y. (2017). Intrinsic volatility of synaptic connections — a challenge to the synaptic trace theory of memory. *Current Opinion in Neurobiology*, *46*, 7–13.

Montgomery, D. P., Hayden, D. J., Chaloner, F. A., Cooke, S. F., & Bear, M. F. (2022). Stimulus-selective response plasticity in primary visual cortex: progress and puzzles. *Frontiers in Neural Circuits*, *15*.

Montijn, J. S., Meijer, G. T., Lansink, C. S., & Pennartz, C. M. (2016). Population-level neural codes are robust to single-neuron variability from a multidimensional coding perspective. *Cell Reports*, *16*(9), 2486–2498.

Morgan, J. L., Berger, D. R., Wetzel, A. W., & Lichtman, J. W. (2016). The fuzzy logic of network connectivity in mouse visual thalamus. *Cell*, *165*(1), 192–206.

Morris, J. S., DeGelder, B., Weiskrantz, L., & Dolan, R. J. (2001). Differential extrageniculostriate and amygdala responses to presentation of emotional faces in a cortically blind field. *Brain*, *124*(6), 1241–1252.

Morris, R. (1984). Developments of a water-maze procedure for studying spatial learning in the rat. *Journal of Neuroscience Methods*, *11*(1), 47–60.

Mrsic-Flogel, T. D., Hofer, S. B., Ohki, K., Reid, R. C., Bonhoeffer, T., & Hübener, M. (2007). Homeostatic regulation of eye-specific responses in visual cortex during ocular dominance plasticity. *Neuron*, *54*(6), 961–972.

Niell, C. M., & Stryker, M. P. (2008). highly selective receptive fields in mouse visual cortex. *Journal of Neuroscience*, *28*(30), 7520–7536.

Niell, C. M., & Stryker, M. P. (2010). Modulation of visual responses by behavioral state in mouse visual cortex. *Neuron*, *65*(4), 472–479.

Noguchi, J., Matsuzaki, M., Ellis-Davies, G. C., & Kasai, H. (2005). Spine-neck geometry determines NMDA receptor-dependent Ca2 signaling in dendrites. *Neuron*, *46*(4), 609–622.

O'Hashi, K., Miyashita, M., & Tanaka, S. (2007). Experience-dependent orientation plasticity in the visual cortex of rats chronically exposed to a single orientation. *Neuroscience Research*, *58*(1), 86–90.

O'Herron, P., Levy, M., Woodward, J. J., & Kara, P. (2020). An unexpected dependence of cortical depth in shaping neural responsiveness and selectivity in mouse visual cortex. *eNeuro*, *7*(2).

Ohki, K., Chung, S., Ch'ng, Y. H., Kara, P., & Reid, R. C. (2005). Functional imaging with cellular resolution reveals precise micro-architecture in visual cortex. *Nature*, *433*(7026), 597–603.

Osterhout, J. A., El-Danaf, R. N., Nguyen, P. L., & Huberman, A. D. (2014). Birthdate and outgrowth timing predict cellular mechanisms of axon target matching in the developing visual pathway. *Cell Reports*, *8*(4), 1006–1017.

Pachitariu, M., Stringer, C., Dipoppa, M., Schröder, S., Rossi, L. F., Dalgleish, H., Carandini, M., & Harris, K. D. (2017). Suite2p: beyond 10,000 neurons with standard two-photon microscopy. *bioRxiv*, 061507.

Packer, O., Hendrickson, A. E., & Curcio, C. A. (1989). Photoreceptor topography of the retina in the adult pigtail macaque (Macaca nemestrina). *Journal of Comparative Neurology*, *288*(1), 165–183.

Panzeri, S., Moroni, M., Safaai, H., & Harvey, C. D. (2022). The structures and functions of correlations in neural population codes. *Nature Reviews Neuroscience*, *23*(9), 551–567.

Paola, V. D., Holtmaat, A., Knott, G., Song, S., Wilbrecht, L., Caroni, P., & Svoboda, K. (2006). Cell type-specific structural plasticity of axonal branches and boutons in the adult neocortex. *Neuron*, *49*(6), 861–875.

Papouin, T., Ladépêche, L., Ruel, J., Sacchi, S., Labasque, M., Hanini, M., Groc, L., Pollegioni, L., Mothet, J.-P., & Oliet, S. H. (2012). Synaptic and extrasynaptic NMDA receptors are gated by different endogenous coagonists. *Cell*, *150*(3), 633–646.

Pelli, D. G. (1997). The VideoToolbox software for visual psychophysics: transforming numbers into movies. *Spatial Vision*, *10*(4), 437–442.

Penn, A. A., Riquelme, P. A., Feller, M. B., & Shatz, C. J. (1998). Competition in retinogeniculate patterning driven by spontaneous activity. *Science*, *279*(5359), 2108–2112.

Pérez-Ortega, J., Alejandre-García, T., & Yuste, R. (2021). Long-term stability of cortical ensembles. *eLife*, *10*, e64449.

Perry, V., & Cowey, A. (1984). Retinal ganglion cells that project to the superior colliculus and pretectum in the macaque monkey. *Neuroscience*, *12*(4), 1125–1137.

Pfeiffenberger, C., Cutforth, T., Woods, G., Yamada, J., Renteria, R. C., Copenhagen, D. R., Flanagan, J. G., & Feldheim, D. A. (2005). Ephrin-As and neural activity are required for eye-specific patterning during retinogeniculate mapping. *Nature Neuroscience*, *8*(8), 1022–1027.

Piscopo, D. M., El-Danaf, R. N., Huberman, A. D., & Niell, C. M. (2013). Diverse visual features encoded in mouse lateral geniculate nucleus. *Journal of Neuroscience*, *33*(11), 4642–4656.

Pizzorusso, T., Medini, P., Berardi, N., Chierzi, S., Fawcett, J. W., & Maffei, L. (2002). Reactivation of ocular dominance plasticity in the adult visual cortex. *Science*, *298*(5596), 1248–1251.

Pologruto, T. A., Sabatini, B. L., & Svoboda, K. (2003). ScanImage: Flexible software for operating laser scanning microscopes. *BioMedical Engineering OnLine*, *2*(1), 1–9.

Polyak, S. (1957). *The vertebrate visual system* (Vol. 277). University of Chicago Press Chicago.

Poort, J., Khan, A. G., Pachitariu, M., Nemri, A., Orsolic, I., Krupic, J., Bauza, M., Sahani, M., Keller, G. B., Mrsic-Flogel, T. D., & Hofer, S. B. (2015). Learning enhances sensory and multiple son-sensory representations in primary visual cortex. *Neuron*, *86*(6), 1478–1490.

Pöppel, E., Held, R., & Frost, D. (1973). Residual visual function after brain wounds involving the central visual pathways in man. *Nature*, *243*(5405), 295–296.

Prothero, D. R. (2016). *The princeton field guide to prehistoric mammals*. Princeton University Press.

Qiu, Y., Zhao, Z., Klindt, D., Kautzky, M., Szatko, K. P., Schaeffel, F., Rifai, K., Franke, K., Busse, L., & Euler, T. (2021). Natural environment statistics in the upper and lower visual field are reflected in mouse retinal specializations. *Current Biology*, *31*(15), 3233–3247.

Rafols, J. A., & Valverde, F. (1973). The structure of the dorsal lateral geniculate nucleus in the mouse. A golgi and electron microscopic study. *Journal of Comparative Neurology*, *150*(3), 303–331.

Rajan, I., & Cline, H. T. (1998). Glutamate receptor activity is required for normal development of tectal cell dendrites in vivo. *Journal of Neuroscience*, *18*(19), 7836–7846.

Ranson, A. (2017). Stability and plasticity of contextual modulation in the mouse visual cortex. *Cell Reports*, *18*(4), 840–848.

Reese, B. E. (1988). 'Hidden lamination' in the dorsal lateral geniculate nucleus: the functional organization of this thalamic region in the rat. *Brain Research Reviews*, *13*(2), 119–137.

Reese, B. E., & Jeffery, G. (1983). Crossed and uncrossed visual topography in dorsal lateral geniculate nucleus of the pigmented rat. *Journal of Neurophysiology*, *49*(4), 877–885.

Reimer, J., Froudarakis, E., Cadwell, C. R., Yatsenko, D., Denfield, G. H., & Tolias, A. S. (2014). Pupil fluctuations track fast switching of cortical states during quiet wakefulness. *Neuron*, *84*(2), 355–362.

Reinert, S., Hübener, M., Bonhoeffer, T., & Goltstein, P. M. (2021). Mouse prefrontal cortex represents learned rules for categorization. *Nature*, *593*(7859), 411–417.

Renart, A., & Machens, C. K. (2014). Variability in neural activity and behavior. *Current Opinion in Neurobiology*, *25*, 211–220.

Ringach, D. L., Mineault, P. J., Tring, E., Olivas, N. D., Garcia-Junco-Clemente, P., & Trachtenberg, J. T. (2016). Spatial clustering of tuning in mouse primary visual cortex. *Nature Communications*, *7*(1), 1–9.

Rompani, S. B., Müllner, F. E., Wanner, A., Zhang, C., Roth, C. N., Yonehara, K., & Roska, B. (2017). Different modes of visual integration in the lateral geniculate nucleus revealed by single-cell-initiated transsynaptic tracing. *Neuron*, *93*(4), 767–776.

Rose, T., & Bonhoeffer, T. (2018). Experience-dependent plasticity in the lateral geniculate nucleus. *Current Opinion in Neurobiology*, *53*, 22–28.

Rose, T., Jaepel, J., Hübener, M., & Bonhoeffer, T. (2016). Cell-specific restoration of stimulus preference after monocular deprivation in the visual cortex. *Science*, *352*(6291), 1319–1322.

Rosón, M. R., Bauer, Y., Kotkat, A. H., Berens, P., Euler, T., & Busse, L. (2019). Mouse dLGN receives functional input from a diverse population of retinal ganglion cells with limited convergence. *Neuron*, *102*(2), 462–476.

Rossum, V., & Drake, F. L. (2009). Python 3 reference manual createspace.

Roth, M. M., Dahmen, J. C., Muir, D. R., Imhof, F., Martini, F. J., & Hofer, S. B. (2016). Thalamic nuclei convey diverse contextual information to layer 1 of visual cortex. *Nature Neuroscience*, *19*(2), 299–307.

Rule, M. E., & O'Leary, T. (2022). Self-healing codes: How stable neural populations can track continually reconfiguring neural representations. *Proceedings of the National Academy of Sciences*, *119*(7), e2106692119.

Rule, M. E., O'Leary, T., & Harvey, C. D. (2019). Causes and consequences of representational drift. *Current Opinion in Neurobiology*, *58*, 141–147.

Sammons, R. P., Clopath, C., & Barnes, S. J. (2018). Size-dependent axonal bouton dynamics following visual deprivation in vivo. *Cell Reports*, *22*(3), 576–584.

Samonds, J. M., Choi, V., & Priebe, N. J. (2019). Mice discriminate stereoscopic surfaces without fixating in depth. *Journal of Neuroscience*, *39*(41), 8024–8037.

Sasaki, K. S., Kimura, R., Ninomiya, T., Tabuchi, Y., Tanaka, H., Fukui, M., Asada, Y. C., Arai, T., Inagaki, M., Nakazono, T., Baba, M., Kato, D., Nishimoto, S., Sanada, T. M., Tani, T., Imamura, K., Tanaka, S., & Ohzawa, I. (2015). Supranormal orientation selectivity of visual neurons in orientation-restricted animals. *Scientific Reports*, *5*(1), 1–12.

Sawtell, N. B., Frenkel, M. Y., Philpot, B. D., Nakazawa, K., Tonegawa, S., & Bear, M. F. (2003). NMDA receptor-dependent ocular dominance plasticity in adult visual cortex. *Neuron*, *38*(6), 977–985.

Schiller, P. H., Sandell, J. H., & Maunsell, J. H. (1987). The effect of frontal eye field and superior colliculus lesions on saccadic latencies in the rhesus monkey. *Journal of Neurophysiology*, *57*(4), 1033–1049.

Schindelin, J., Arganda-Carreras, I., Frise, E., Kaynig, V., Longair, M., Pietzsch, T., Preibisch, S., Rueden, C., Saalfeld, S., Schmid, B., Tinevez, J.-Y., White, D. J., Hartenstein, V., Eliceiri, K., Tomancak, P., & Cardona, A. (2012). Fiji: an open-source platform for biological-image analysis. *Nature Methods*, *9*(7), 676–682.

Schmidt, K. E., Kim, D.-S., Singer, W., Bonhoeffer, T., & Löwel, S. (1997). Functional specificity of long-range intrinsic and interhemispheric connections in the visual cortex of strabismic cats. *Journal of Neuroscience*, *17*(14), 5480–5492.

Schmidt, K. E., & Wolf, F. (2021). Punctuated evolution of visual cortical circuits? Evidence from the large rodent Dasyprocta leporina, and the tiny primate Microcebus murinus. *Current Opinion in Neurobiology*, *71*, 110–118.

Schneider, C. A., Rasband, W. S., & Eliceiri, K. W. (2012). NIH Image to ImageJ: 25 years of image analysis. *Nature Methods*, *9*(7), 671–675.

Schneider, G. E. (1969). Two visual systems. *Science*, *163*(3870), 895–902.

Scholl, B., Burge, J., & Priebe, N. J. (2013). Binocular integration and disparity selectivity in mouse primary visual cortex. *Journal of Neurophysiology*, *109*(12), 3013–3024.

Scholl, B., Pattadkal, J. J., & Priebe, N. J. (2017). Binocular disparity selectivity weakened after monocular deprivation in mouse V1. *Journal of Neuroscience*, *37*(27), 6517–6526.

Schoonover, C. E., Ohashi, S. N., Axel, R., & Fink, A. J. P. (2021). Representational drift in primary olfactory cortex. *Nature*, *594*(7864), 541–546.

Schumacher, J. W., McCann, M. K., Maximov, K. J., & Fitzpatrick, D. (2022). Selective enhancement of neural coding in V1 underlies fine-discrimination learning in tree shrew. *Current Biology*, *32*(15), 3245–3260.

Sengpiel, F., Gödecke, I., Stawinski, P., Hübener, M., Löwel, S., & Bonhoeffer, T. (1998). Intrinsic and environmental factors in the development of functional maps in cat visual cortex. *Neuropharmacology*, *37*(4-5), 607–621.

Sengpiel, F., Stawinski, P., & Bonhoeffer, T. (1999). Influence of experience on orientation maps in cat visual cortex. *Nature Neuroscience*, *2*(8), 727–732.

Shang, C., Liu, Z., Chen, Z., Shi, Y., Wang, Q., Liu, S., Li, D., & Cao, P. (2015). A parvalbumin-positive excitatory visual pathway to trigger fear responses in mice. *Science*, *348*(6242), 1472–1477.

Shatz, C. J., Lindström, S., & Wiesel, T. N. (1977). The distribution of afferents representing the right and left eyes in the cat's visual cortex. *Brain Research*, *131*(1), 103–116.

Shatz, C. J., & Stryker, M. P. (1978). Ocular dominance in layer IV of the cat's visual cortex and the effects of monocular deprivation. *Journal of Physiology*, *281*(1), 267–283.

Sholl, D. (1953). Dendritic organization in the neurons of the visual and motor cortices of the cat. *Journal of Anatomy*, *87*(Pt 4), 387.

Shtoyerman, E., Arieli, A., Slovin, H., Vanzetta, I., & Grinvald, A. (2000). Long-term optical imaging and spectroscopy reveal mechanisms underlying the intrinsic signal and stability of cortical maps in V1 of behaving monkeys. *Journal of Neuroscience*, *20*(21), 8111–8121.

Sibille, J., Gehr, C., Benichov, J. I., Balasubramanian, H., Teh, K. L., Lupashina, T., Vallentin, D., & Kremkow, J. (2022). High-density electrode recordings reveal strong and specific connections between retinal ganglion cells and midbrain neurons. *Nature Communications*, *13*(1), 1–18.

Siegle, J. H., Jia, X., Durand, S., Gale, S., Bennett, C., Graddis, N., Heller, G., Ramirez, T. K., Choi, H., Luviano, J. A., Groblewski, P. A., Ahmed, R., Arkhipov, A., Bernard, A., Billeh, Y. N., Brown, D., Buice, M. A., Cain, N., Caldejon, S., ... Koch, C. (2021). Survey of spiking in the mouse visual system reveals functional hierarchy. *Nature*, *592*(7852), 86–92.

Simon, D. K., & O'Leary, D. D. (1992). Development of topographic order in the mammalian retinocollicular projection. *Journal of Neuroscience*, *12*(4), 1212–1232.

Sincich, L. C., Zhang, Y., Tiruveedhula, P., Horton, J. C., & Roorda, A. (2009). Resolving single cone inputs to visual receptive fields. *Nature Neuroscience*, *12*(8), 967–969.

Singer, W., Tretter, F., & Yinon, U. (1979). Inverted vision causes selective loss of striate cortex neurons with binocular, vertically oriented receptive fields. *Brain Research*, *170*(1), 177–181.

Singer, W., Yinon, U., & Tretter, F. (1979). Inverted monocular vision prevents ocular dominance shift in kittens and impairs the functional state of visual cortex in adult cats. *Brain Research*, *164*(1-2), 294–299.

Sommeijer, J.-P., Ahmadlou, M., Saiepour, M. H., Seignette, K., Min, R., Heimel, J. A., & Levelt, C. N. (2017). Thalamic inhibition regulates critical-period plasticity in visual cortex and thalamus. *Nature Neuroscience*, *20*(12), 1715–1721.

Steinberg, R. H., Reid, M., & Lacy, P. L. (1973). The distribution of rods and cones in the retina of the cat (Felis domesticus). *Journal of Comparative Neurology*, *148*(2), 229–248.

Stettler, D. D., Yamahachi, H., Li, W., Denk, W., & Gilbert, C. D. (2006). Axons and synaptic boutons are highly dynamic in adult visual cortex. *Neuron*, *49*(6), 877–887.

Stone, J. (1983). *Parallel processing in the visual system, The classification of retinal ganglion cells and its impact on the neurobiology of vision.*

Stratton, G. M. (1897). Vision without inversion of the retinal image. *Psychological Review*, *4*(5), 463–481.

Stratton, G. M. (1896). Some preliminary experiments on vision without inversion of the retinal image. *Psychological Review*, *3*(6), 611–617.

Stryker, M. P., Sherk, H., Leventhal, A. G., & Hirsch, H. V. (1978). Physiological consequences for the cat's visual cortex of effectively restricting early visual experience with oriented contours. *Journal of Neurophysiology*, *41*(4), 896–909.

Sugita, Y. (1996). Global plasticity in adult visual cortex following reversal of visual input. *Nature*, *380*(6574), 523–526.

Sur, M., Humphrey, A. L., & Sherman, S. M. (1982). Monocular deprivation affects X- and Y-cell retinogeniculate terminations in cats. *Nature*, *300*(5888), 183–185.

Szatko, K. P., Korympidou, M. M., Ran, Y., Berens, P., Dalkara, D., Schubert, T., Euler, T., & Franke, K. (2020). Neural circuits in the mouse retina support color vision in the upper visual field. *Nature Communications*, *11*(1), 1–14.

Szél, Á., Röhlich, P., Gaffé, A. R., Juliusson, B., Aguirre, G., & Veen, T. V. (1992). Unique topographic separation of two spectral classes of cones in the mouse retina. *Journal of Comparative Neurology*, *325*(3), 327–342.

Tanaka, S., Tani, T., Ribot, J., O'Hashi, K., & Imamura, K. (2009). A postnatal critical period for orientation plasticity in the cat visual cortex. *PLoS ONE*, *4*(4), e5380.

Tieman, S. B. (1984). Effects of monocular deprivation on geniculocortical synapses in the cat. *Journal of Comparative Neurology*, *222*(2), 166–176.

Tring, E., Duan, K. K., & Ringach, D. L. (2022). ON/OFF domains shape receptive field structure in mouse visual cortex. *Nature Communications*, *13*(1), 1–11.

Triplett, J. W., & Feldheim, D. A. (2012). Eph and ephrin signaling in the formation of topographic maps. *Seminars in Cell & Developmental Biology*, *23*(1), 7–15.

Usrey, W. M., Reppas, J. B., & Reid, R. C. (1999). Specificity and strength of retinogeniculate connections. *Journal of Neurophysiology*, *82*(6), 3527–3540.

Vega-Zuniga, T., Medina, F. S., Fredes, F., Zuniga, C., Severín, D., Palacios, A. G., Karten, H. J., & Mpodozis, J. (2013). Does nocturnality drive binocular vision? octodontine rodents as a case study. *PLoS ONE*, *8*(12), e84199.

Wallace, D. J., Fitzpatrick, D., & Kerr, J. N. (2016). Primate thalamus: More than meets an eye. *Current Biology*, *26*(2), R60–R61.

Wang, B.-S., Sarnaik, R., & Cang, J. (2010). Critical period plasticity matches binocular orientation preference in the visual cortex. *Neuron*, *65*(2), 246–256.

Wang, Q., Gao, E., & Burkhalter, A. (2011). Gateways of ventral and dorsal streams in mouse visual cortex. *Journal of Neuroscience*, *31*(5), 1905–1918.

Wang, Q., Sporns, O., & Burkhalter, A. (2012). Network analysis of corticocortical connections reveals ventral and dorsal processing streams in mouse visual cortex. *Journal of Neuroscience*, *32*(13), 4386–4399.

Wang, Q., Ding, S.-L., Li, Y., Royall, J., Feng, D., Lesnar, P., Graddis, N., Naeemi, M., Facer, B., Ho, A., Dolbeare, T., Blanchard, B., Dee, N., Wakeman, W., Hirokawa, K. E., Szafer, A., Sunkin, S. M., Oh, S. W., Bernard, A., … Ng, L. (2020). The Allen Mouse Brain Common Coordinate Framework: A 3D reference atlas. *Cell*, *181*(4), 936–953.

Watkins, J. C., & Evans, R. H. (1981). Excitatory amino acid transmitters. *Annual Review of Pharmacology and Toxicology*, *21*(1), 165–204.

Wei, P., Liu, N., Zhang, Z., Liu, X., Tang, Y., He, X., Wu, B., Zhou, Z., Liu, Y., Li, J., Zhang, Y., Zhou, X., Xu, L., Chen, L., Bi, G., Hu, X., Xu, F., & Wang, L. (2015). Processing of visually evoked innate fear by a non-canonical thalamic pathway. *Nature Communications*, *6*(1), 1–13.

Weiler, S., Nilo, D. G., Bonhoeffer, T., Hübener, M., Rose, T., & Scheuss, V. (2022). Functional and structural features of L2/3 pyramidal cells continuously covary with pial depth in mouse visual cortex. *Cerebral Cortex*.

Weiskrantz, L., Warrington, E. K., Sanders, M. D., & Marshall, J. (1974). Visual Capacity In The Hemianopic Field Following A Restricted Occipital Ablation. *Brain*, *97*(1), 709–728.

Wiesel, T. N., & Hubel, D. H. (1963a). Single-cell responses in striate cortex of kittens deprived of vision in one eye. *Journal of Neurophysiology*, *26*(6), 1003–1017.

Wiesel, T. N., & Hubel, D. H. (1963b). Effects Of Visual Deprivation On Morphology And Physiology Of Cells In The Cat's Lateral Geniculate Body. *Journal of Neurophysiology*, *26*(6), 978–993.

Williams, S. E., Mann, F., Erskine, L., Sakurai, T., Wei, S., Rossi, D. J., Gale, N. W., Holt, C. E., Mason, C. A., & Henkemeyer, M. (2003). Ephrin-B2 and EphB1 mediate retinal axon divergence at the optic chiasm. *Neuron*, *39*(6), 919–935.

Xia, J., Marks, T. D., Goard, M. J., & Wessel, R. (2021). Stable representation of a naturalistic movie emerges from episodic activity with gain variability. *Nature Communications*, *12*(1), 1–15.

Yamahachi, H., Marik, S. A., McManus, J. N., Denk, W., & Gilbert, C. D. (2009). Rapid axonal sprouting and pruning accompany functional reorganization in primary visual cortex. *Neuron*, *64*(5), 719–729.

Yoshida, T., Ozawa, K., & Tanaka, S. (2012). Sensitivity profile for orientation selectivity in the visual cortex of goggle-reared mice. *PLoS ONE*, *7*(7), e40630.

Yoshitake, K., Tsukano, H., Tohmi, M., Komagata, S., Hishida, R., Yagi, T., & Shibuki, K. (2013). Visual map shifts based on whisker-guided cues in the young mouse visual cortex. *Cell Reports*, *5*(5), 1365–1374.

Zeater, N., Cheong, S. K., Solomon, S. G., Dreher, B., & Martin, P. R. (2015). Binocular visual responses in the primate lateral geniculate nucleus. *Current Biology*, *25*(24), 3190–3195.

Zhang, J., Ackman, J. B., Xu, H.-P., & Crair, M. C. (2012). Visual map development depends on the temporal pattern of binocular activity in mice. *Nature Neuroscience*, *15*(2), 298–307.

Zhao, X., Liu, M., & Cang, J. (2013). Sublinear binocular integration preserves orientation selectivity in mouse visual cortex. *Nature Communications*, *4*(1), 1–12.

Žiburkus, J., & Guido, W. (2006). Loss of Binocular Responses and Reduced Retinal Convergence During the Period of Retinogeniculate Axon Segregation. *Journal of Neurophysiology*, *96*(5), 2775–2784.

Ziv, Y., Burns, L. D., Cocker, E. D., Hamel, E. O., Ghosh, K. K., Kitch, L. J., Gamal, A. E., & Schnitzer, M. J. (2013). Long-term dynamics of CA1 hippocampal place codes. *Nature Neuroscience*, *16*(3), 264–266.

Acronyms

AAV	Adeno associated virus
ACCF	Allen common coordinate framework
AMPAR	AMPA receptor
area A	Anterior HVA
area AM	Anteromedial HVA
area LI	Laterointermediate HVA
area LM	Lateromedial HVA
area P	Posterior HVA
area PM	Posteromedial HVA
area POR	Postrhinal HVA
area RL	Rostrolateral HVA
CS-	Non-conditioned stimulus
CS+	Conditioned stimulus
dLGN	Dorsal lateral geniculate nucleus of the thalamus
DOi	Dendritic orientaiton index
DS	Direction selectivity
E#	Embryonic day #
EGFP	Enhanced green fluorescent protein
EPSC	Excitatory post synaptic current
FD	Fluorescence difference
HVA	Higher visual area
IOS	Intrinsic optical signal imaging
LLM	Like-to-like microcircuit
LP	Lateral posterior nucleus of the thalamus
M	Magnocellular
MD	Monocular deprivation
NMDAR	NMDA receptor
ODI	Ocular dominance index
ooDSGC	ON-OFF direction selective retinal ganglion cell
OS	Orientation selectivity
P	Parvocellular
P#	Postnatal day #
PFA	Paraformaldehyde
PO	Preferred orientation
PPC	Posterior parietal cortex
PSC	Pairwise signal correlation
RF	Receptive field
ROI	Region of interest
SC	Superior colliculus
TC	Thalamocortical
V1	Primary visual cortex

Declaration of author contribution and Acknowledgements

Declaration of author contribution

Binocularity in the dLGN

The project was conceived by Simon Weiler, myself, Martin H.P. Fernholz and Tobias Rose. I established and performed intravitreal injections for viral delivery in the lab. The adult acute brain slice approach for *in vitro* electrophysiological recordings was developed by Simon Weiler. The two-step optogenetic stimulation protocol was developed by Simon Weiler and Martin H.P. Fernholz. All *in vitro* recordings from dLGN neurons were performed by Martin H.P. Fernholz and Simon Weiler. Clearing and antibody staining of brain slices and retinas was performed by Volker Staiger, and subsequent confocal imaging was performed by Martin H.P. Fernholz, Volker Staiger, myself and Robert Kasper. Martin H.P Fernholz reidentified all dLGN neurons in confocal and two-photon image stacks. Volker Staiger, Meike Hack and Ursula Weber reconstructed the morphologies of dLGN neurons. Quality control of data was done by myself and Martin H.P Fernholz. I developed the pipeline for analysing axodendritic overlap and its effects on functional binocular convergence, with help from Martin H.P. Fernholz. I wrote the majority of data analysis routines with help from Simon Weiler and Martin H.P. Fernholz.

Representational drift of orientation tuning

The project was conceived by myself, Uwe Lewin, Tobias Rose, Carl Schoonover, Andrew Fink, Tobias Bonhoeffer and Mark Hübener. Surgeries, animal handling, stripe rearing and chronic two-photon imaging was performed by myself and Uwe Lewin. Manual annotation of calcium imaging data was performed by Sascha Hay, Sano Kishwer, Ezgi Kaya and Meike Hack, while Uwe Lewin and myself performed manual neuron matching across days. Data analysis was performed by myself with help from Uwe Lewin.

Acknowledgements

First, I would like to thank Tobias Rose and Mark Hübener for supervising me during my thesis. Tobias Rose in particular, you took me onboard, when I started in the lab and guided my scientific development in the first five years of my PhD. To you Mark Hübener, I am grateful for taking over the role of my supervisor after Tobias Rose moved to his new position. I would like to thank you Tobias Bonhoeffer for accepting me into your lab and for sound and honest advice, both scientific and personal. Andrew Fink and Carl E. Schoonover, thank you for reinvigorating my enthusiasm for representational drift, many interesting conversations, and convincing me to do one (or two) more rounds of experiments. Within this extensive list of advisors, I would also like to thank Laura Busse, who was on my thesis advisory committee (TAC), you always had an open ear, even outside the official TAC meetings.

I would like to thank the Max Planck Society and the International Max Planck Research School for Life Sciences (IMPRS-LS), for financial support during my PhD and providing an inspiring research environment.

A big thank you also goes to Volker Staiger, Claudia Huber, Frank Voss, Max Sperling and Meike Hack for keeping the lab running in both the obvious and sometimes not so obvious ways. In particular, thank you Volker Staiger, for being an integral member of the dLGN experimental team.

Thank you to Simon Weiler, Martin M.P. Fernholz and David Laubender for being wonderful team mates in the dLGN binocularity project. Our work together on this "side project" was always fun and probably kept me from calling it quits at times.

I only agreed to pursue the stripe rearing experiments under the condition that a new student would join the team. Uwe Lewin, you delivered above and beyond what I could ever have hoped for. A wonderful colleague and an easy first mentee! It was my pleasure to develop this project and perform these experiments with you.

Thank you, to the rest of the Bon-Bros, for both in and out of lab shenanigans, and for all the valuable experience and scientific insights you shared with me. In particular Juliane Jaepel, thank you for teaching me the skills I needed when I started my PhD, and for being a wonderful friend. Thank you to Pieter Goltstein, for the brewing bonanzas, and for always helping with technical issues at the B-scope. Without you, the B-scope would probably have burst into flame. David Laubender and Mike Myoga, thank you for quite a number of emergency pizzas and beers.

Finally, I would like to thank my family, in particular my parents Hans-Peter and Marcella, for always supporting me, guiding my education and steering me away from stupid decisions. Lastly, I want to thank the newest member of my family, Sandra Reinert. My partner in love, science, and sometimes minor crimes. I cannot overstate how grateful I am to have met you, and for all the support you have given me over the years. The projects in this thesis would not be what they are without our late-night discussion. It was tough at times, and without you I almost certainly would have quit.

Affidavit

Hiermit versichere ich an Eides statt, dass ich die vorliegende Dissertation *On computations and their maintenance in the mouse visual system* selbstständig angefertigt habe, mich außer der angegebenen keiner weiteren Hilfsmittel bedient und alle Erkenntnisse, die aus dem Schrifttum ganz oder annähernd übernommen sind, als solche kenntlich gemacht und nach ihrer Herkunft unter Bezeichnung der Fundstelle einzeln nachgewiesen habe.

I hereby confirm that the dissertation *On computations and their maintenance in the mouse visual system* is the result of my own work and that I have only used sources or materials listed and specified in the dissertation.

Joel Bauer
München, den 14.12.22
Munich, 14.12.22

Erklärung

Hiermit erkläre ich, dass die Dissertation nicht ganz oder in wesentlichen Teilen einer anderen Prüfungskomission vorgelegt worden ist, und dass ich mich anderweitig einer Doktorprüfung ohne Erfolg nicht unterzogen habe.

Joel Bauer
München, den 14.12.22